TWO-DIMENSIONAL CRYSTALLIZATION OF SIGNAL PEPTIDE PEPTIDASE AND SINGLE PARTICLE CRYO-EM OF THREE PHOTOSYSTEM II COMPLEXES RELEVANT TO PHOTOINHIBITION

A Dissertation
Presented to
The Academic Faculty

by

Kasahun Neselu

In Partial Fulfilment
Of the requirements for the Degree
Ph.D. in the
School of Biological Sciences

Georgia Institute of Technology
August 2021

TWO-DIMENSIONAL CRYSTALLIZATION OF SIGNAL PEPTIDE PEPTIDASE AND SINGLE PARTICLE CRYO-EM OF THREE PHOTOSYSTEM II COMPLEXES RELEVANT TO PHOTOINHIBITION

Approved by:

Dr. Ingeborg Schmidt-Krey, Advisor
School of Biological Sciences
Georgia Institute of Technology

Dr. Raquel Lieberman
School of Chemistry & Biochemistry
Georgia Institute of Technology

Dr. Loren Williams
School of Chemistry & Biochemistry
Georgia Institute of Technology

Dr. Yuhong Fan
School of Biological Sciences
Georgia Institute of Technology

Dr. Matthew Torres
School of Biological Sciences
Georgia Institute of Technology

Date Approved: July 2021

ACKNOWLEDGMENTS

First, I want to thank my family for their love and support. They have nurtured and given me way more than they could afford. I would not be where I am today without them. They have cheered me on my good days and encouraged me to push through on my bad days. I want to thank my parents for the values they have installed in me. They have taught me to appreciate the things I have and work for the things I want. They have taught me planning and working hard always take me where I want to go. The values they have instilled in me have brought me to where I am today and will continue to carry me in my adventures ahead.

I want to thank all of my teacher for preparing me for the journey ahead. I want to thank my elementary school teachers who prepared me for middle school, my middle school teachers who prepared me for high school, my high school teachers who prepared me for my undergraduate studies, my undergraduate professors who prepared me for my graduate studies, and my graduate school professors who have prepared me for my graduate level works. I want to thank my committee members who have helped me grow as a researcher. All of their critiques, guidance, and support have helped me to develop my scientific thinking.

I especially want to thank my Ph.D. advisor, Dr. Schmidt-Krey because she has made my years at Tech a wonderful experience. She has challenged me to be the best I can be inside and outside of research. Even with her busy schedule, she always makes time to meet with all of her graduate students and provide the proper guidance. She always gives us constructive feedback on our works and help us become better researchers. I could not have completed this journey without her.

I would like to thank my current and past lab mates: Dr. Yusuf Uddin, Carolan Espy, Tajah Damm, Arshay Grant, Dr. Kerry Strickland, Maureen Metcalfe, Eric Woods, Justin

Dehorty, and Shuo Huan. I have learned a lot from all of them and I will always cherish the times we spent together. I would also like to thank my friends here at Georgia Tech. I have a lot of good memories to keep with me.

TABLE OF CONTENT

PAGE

ACKNOWLEDGEMENTS ii
LIST OF TABLES vi
LIST OF FIGURES vii
LIST OF SYMBOLS AND ABBREVIATIONS xi
SUMMARY xiii

CHAPTER 1: INTRODUCTION 1
1.1 METHODS USED FOR STRUCTURE DETERMINATION 1
1.2 CRYO-EM 1
1.3 SINGLE PARTICLE CRYO-EM 2
1.4 2D ELECTRON CRYSTALLOGRAPHY 4
1.5 CHALLENGES IN CRYO-EM 6
1.5.1 SAMPLE PREPARATION 6
1.5.2 DATA COLLECTION 7
1.5.3 IMAGE PROCESSING 7
1.6 RECENT ADVANCES IN CRYO-EM 9
1.7 PDB STRUCTURE JUMP 10
1.8 MEMBRANE PROTEINS 12

CHAPTER 2 TWO-DIMENSIONAL CRYSTALLIZATION OF SIGNAL PEPTIDE PEPTIDASE 14
2.1 INTRODUCTION 14
2.2 MCMJR1SPP EXPERIMENTAL PROCEDURES 20
2.2.1 MCMJR1 SPP EXPRERESSION AND PURIIFICTATION 20
2.2.2 MCMJR1SPP TWO-DIMENSIONAL CRYSTALLIZATION 20
2.2.3 MCMJR1SPP NEGATIVE STAIN TEM GRID PREPARATION 23
2.2.4 MCMJR1SPP TEM IMAGING 23
2.2.5 MCMJR1SPP IMAGE EVALUATION 23
2.2.6 MCMJR1SPP CRYSTALLIZATION CONDITION OPTIMIZATION 27
2.3 RESULTS 28
2.4 DISCUSSION 55
2.5 ACKNOWLEDGEMENTS 58

CHAPTER 3: CRYO-EM: SINGLE PARTICLE ANALYSIS OF ACTIVE PSII 59
3.1 INTRODUCTION 59
3.2 PSII EXPERIMENTAL PROCEDURES 62
3.2.1 PURIFICATION OF ACTIVE PSII 62
3.2.2 CRYO-EM GRID PREPARATION OF ACTIVE PSII 62
3.2.3 CRYO-EM DATA COLLECTION AND IMAGE 63

PROCESSING OF ACTIVE PSII
3.3 RESULTS 64
3.4 DISCUSSION 73
3.5 ACKNOWLEDGMENTS 77

CHAPTER 4: SINGLE PARTICLE ANALYSIS OF PSII SALT WASH AND UREA WASH COMPLEXES 78
4.1 INTRODUCTION 78
4.2 PSII EXPERIMENTAL PROCEDURES 82
4.2.1 PURIFICATION OF ACTIVE PSII AND SALT AND UREA TREATMENTS 82
4.2.2 SALT WASH AND UREA WASH PSII CRYO-EM GRID PREPARATION 82
4.2.3 SALT WASH AND UREA WASH PSII DATA COLLECTION AND IMAGE PROCESSING 83
4.3 RESULTS 84
4.4 DISCUSSION 100
4.5 ACKNOWLEDGMENTS 104

CHAPTER 5: CONCLUSIONS AND FUTURE DIRECTIONS 105
5.1 CONCLUSIONS 105
5.2 MCMJR1SPP FUTURE DIRECTIONS 106
5.2.1 CRYSTALLIZATION TRIALS 106
5.2.2 MCMJR1SPP 2D CRYO-EM AND FOLLOW UP EXPERIMENTS 107
5.3 PSII FUTURE DIRECTIONS 108
5.3.1 PSII CRYO-EM SAMPLE PREPARATION 108
5.3.2 DATA COLLECTION 108
5.3.3 AUTOMATIC PARTICLE PICKING 109

REFERENCES 110

LIST OF TABLES

Table 2.1. A representative 2D crystallization trial. Each dialysis experiment examines 4 different conditions for each crystallization parameter.……...22

Table 2.2. Different 2D crystallization parameters tested to improve the quality and size of MCMJR1SPP crystals.……29

Table 4.1. Extrinsic subunits present in the 3 PSII samples……78

LIST OF FIGURES

Figure 1.1. Cryo-EM single particle analysis flowchart.……...…….3

Figure 1.2. 2D Electron crystallography flowchart.……5

Figure 1.3. Overall growth of structures released by year……...…...……..11

Figure 1.4. Overall growth of cryo-EM structures released by year….……12

Figure 2.1. Secondary structure of MCMJR1SPP (PDB ID: 4HYC)…...……..…..15

Figure 2.2. Gamma secretase subunits (PDB ID: 5A63):……..……...16

Figure 2.3. Presenilin and SPP have opposite membrane orientations. ……...……17

Figure 2.4. MCMJR1SPP (PDB ID: 4HYC) active site (YD, GxGD)...……..……18

Figure 2.5. Two-dimensional crystallization by dialysis……..21

Figure 2.6. Different membrane morphologies from MCMJR1SPP crystallization trials……24

Figure 2.7. Fast Fourier Transform (FFT) quality…...……..…….....27

Figure 2.8. Representative micrographs from MCMJR1SPP LPR3 2D crystallization trials….30

Figure 2.9. Representative micrographs from MCMJR1SPP LPR8 2D crystallization trials….31

Figure 2.10. Representative micrographs from MCMJR1SPP LPR26 2D crystallization trials..32

Figure 2.11. Representative micrographs from MCMJR1SPP pH5.5 2D crystallization trials...33

Figure 2.12. Representative micrographs from MCMJR1SPP pH6 2D crystallization trials…..34

Figure 2.13. Representative micrographs from MCMJR1SPP pH8 2D crystallization trials…..36

Figure 2.14. Representative micrographs from MCMJR1SPP 21°C 2D crystallization trials…37

Figure 2.15. Representative micrographs from MCMJR1SPP 27°C 2D crystallization trials…39

Figure 2.16. Representative micrographs from MCMJR1SPP 30°C 2D crystallization trials....43

Figure 2.17. Representative micrographs from MCMJR1SPP 0% glycerol 2D crystallization trials……45

Figure 2.18. Representative micrographs from MCMJR1SPP 20% glycerol 2D crystallization trials……47

Figure 2.19. Representative micrographs from MCMJR1SPP 0mM NaCl 2D crystallization trials……..……...49

Figure 2.20. Representative micrographs from MCMJR1SPP 250mM NaCl 2D crystallization trials……...…….51

Figure 2.21. Representative micrographs from MCMJR1SPP 1M NaCl 2D crystallization trials……53

Figure 3.1. Structure of spinach PSII (PDB ID: 3JCU)….……...60

Figure 3.2. Cryo-EM image quality assessment of active (control) PSII sample…….65

Figure 3.3. Representative Cryo-EM micrograph from the active (control) PSII data collection……..……..66

Figure 3.4. Class averages (500) generated from active (control) PSII particles using cisTEM……...67

Figure 3.5. Individual PSII particles……..……...67

Figure 3.6. Active PSII class averages were used to generate 3D reconstruction……68

Figure 3.7. Class averages (250) generated from active (control) PSII particles using cisTEM……..…….69

Figure 3.8. Individual PSII particles……...……..69

Figure 3.9. Class averages (50) generated from active (control) PSII particles using cisTEM……...70

Figure 3.10. Class averages (10) generated from active (control) PSII particles using cisTEM……...70

Figure 3.11. Active PSII class averages were used to generate 3D reconstruction……..71

Figure 3.12. 3D reconstructions from short and long class averages...……72

Figure 4.1. Schematic representation showing location of the extrinsic subunits in active (control) PSII, salt wash PSII, and urea wash PSII……....79

Figure 4.2. Inactive spinach PSII (PDB ID: 3JCU).…….....80

Figure 4.3. Representative Cryo-EM micrograph from the salt wash PSII data collection….....86

Figure 4.4. Class averages generated from salt wash PSII particles using cisTEM...……..87

Figure 4.5. Salt wash PSII class averages were used to generate 3D reconstruction...……88

Figure 4.6. Representative Cryo-EM micrograph from the urea wash PSII data collection..…..89

Figure 4.7. Class averages generated from urea wash PSII particles using cisTEM…..……..90

Figure 4.8. Urea wash PSII class averages were used to generate 3D reconstruction...……...91

Figure 4.9. Class averages from Control PSII sample..……92

Figure 4.10. Class averages from salt wash PSII sample..……....92

Figure 4.11. Class averages from urea wash PSII sample……93

Figure 4.12. Superimposed comparison of active PSII 3D reconstruction with spinach PSII structure (PDB ID: 3JCU)……..94

Figure 4.13. Superimposed comparison of the salt wash PSII 3D reconstruction with spinach PSII structure (PDB ID: 3JCU)…….....95

Figure 4.14. Superimposed comparison of urea wash PSII 3D reconstruction with spinach PSII structure (PDB ID: 3JCU)……..…96

Figure 4.15. Superimposed comparison of active (Green) and salt wash (Red) PSII 3D reconstructions……...…97

Figure 4.16. Superimposed comparison of active (Green) and urea wash (Blue) PSII 3D reconstructions……...98

Figure 4.17. Superimposed comparison of salt wash (Red) and urea wash (Blue) PSII 3D reconstructions……...99

LIST OF SYMBOLS AND ABBREVIATIONS

2D	two-dimensional
3D	three-dimensional
Å	Ångström
APP	amyloid precursor protein
Aβ	amyloid beta
BBY	Berthold, Babcock, Yocum sample
CCD	charged-coupled device
CMC	critical micelle concentration
Cryo-EM	electron cryo-microscopy
DDM	dodecyl β-D-maltoside
DMPC	1,2-dimyristoyl-sn-glycero-3-phosphocholine
DNA	deoxyribonucleic acid
DQE	detective quantum efficiency
EM	transmission electron microscope
ER	endoplasmic reticulum
FFT	Fast Fourier transform
HEPES	4-(2-hyroxyethyl)-1-piperazineethanesulfonic acid
IAP	intramembrane aspartyl proteases
IP	intramembrane proteases
kDa	kilodalton
LPR	lipid to protein ratio
MCMJR1SPP	*Methanoculleus marisnigri JR1* SPP

MES	2-(N-morpholino) ethanesulfonic acid
mg	milligram
$MgCl_2$	Magnesium chloride
MHC	major histocompatibility complex
mg	milligram
mL	milliliter
mM	millimolar
MWCO	molecular weight cut-off
NaCl	sodium chloride
NaN_3	sodium azide
NMR	nuclear magnetic resonance spectroscopy
OPDM	octyl thioglucopyranoside photosystem II in dodecyl maltoside
OTG	octyl β-D-thioglucopyranoside
OTG-PSII	OTG-photosystem II
PDB	Protein Data Bank
PSII	photosystem II
RNA	ribonucleic acid
SNR	signal to noise ratio
SPA	single particle analysis
SPP	signal peptide peptidase
TEM	transmission electron microscopy
TX-100	Triton X-100

SUMMARY

Different cryo-EM techniques can be employed to study a wide range of biological samples. This study uses two-dimensional (2D) electron crystallography and single particle cryo-EM to study two different membrane proteins.

Signal peptide peptidase is a small membrane protease capable of hydrolyzing various substrates in a hydrophobic environment. This protein is involved in different pathways and can serve as intervention point for different diseases. Because it is a small membrane protein, it has to be crystalized for structure determination. The 2D crystallization by dialysis approach was employed to reconstitute *Methanoculleus marisnigri JR1* SPP (MCMJR1SPP) into a phospholipid bilayer and 2D crystallization parameters were optimized to obtain significantly improved 2D crystals. These parameters included lipid to protein ratio (LPR), pH, temperature, glycerol and salt concentrations.

Photosystem II (PSII) is a large membrane protein complex found in photosynthetic organisms. It plays a key role in photosynthesis by oxidizing water to provide electrons for the electron transport chain in the light dependent reaction. This same process forms oxygen gas. Recent advancements in cryo-EM have made it possible to study this protein by single particle cryo-EM. This approach resulted in structures of 3 different PSII samples that show the overall architecture of the complex and location of critical extrinsic subunits.

CHAPTER 1: INTRODUCTION

1.1 METHODS FOR PROTEIN STRUCTURE DETERMINATION

The three-dimensional structure of a biological macromolecule plays a key role in their function. Thus, structural studies of macromolecules are very important. Not only does the knowledge gained from these studies help us to understand how these macromolecules work, but also how to target these macromolecules and modulate their function[1]. Furthermore, structural biology allows us to understand how these macromolecules interact with one another.

Three structural biology methods are frequently used to determine the three-dimensional structure of macromolecules: X-ray crystallography, electron cryo-microscopy (cryo-EM), and nuclear magnetic resonance (NMR) spectroscopy. These structural biology methods have made it possible to determine and understand the structures and functions of many biological macromolecules[2-5]

In this research cryo-EM was applied to the study of two different membrane proteins, signal peptide peptidase (SPP) and photosystem II (PSII). The cryo-EM method two-dimensional (2D) electron crystallography was applied to SPP. The PSII structure was studied intensively by single particle cryo-EM.

1.2 CRYO-EM

Cryo-EM has increasingly contributed to the structure determination of proteins over especially the past decade. It has been of particular value for studies of samples such as viruses, large protein complexes, proteins with conformational variability, membrane proteins, and cellular structural studies. Depending on the kind of sample, one of four cryo-EM methods is

applied: cryo electron tomography[6-11], 2D electron crystallography[12-16], microED[17-20], and single particle analysis[3, 21-24]. The approach is chosen based on the specific sample and these methods can be combined to study a very wide range of biological samples, from cells to protein structures and their interactions[25].

1.3 SINGLE PARTICLE CRYO-EM

Cryo-EM studies of proteins require and are typically preceded by purification and biochemical characterization of the protein of interest. Larger protein complexes such as PSII are often studied by single particle cryo-EM. The definition of "large" for cryo-EM is changing with time and basically describes the possibility to identify and analyze individual particles. The advent of phase plates and novel data collection approaches have contributed to dramatically redefine the size of particles that can be studied by single particle cryo-EM[26-29]. Single particle cryo-EM samples of membrane proteins are studied either in detergent or are reconstituted into lipid bilayers[30]. The PSII under investigation here was studied in the detergent-solubilized state by single particle cryo-EM. The cryo-EM approach of 2D electron crystallography requires a 2D crystallization step[12, 13, 31-34].

As a first step in single particle cryo-EM, the sample is studied by negative stain transmission electron microscopy (TEM) in order to obtain information on sample distribution, potential aggregation, and general suitability for cryo-EM[35-37]. Then the sample concentration and distribution are optimized for cryo-EM grid preparation for which the sample is flash-frozen in vitreous ice [38, 39]. Initial cryo-EM studies are often carried out with 120kV or 200kV cryo-EMs to optimize cryo-EM grid ice thickness in addition to protein concentration and distribution[40]. The sample is usually prepared using cryo-EM grids with perforated carbon

film[41]. The goal is to suspend the sample in vitreous ice inside the perforated holes for image data collection. The molecules ideally have random orientations in the vitreous ice of the cryo-EM grids[42]. Once suitable cryo-EM grid conditions have been identified, data collection on a 300kV cryo-EM equipped with a direct electron detector is used to obtain image data at the highest possible resolution[43-45]. Many recent structures are in the ranges of 3-4Å resolution[4, 46-48] Images are then analyzed for quality and areas of interest are identified. The best images in terms of image quality, ice thickness, sample concentration, and areas of mostly vitreous ice vs. carbon film are selected and analyzed by image processing for which various image processing software options exist [49-54]. The resolution of the resulting 3D reconstruction will depend on the sample preparation. This includes the sample purification, cryo-EM grid preparation, data collection, and image processing.

Cryo-EM Single Particle Analysis Flowchart

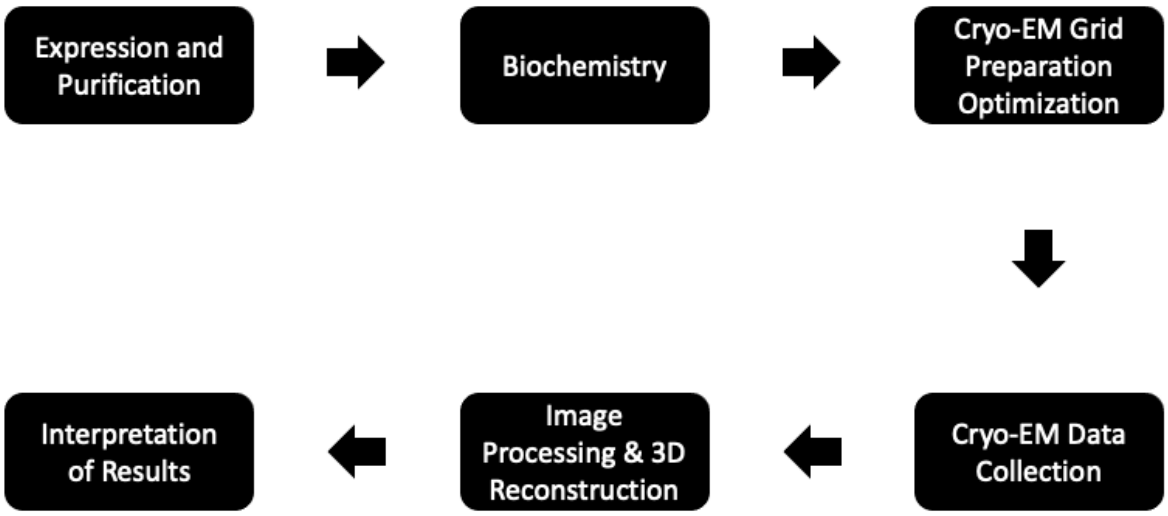

Figure 1.1. Cryo-EM single particle analysis flowchart. In order to determine the structure of a functional protein, first it is expressed and purified. Then the sample is tested for activity. In the third major step, optimal cryo-EM grid conditions are determined, followed by Cryo-EM data collection. In the two final steps, the images are processed, and a 3D reconstruction is generated and interpreted.

1.4 2D ELECTRON CRYSTALLOGRAPHY

Membrane proteins, which are too small for single particle cryo-EM, can be studied by 2D electron crystallography. Once a membrane protein has been purified, it can be incorporated into a phospholipid bilayer in order to induce 2D crystallization [31-33, 55-58]. The most popular method for 2D crystallization is reconstitution through dialysis. First the membrane protein of interest is solubilized and purified. Then the solubilized membrane protein is mixed with detergent-solubilized phospholipids. The protein/lipid/detergent mixture is then transferred into a semipermeable dialysis tubing. The dialysis tubing is placed inside a beaker containing a much larger volume of detergent-free buffer and incubated in a controlled environment for an extended time. During this period, the detergent is removed from the dialysis tubing, and the membrane protein is reconstituted into the phospholipid bilayers. Under the right conditions, 2D crystals can form and be used for structure determination.

Many parameters that affect crystal quality and size need to be considered. These parameters include the protein, lipid, and buffer components as well as temperature. The effect of these different parameters on the crystal quality and size have to be screened and evaluated[31]. Each parameter is optimized to obtain the best possible 2D crystals. The 2D crystallization conditions require thorough screening by negative stain TEM[59].

In order to determine the structure of membrane proteins using 2D electron crystallography, large (ideally 1-10 μm) and highly ordered single or double-layered 2D crystals are required. As different crystallization parameters are tested, their effect on the crystal quality and size have to be evaluated[59]. Once large and well-ordered crystals are obtained, the sample is prepared using cryo-EM for high resolution data collection[60-62]. Cryo-EM grids are

prepared with the back-injection method[61, 63, 64]. Images are then collected using a 300kV electron cryo-microscope and processed[52, 65] with the MRC program suite or 2DX[52, 66].

Membrane proteins subjected to 2D crystallization experiments can form single or double-layered 2D crystals, stacks of 2D crystals, or three-dimensional crystals[67]. It may be possible to collect and analyze data from small three-dimensional crystals using MicroED[17, 19, 20]. A number of important membrane protein structures have been determined using 2D electron crystallography[5, 68-71].

2D Electron Crystallography Flowchart

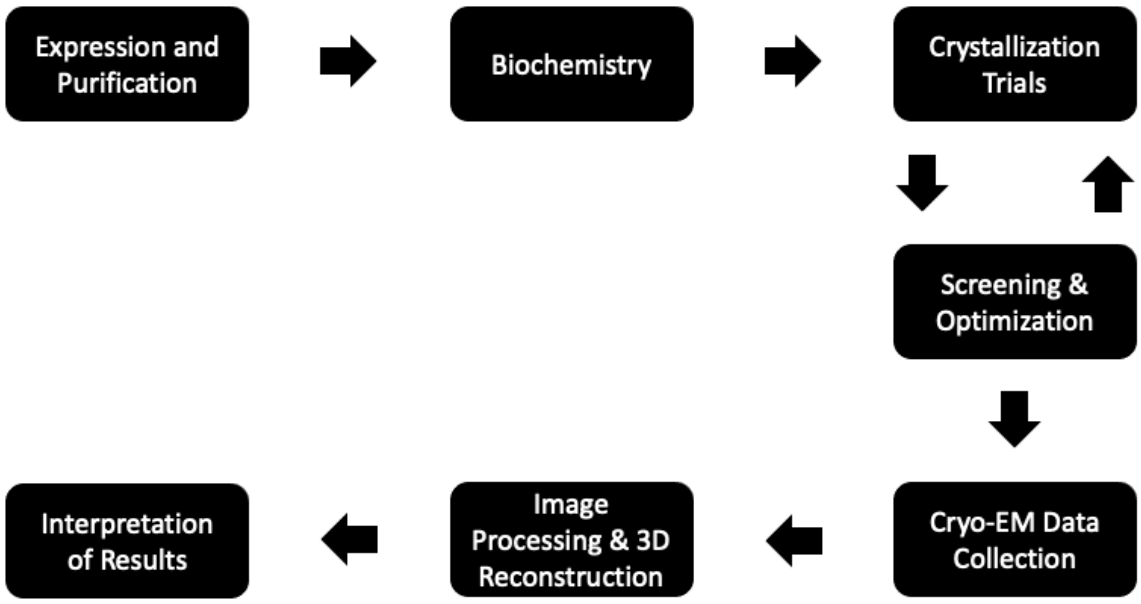

Figure 1.2. 2D electron crystallography flowchart. In order to determine the structure of a membrane protein, first it is expressed and purified. Then it is characterized for purity and activity. In the next step, two-dimensional crystallization trials are conducted to grow large well ordered 2D crystals. Once this is achieved, cryo-EM grids are prepared by back-injection, cryo-EM data is collected, the images are processed, and a 3D reconstruction is generated and interpreted.

1.5 CHALLENGES IN CRYO-EM

While Cryo-EM is a very powerful technique for determining protein structures, there are major hurdles at different stages of structure determination. These challenges can be at the sample preparation, data collection, and/or image processing steps.

1.5.1 SAMPLE PREPARATION

When imaging macromolecules by cryo-EM, they have to be in a solid state. This presents a problem because biological molecules function in an aqueous environment. The samples can be either dehydrated or flash frozen to achieve a solid state. Negative stain methods[35, 37] are used to prepare biological molecules for fast and efficient initial screening and characterization. For high resolution data collection, the samples are vitrified. It is crucial that the flash freezing is rapid to obtain vitreous ice[38, 39].

Sample distribution and ice thickness need to be carefully adjusted and the overall sample preparation has to be highly reproducible[42]. Controlling the sample preparation environment via automation of grid preparation increases sample preparation reproducibility and reduces the required training[72] Several efforts are underway to automate the entire process[45, 72, 73]. This will reduce human error and make sample preparation more reproducible. The amount of sample required for sample preparation may also decrease for new, automated devices.

1.5.2 DATA COLLECTION

When electrons come in contact with the sample, they can be scattered elastically or inelastically. During elastic scattering, the electrons interact with the sample and are scattered with the same energy they had before they interacted with the sample. However, during inelastic scattering, the electrons coming from the beam transfer some of their energy onto the sample. The transferred energy excites electrons within the sample and results in covalent bond breakage. This starts a cascade of events that ultimately destroys the sample. Most of the electrons coming from the beam are scattered inelastically by the sample. This results in rapid sample degradation. Furthermore, as the sample is being imaged, the radiation damage increases over time[39].

In order to minimize the radiation damage, the sample has to be imaged under low electron exposure/dose. However, this leads to another problem. Imaging with low electron exposure results in images that have poor quality. These images have a low signal to noise ratio (SNR). Furthermore, biological molecules are made up of light elements such as hydrogen, carbon, oxygen, nitrogen and sulfur. Compared to heavier elements, these elements have poor scattering properties. Because of these reasons, the collected electron micrographs have poor signal. However, with image processing, the signal can be enhanced, and high-resolution structures can be attained.

1.5.3 IMAGE PROCESSING

Even though individual cryo-EM electron micrographs have poor SNR, information from different images can be combined to enhance the signal. In single particle analysis, individual electron micrographs contain the particles of interest in different orientations. However, the information from individual particles alone is not sufficient for high resolution structure

determination. Information from a large number of different particles that have the same orientation have to be averaged to enhance the signal that is used for 3D structure determination. This is achieved in the class averaging step of image processing[74].

In class averaging, particles that have the same orientation are aligned and then averaged. Each particle has five alignment parameters (x, y, translation and 3 Euler angles (psi, theta, and phi)). The particles are first rotated clockwise on different axes for proper alignment. In the next step, the relative orientation of the class averages with respect to each other is determined. For the 3D reconstruction of the sample, the Fourier transform of each class average is determined. Then the Fourier transforms of these class averages are used to obtain the three-dimensional reconstruction of the sample. This process starts by taking the Fourier transform of the first class average to determine the phase and amplitude information. Then this information is plotted in reciprocal space. In the next step, the Fourier transform of the second class average is determined and the phase and amplitude information is plotted in reciprocal space. The relative orientation of the first and the second class averages can be determined because they share a common line of phases and amplitudes. This is known as the law of common lines[75, 76]. Sinograms can be used to find the relative orientation between two Fourier transforms by making it possible to find the common line of phases and amplitudes shared between two transforms.

Once the common line of phases and amplitudes of the first two class averages are determined, the Fourier transform of the third class average can be used to determine the common lines between the first and third class average as well as the second and third class average. This information is plotted in reciprocal space along with the first two class averages. Then the Fourier transform of the fourth-class average is determined and the phase and amplitude information are plotted in reciprocal space with respect to the first three class average

information. The rest of the class average are plotted using the same process. Usually, many class averages are required as individual class averages provide different orientation of the sample [49-51].

Another interesting challenge in cryo-EM is the strategy for discarding low-quality data to optimize each individual image before selecting the best image in terms of resolution, sample concentration and distribution, and sample location in vitreous ice. During data collection, multiple frames, also referred to as “movie’, are captured from one area of interest. The first few frames have the least amount of radiation damage yet suffer from sample drift. The later frames have the least drift, but the radiation damage is high. Approaches have been developed to automatically exclude the first and last few frames during their image processing stage to obtain a higher resolution than when using all of the frames, and the remaining frames can be aligned to account for sample movement between frames, which is described in the next section[77].

1.6 RECENT ADVANCES IN CRYO-EM

Recent advances have propelled Cryo-EM forward as a prominent structural biology technique for various samples. In 2017, the Nobel prize in chemistry was awarded to Jacques Dubochet, Joachim Frank, and Richard Henderson for their contributions to cryo-EM.

The introduction of direct electron detectors[78-81], automated data collection[44, 82], algorithms that correct sample movement caused by the electron beam[77] and various image processing software[49-51] have made cryo-EM an extremely powerful technique in structural biology. Prior to direct electron detectors, researchers used film[83] and charged-coupled device (CCD) cameras[84, 85]. Direct electron detectors have better detective quantum efficiency (DQE) than CCD cameras and higher efficiency than film [78]. In addition, these direct electron

detectors can be used to collect images at high frame rates. This makes it possible to collect many images in the form of a movie for each area of interest[86]. After data collection, the subframes of each movie can be processed to correct for sample movement that takes place during data collection. This process is called frame alignment. By aligning the subframes the quality of the data is enhanced to give a high-resolution structure of the sample. Using direct electron detectors, researchers have been able to improve the structures of many well-studied samples to a substantially higher resolution[77].

1.7 PDB STRUCTURE JUMP

As of February 2021, 174,293 structure entries have been deposited in the Protein Data Bank (PDB) (***figure 1.3***). Of these structures, 95,550 were determined between 2012-2020. Thus, 55% of the structures were solved in the past 9 years. Until 2010, there were only 320 cryo-EM structures in the PDB. Now there are more than 6,911 structures (***figure 1.4***). In 2020 alone, approximately 2,390 cryo-EM entries have been deposited in the PDB. Until recently, the number of membrane protein structures in the PDB was less than 1% of total entries[87]. However, major advances in structural biology are beginning to change that[82]. This is important since an estimated 20-30% of the genes in most organism genomes code for membrane proteins[88, 89].

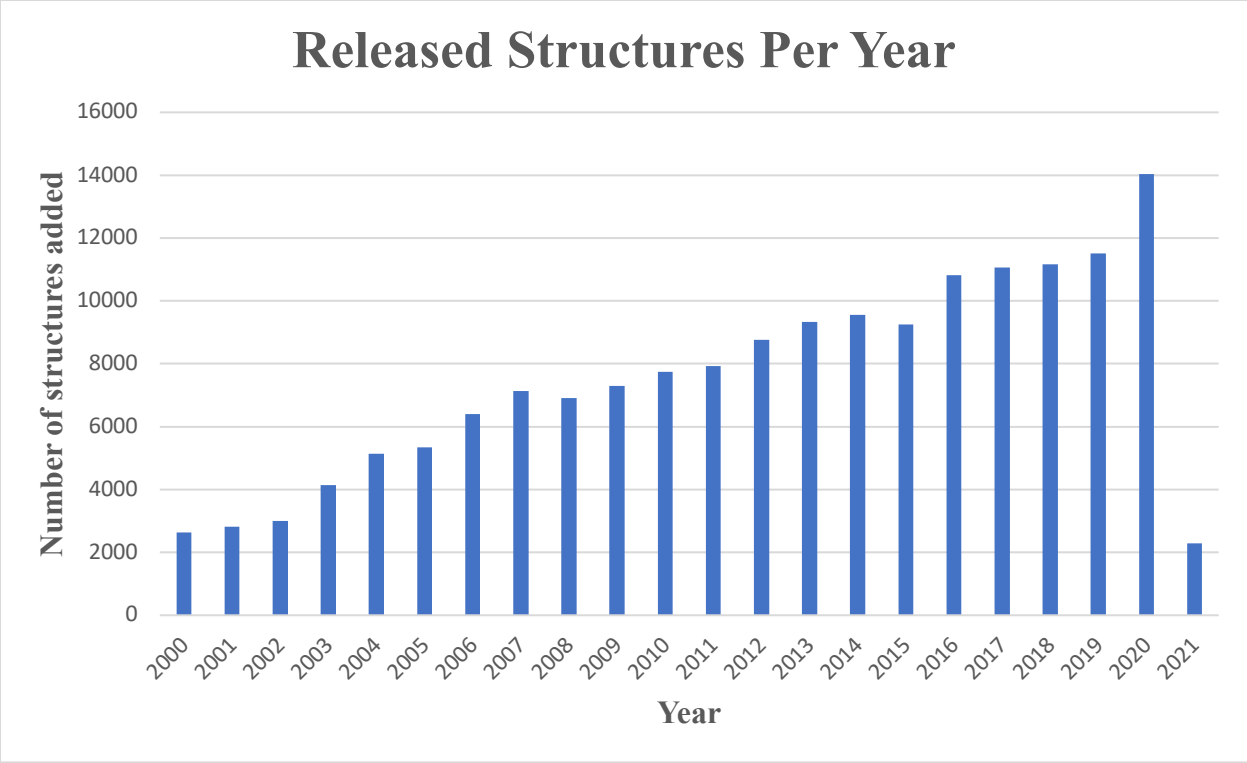

Figure 1.3. Overall growth of structures released by year. There are 174,294 structures in the PDB as of February 2021. In the past 10 years, the number of new structures added has increased rapidly due to improvements in structure determination techniques.

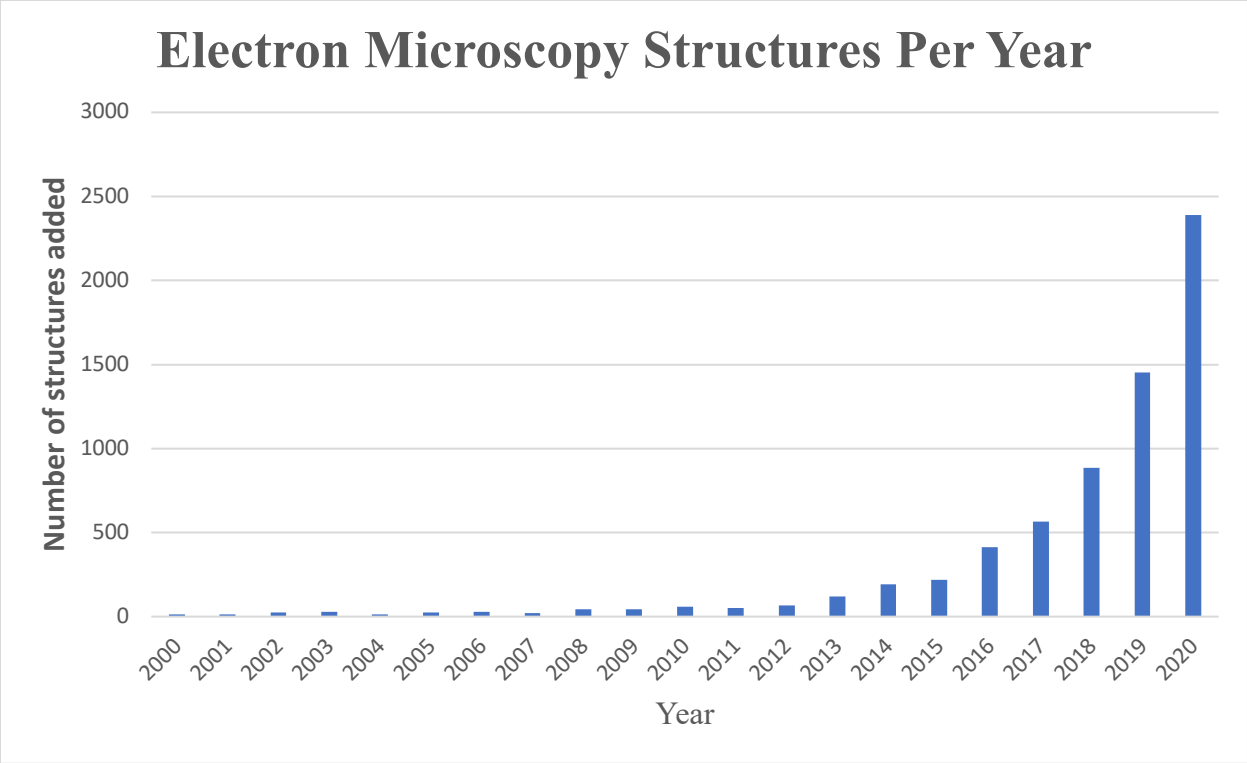

Figure 1.4. Overall growth of cryo-EM structures released by year. Currently, there are 6911 EM structures in the PDB. Of these, nearly one third (2,390) were determined in 2020.

1.8 MEMBRANE PROTEINS

The focus of this study are membrane proteins. These proteins are responsible for a wide range of functions and are frequently considered important drug targets for a large number of diseases [90, 91]. However, membrane proteins pose substantial challenges in the different steps of structure determination. First, it is often not trivial to over-express and purify membrane proteins[92]. Once purified and functional protein is obtained, it may still be challenging to purify the protein in large quantities, which limits crystallization studies for structure determination[31, 93]. Second, preventing aggregation and keeping membrane proteins active is an additional challenge[94, 95]. Chapter 2 focuses on 2D crystallization studies of

Methanoculleus marisnigri JR1 Signal Peptide Peptidase (MCMJR1SPP) and chapters 3 and 4 focus on single particle analysis (SPA) cryo-EM of photosystem II (PSII) complexes.

CHAPTER 2: TWO-DIMENSIONAL CRYSTALLIZATION OF SIGNAL PEPTIDE PEPTIDASE

2.1 INTRODUCTION

Membrane proteins carry out a wide range of biological functions. A specific group of membrane proteins capable of cleaving substrates are known as intramembrane proteases (IPs)[96, 97]. These IPs are capable of catalyzing hydrolysis reactions within the transmembrane regions[98]. As hydrolysis reactions require water, the fact IPs are able to do this in a hydrophobic environment makes them unique. However, the detailed mechanism of how this reaction happens is not known.

Four kinds of IPs have been identified: serine proteases, glutamate proteases, zinc metalloproteases, and aspartyl proteases[99, 100]. IPs are found in the endoplasmic reticulum (ER), Golgi apparatus, and cell membranes. The substrates of these IPs are membrane bound[101]. When these substrates are cleaved by IPs, they are released from the membrane in fragments into the cytoplasm or outside the cell where they can carry out their biological functions[97].

This chapter focuses on 2D crystallization studies of one of these four IPs: intramembrane aspartyl proteases (IAPs). These proteases cleave their substrates within the lipid bilayer[102]. Members of the IAP family share important features. They have conserved active site motifs: YD and GxGD residues on consecutive transmembrane helices as well as a PAL motif near their C-terminal end[103]. These motifs are important for the IAP hydrolysis reaction[99, 104]. The motifs are conserved across different species[105, 106]. Members of the IAP family are involved in various diseases such as Alzheimer's disease and hepatitis C virus

maturation and can be key intervention points for these diseases. Because of this, it is important to study and understand their mechanisms.

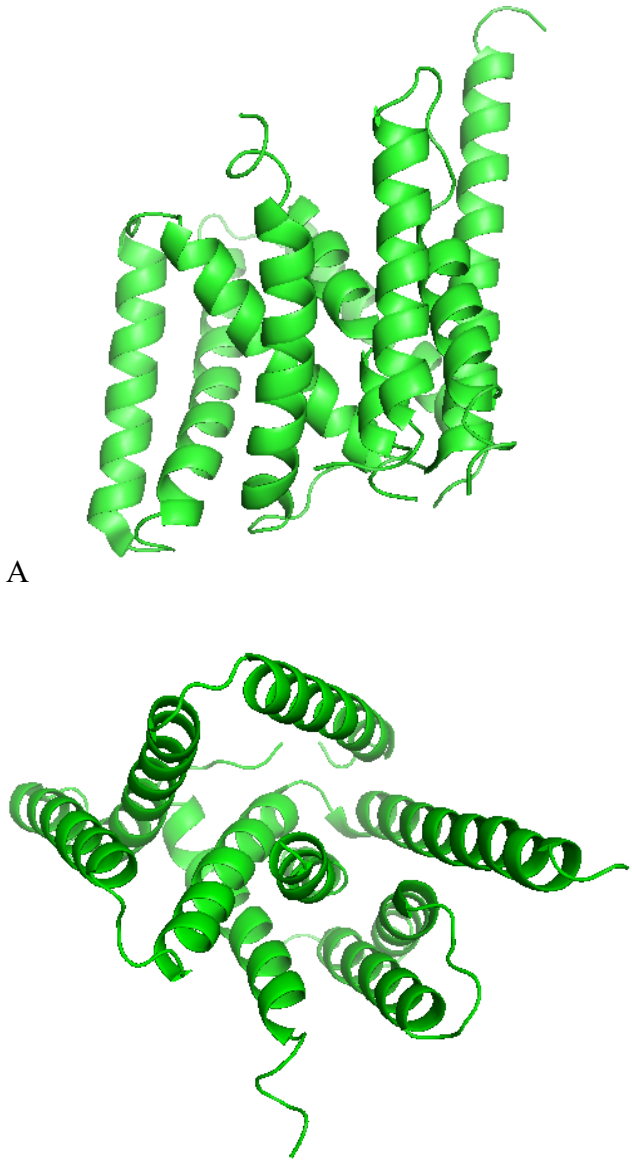

Figure 2.1. Secondary structure of MCMJR1SPP (PDB ID: 4HYC), which has nine transmembrane helices. **A** shows the side view and **B** shows the top view (perpendicular to the plane of the membrane).

One of the key members of the IAP family is γ-secretase. It is composed of four subunits: presenilin, anterior pharynx-defective1 (Aph-1), nicastrin, and presenilin enhancer 2 (PEN-2)[107] (***figure 2.2***). Presenilin is the active subunit. The γ-secretase complex as a whole is responsible for the formation of various species of amyloids[108]. Beta-secretase cleaves amyloid precursor protein (APP). In the process, C100 is produced[109, 110]. This C100 is presented to γ-secretase as a substrate. Then it is cleaved to generate amyloid beta (Aβ) proteins. Depending on where C100 is cleaved, different species of amyloid beta proteins are generated[111]. When C100 is cleaved at the γ site Aβ 42 is generated. This Aβ42 is more likely to aggregated than other species of Aβ. Aβ aggregation leads to the formation of amyloid plaques. These plaques are thought to cause neuron deaths, which is associated with Alzheimer's disease[112].

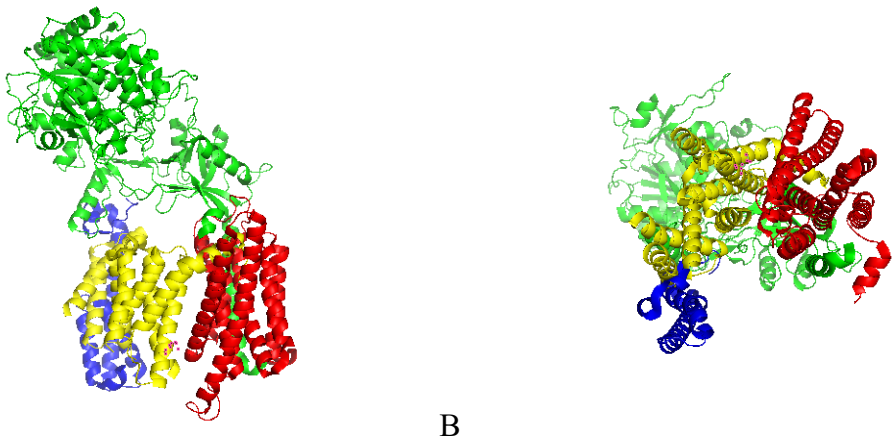

A B

Figure 2.2. Gamma secretase subunits (PDB ID: 5A63): Presenilin (Yellow), Aph-1 (Red), nicastrin (Green), and PEN-2 (Blue). **A** shows a side view and **B** shows a top view (perpendicular to the plane of the membrane).

Signal peptide peptidase (SPP) is another member of the IAP family. It is responsible for cleaving signal peptides. When membrane proteins are synthesized, the N-terminal sequence is cleaved by signal peptidase[113]. SPP cleave the remnant membrane-embedded signal peptide.

As a result, the cleaved peptides are released from the membrane. This is how major histocompatibility complex (MHC) class 1 molecules are released from the endoplasmic reticulum (ER) membrane[97]. When hepatitis c virus infects cells, it takes advantage of this mechanism to complete its assembly[114, 115].

SPP and presenilin share key similarities. Even though they do not have many sequence similarities, they have similar active sites. They both have 9 transmembrane helices. The conserved YD and GxGD active site residues are located on transmembrane helix 6 and 7 respectively for both proteins. Furthermore, they are inhibited by the same molecules[116-118]. They are also able to process the same substrates[104]. Amyloid precursor protein (APP) is a prime example[119]. Interestingly, presenilin and SPP have opposite orientations inside the membrane[120]. The C-terminal end of SPP faces the cytosol while the c-terminus of presenilin faces away from the cytosol (***figure 2.3***). This determines the type of membrane proteins these enzymes cleave. SPP cleaves type I membrane proteins while presenilin cleaves type II membrane proteins.

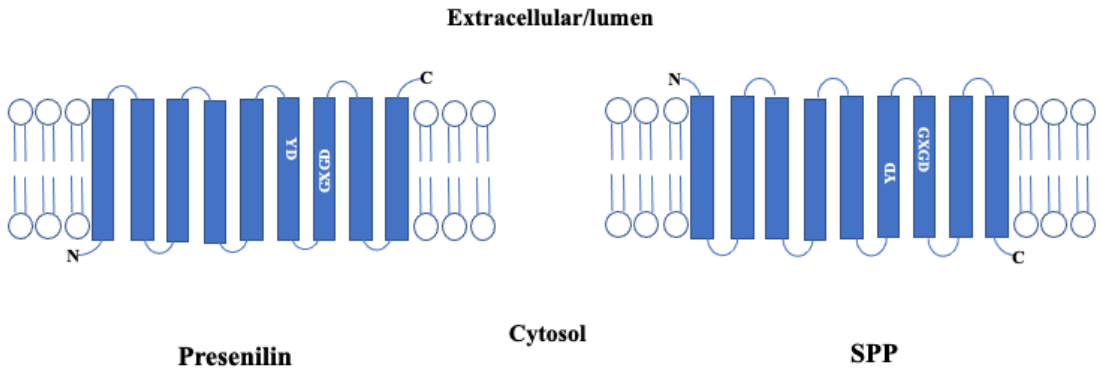

Figure 2.3. Presenilin and SPP have opposite membrane orientations. Because of this, SPP cleaves type I substrates and presenilin cleaves type II substrates.

While both proteins are membrane proteins and are challenging to work with, it is much more difficult to work with presenilin than SPP. Because presenilin is part of the γ secretase complex, it is extremely difficult to express and purify in its functional state. SPP on the other hand is not part of a complex and is somewhat easier to express and purify. Structural studies require a large amount of homogenous sample for crystallization trials. This makes microbial homologs such as *Methanoculleus marisnigri JR1* SPP (MCMJR1SPP) convenient samples for structural studies in order to understand the IAP family reaction mechanism.

Several structures of SPP and presenilin (γ-secretase) have been solved to date [121-124]. However, these structures are not of the wild-type enzymes. Several mutations and modifications have been made to make the protein more stable for structural studies. Furthermore, they are solubilized in detergent and appear to be inactive (***figure 2.4***). For example, the catalytic residues are thought to be too far apart to carry out the protein reaction mechanism.

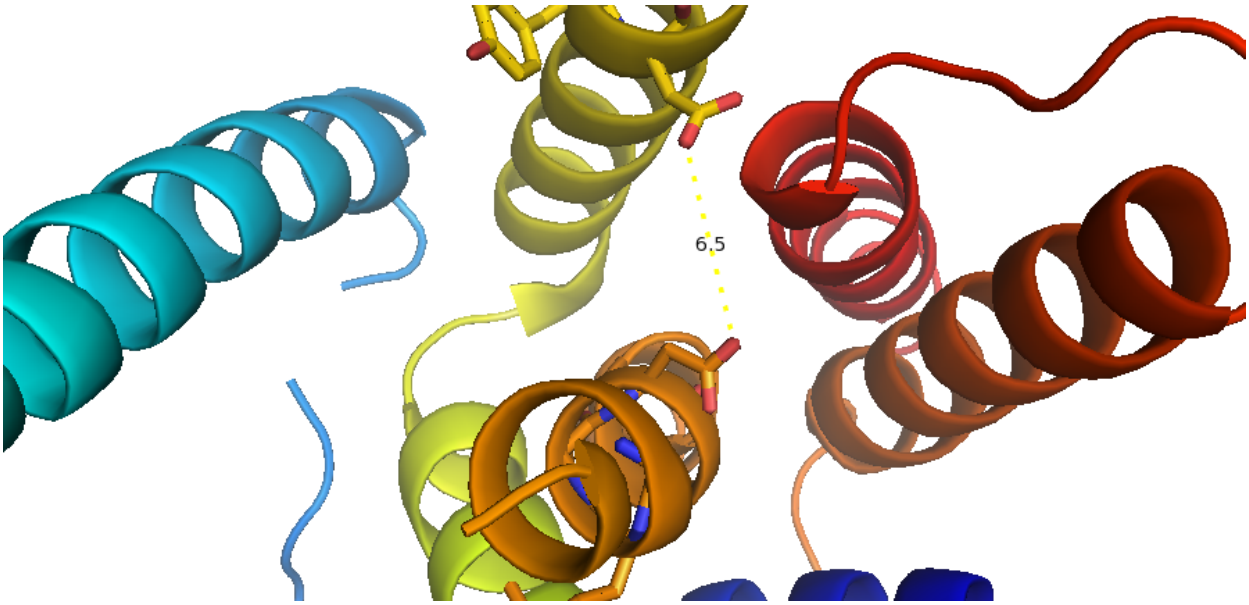

Figure 2.4. MCMJR1SPP (PDB ID: 4HYC) active site (YD, GxGD). The two aspartic acid residues are 6.5Å apart, suggesting this to be a structure of inactive MCMJR1SPP.

The goal of this research is to determine 2D crystallization conditions in order to determine the structure of wild-type SPP within a lipid bilayer. Two-dimensional crystallization offers the opportunity to study membrane proteins within a phospholipid bilayer[31-33], which constitutes conditions of a near-native environment[31]. For SPP, the 2D crystal structure may also shed light on how water enters the hydrophobic environment and takes part in the reaction mechanism. Two-dimensional crystallization experiments of SPP, which are a prerequisite to structure determination by 2D electron crystallography, are described here.

2.2 MCMJR1SPP EXPERIMENTAL PROCEDURES

2.2.1 MCMJR1 SPP EXPRERESSION AND PURIIFICTATION

Methanoculleus marisnigri JR1 SPP (MCMJR1SPP) was cloned and expressed in *E. coli* Rosetta 2 cells (Novagen) in Dr. Raquel Lieberman's laboratory by Sibel Kalyoncu and Swe-Htet Naing [125, 126]. After purification, the MCMJR1SPP samples were in a buffer containing 20 mM Hepes, 250 mM NaCl, 0.05% DDM, pH7 (gel filtration buffer) and the fractions (fractions 10-13) were kept separate (instead of combining and concentrating). Protein concentrations ranged between 0.1-1mg/mL. Then MCMJR1SPP samples were aliquoted into 100 µL volumes and flash frozen using liquid nitrogen. Then samples were stored in -80° C freezer until dialysis experiments were conducted.

2.2.2 MCMJR1SPP TWO-DIMENSIONAL CRYSTALLIZATION

For each dialysis experiment, 4 different conditions were tested. Four 100 µL aliquots and detergent solubilized (0.5% Na-deoxycholate) 1,2-dimyristoyl-sn-glycero-3-phosphocholine (DMPC) (10 mg/ml) were thawed on ice. The LPR was calculated for each condition using the formula below:

$$LPR = \frac{(\frac{C_{lipid} * V_{lipid}}{M.W_{lipid}})}{(\frac{C_{protein} * V_{protein}}{M.W_{protein}})}$$

LPR = lipid to protein ratio C_{lipid} = lipid concentration
V_{lipid} = lipid volume $M.W_{lipid}$ = lipid molecular weight
$C_{protein}$ = protein concentration $V_{protein}$ = protein volume
$M.W_{protein}$ = protein molecular weight

Detergent-solubilized DMPC was pipetted into each aliquot. Then the protein/lipid/detergent mixtures were gently vortexed and left on ice for 10 minutes. Dialysis tubing was cut and placed in a 1 L beaker containing deionized water for hydration.

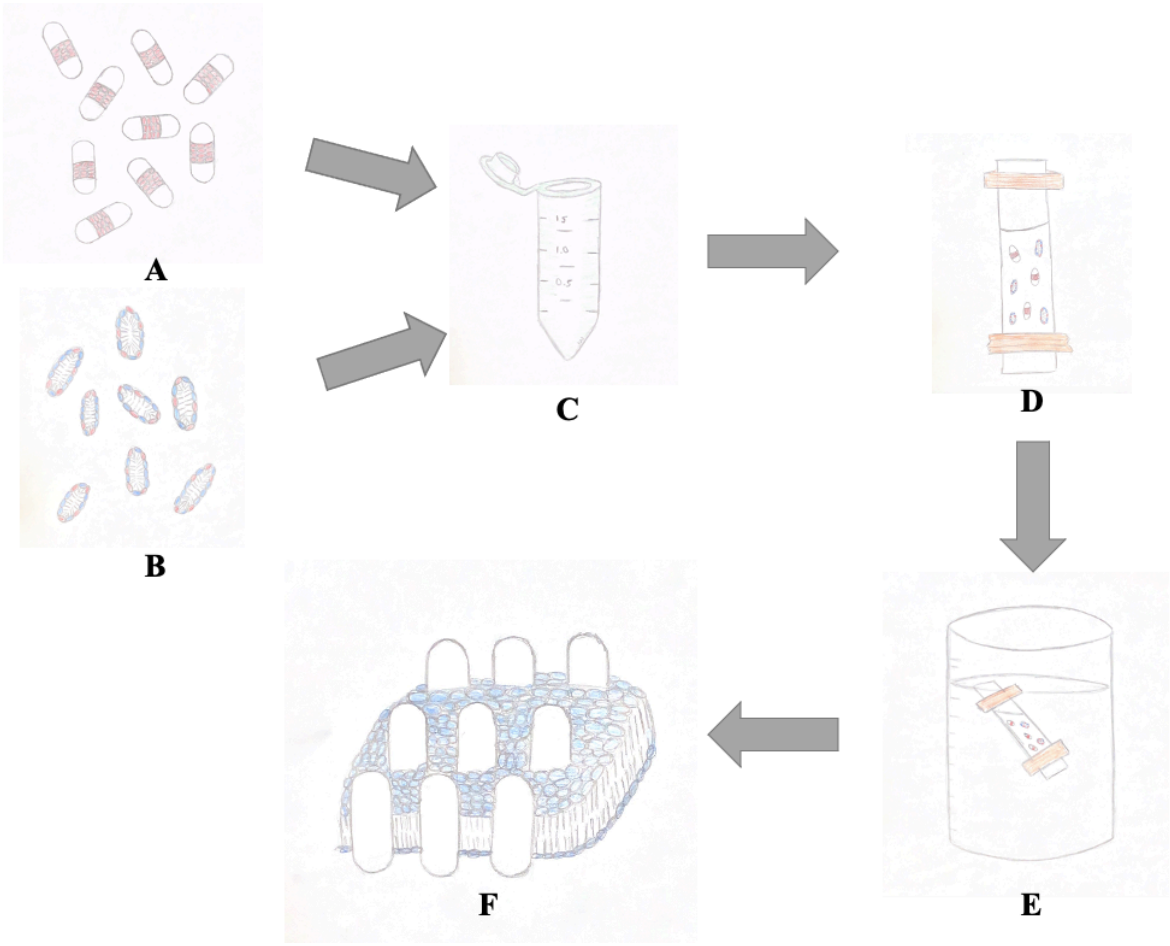

Figure 2.5. Two-dimensional crystallization by dialysis. Detergent solubilized membrane proteins (A) and detergent solubilized phospholipids (B) are mixed together in an Eppendorf tube (C). Then the membrane protein-phospholipid-detergent mixture is transferred into semipermeable dialysis tubing (D). The dialysis tubing containing the sample is dialyzed in a large volume of detergent free buffer for several days (E). During this time, the detergent is removed from the dialysis tubing and the membrane protein is reconstituted into phospholipid bilayers. Under the optimal conditions, 2D crystals can form (F), which often contain ordered arrays of several thousand copies or more of the membrane protein. The membrane proteins are represented by white ovals and the detergent headgroups by orange circles. The phospholipid headgroups are represented by blue circles.

For each condition tested, 250 mL of detergent-free dialysis buffer was prepared and placed inside a 400 mL beaker. The dialysis buffer consisted of 100 mM NaCl, 5 mM $MgCl_2$, 5 mM NaN_3, 20% glycerol, pH 6. These buffer components can affect the crystal size and quality. Therefore, during some experiments, these buffer components were modified as outlined in Table 2.1.

Sample (volume)	Lipid to protein ratio (LPR)	NaCl	$MgCl_2$	NaN_3	pH	Temperature	Glycerol
MCMJR1SPP (100 µL)	0	100mM	5mM	5mM	6	24°C	20%
MCMJR1SPP (100 µL)	10	100mM	5mM	5mM	6	24°C	20%
MCMJR1SPP (100 µL)	20	100mM	5mM	5mM	6	24°C	20%
MCMJR1SPP (100 µL)	30	100mM	5mM	5mM	6	24°C	20%

Table 2.1. An example of 2D crystallization trial. Each dialysis experiment examined 4 different conditions for each crystallization parameter. The best condition was identified by screening, imaging and evaluating results by FFT for each condition. Then a follow-up experiment was set up to optimize that parameter.

The protein/lipid/detergent mixtures were carefully pipetted into dialysis tubing[31]. The dialysis tubing containing the sample was placed inside a beaker containing the detergent-free buffer and covered. The crystallization trials were incubated at 24°C for 14 days [127]. The temperature and the length of dialysis were modified (21-30°C and 11-22day respectively) in order to identify the optimal temperature and dialysis duration. Once dialysis was completed, negative stain TEM grids were immediately prepared.

2.2.3 MCMJR1SPP NEGATIVE STAIN TEM GRID PREPARATION

For the preparation of negative stain TEM grids, 2 μL of MCMJR1SPP sample was placed on a carbon-coated 400-mesh Cu TEM grid. The sample was gently spread across the grid using the edge of the pipette tip. After a 1 min incubation on the carbon-coated grid, the sample was blotted from the side using Whatmann #4 filter paper. Then the grid was stained with 2 μL 1% uranyl acetate for 30 seconds. Afterwards, the grid was blotted again from the side using Whatmann #4 filter paper. All grids were stored in a desiccator until screening and data collection.

2.2.4 MCMJR1SPP TEM IMAGING

After grid preparation, MCMJR1SPP samples were screened and imaged with a JEOL JEM-1400 transmission electron microscope (TEM) at 120kV and equipped with a Gatan Orius SC1000 and a 2k x 2k Gatan Ultrascan 1000.

Each grid was screened thoroughly, and areas containing membranes were used for image collection. Overview images of areas containing membranes were collected at low magnification (5000x-20,000x magnification). Of each of these overview areas, several high magnification images (50,000x-60,000x magnification) were collected to assess if the membranes contained 2D crystals.

2.2.5 MCMJR1SPP IMAGE EVALUATION

The MCMJR1SPP images were evaluated with DigitalMicrograph Software (Gatan Inc) and evaluated for membrane size and morphology as well as presence and quality of two-dimensional crystals. The overview images were used to assess the size of the membranes and

overall morphology while the high magnification images were used to evaluate the size and quality of potential 2D crystals by FFT[65]. The size and quality of order was noted for each image. ***Figures 2.6*** and ***2.7*** show examples of overview images of membranes and FFTs of crystals representing different qualities, respectively.

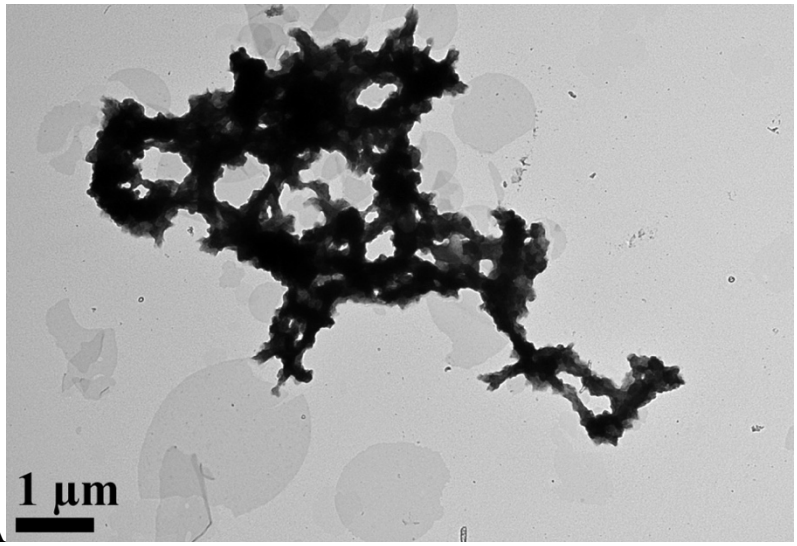

A

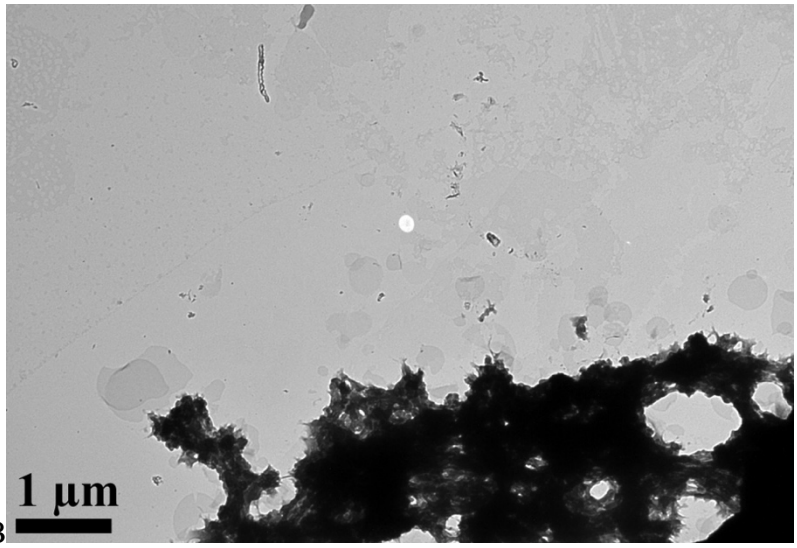

B

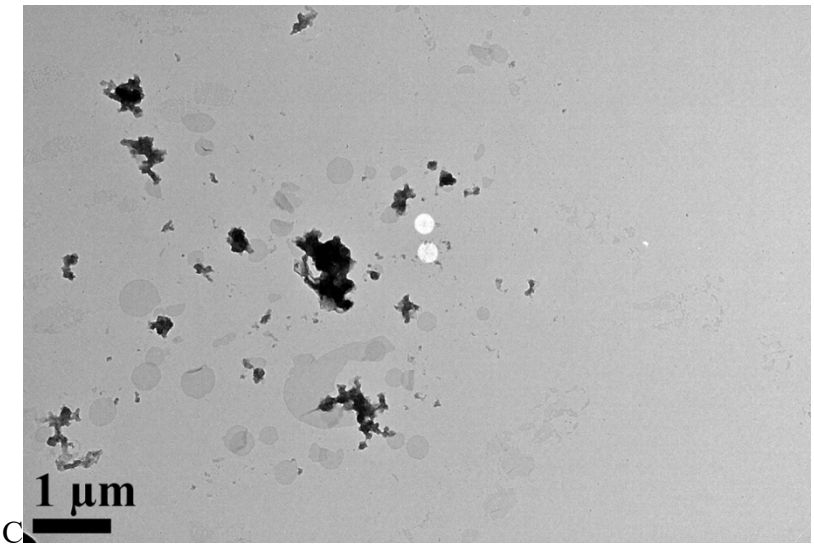

C

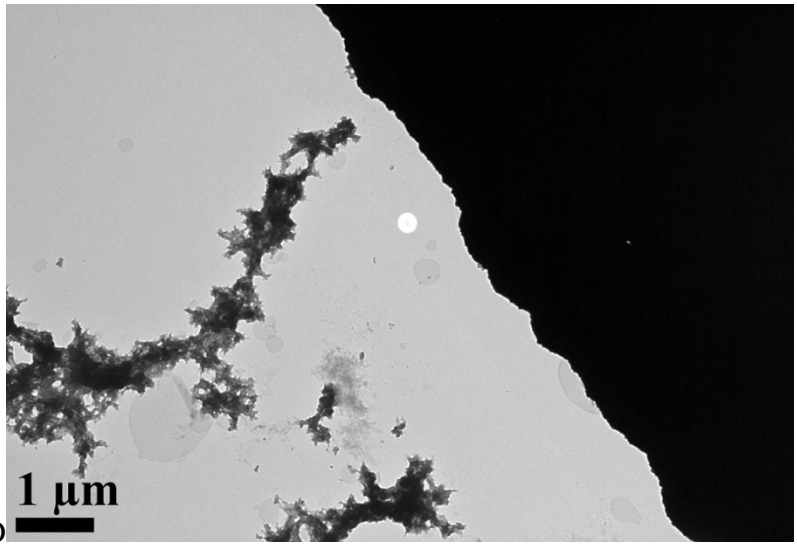

D

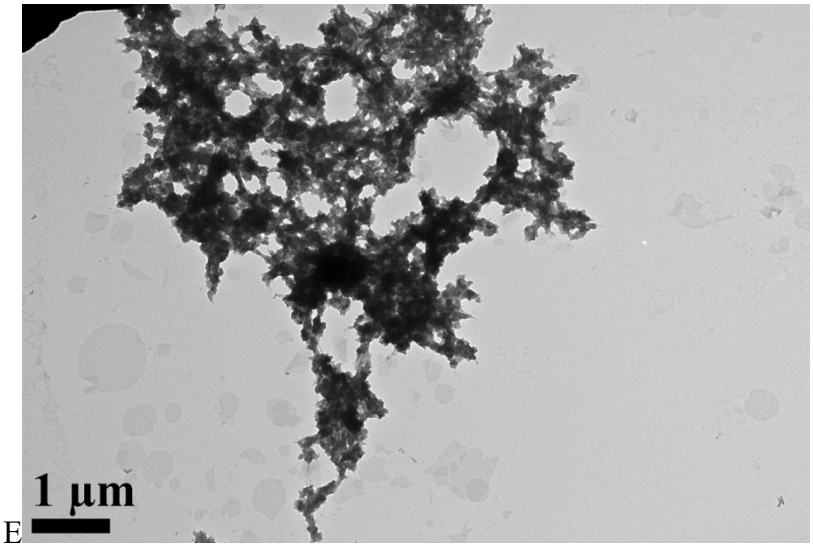

E

F 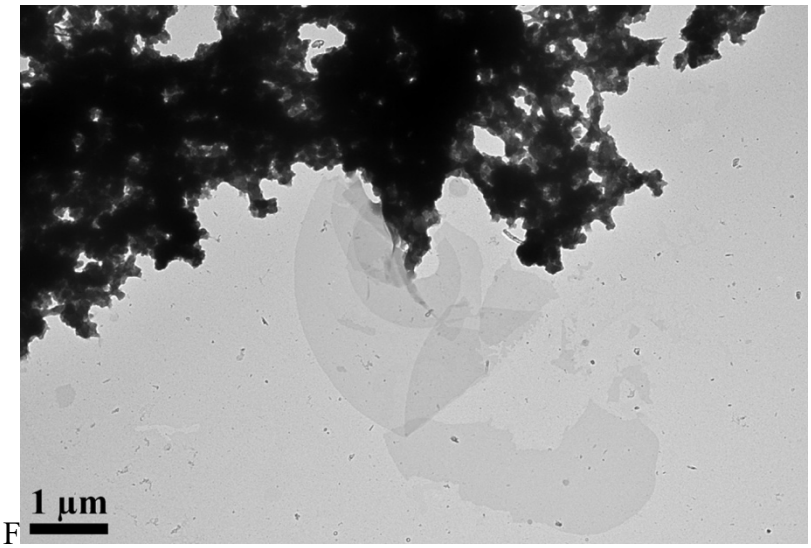

G 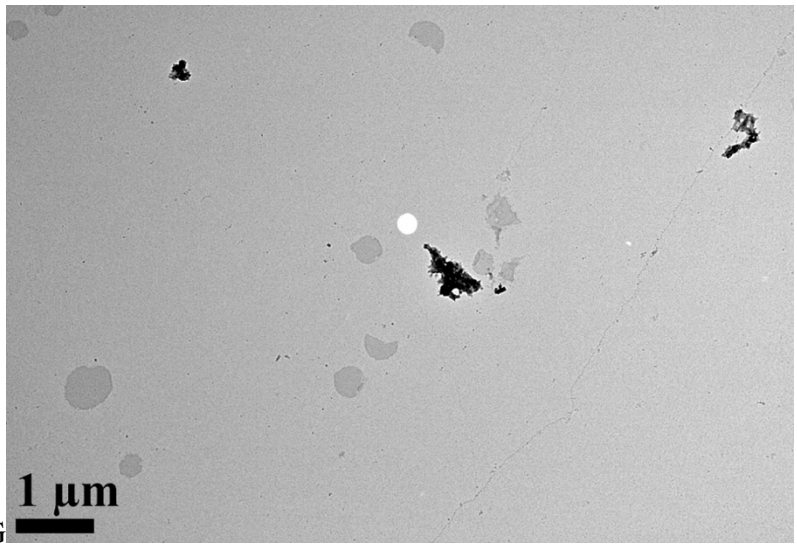

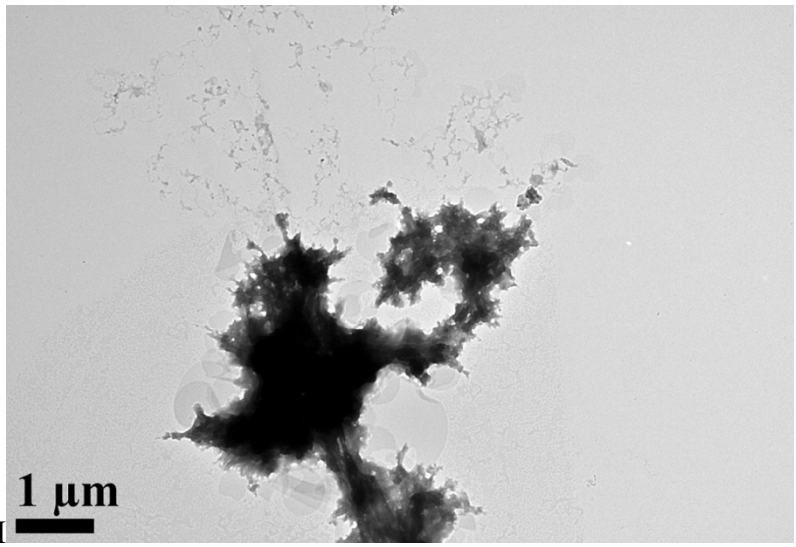

H

Figure 2.6. Different membrane morphologies from MCMJR1SPP crystallization trials (**A-H**). Examples of large membranes that are likely to contain 2D crystals. During screening, many images were collected from areas that resemble the images above.

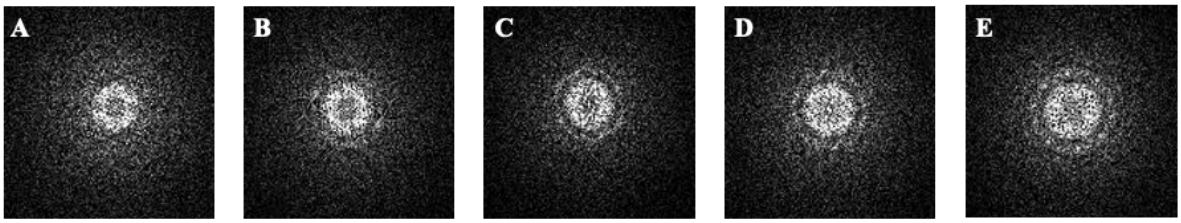

Figure 2.7. Fast Fourier Transform (FFT) quality. During image evaluation, each image was carefully inspected for the presence of 2D crystals, and the quality of these crystals were evaluated by FFT of membrane areas. A-E show examples of FFTs with increasing quality (A=1, B=2, C=3, D=4, E=5). A crystal with a quality of 1 is poor crystals and a crystal with a quality of 5 is a very good crystal.

2.2.6 MCMJR1SPP CRYSTALLIZATION CONDITION OPTIMIZATION

After each MCMJR1SPP image was evaluated, the dialysis condition that gave the best result was identified and the conditions were refined in the next experiment. This process was repeated until the optimal condition for the parameter was identified. Key parameters were reevaluated if another parameter resulted in a marked improvement.

2.3 RESULTS

The Lipid to protein ratio (LPR) was first tested. The first two experiments tested LPRs between 0-26 (LPRs 0,1,2,3,4,8,14, 26) from different fractions (10-13). Then follow-up experiments examined LPRs between 6-10 (LPRs 6,7, 9 and 10). It was determined that LPRs 6-8 and fractions 11 and 12 were optimal, based on membrane size and order. Representative images showing the overall size and morphology of membranes as well as crystal qualities are shown in ***figures 2.8, 2.9*** and ***2.10***. For every new purification, similar LPRs were tested, and shown to be reproducible.

Next, the pH was optimized as a crystallization parameter. Initial experiment tested pH values between 5-8 (pH 5,6,7, and 8). Follow-up experiments examined pH 5-7(pH 5.5, 6, 6.5, and 7). These experiments showed a pH value of both 6.0 and 6.5 was optimal. Representative images of these results are shown in ***Figures 2.11***, **2.12**, and **2.13**. The next 5 sets of experiments examined the effects of temperature. Temperatures between 21-30°C (21°,24°, 27°, and 30°C) were examined using LPRs 6 and 8. These experiments showed membrane size and crystal quality were best at a dialysis temperature of 27°C. ***Figures 2.14***, ***2.15***, and ***2.16*** are representative images from these studies showing the membrane size and morphology as well as the crystal quality.

The effects of glycerol (0%, 5%,10%, and 20% glycerol) were tested. Best results were between 10-20% glycerol. Representative images are shown in ***Figures 2.17*** and ***2.18***. Next, dialysis experiments examined the effects of NaCl. Experiments tested NaCl concentrations between 0-1M (0mM,50mM, 200mM, 250mM, 500mM, 750mM and 1M). NaCl concentrations between 200-250mM gave the best results. ***Figures 2.19***, ***2.20***, and ***2.21*** show the size and morphology of membranes as well as crystal qualities observed under these conditions.

Parameter	**Range Tested**	**Optimal Condition**
LPR	0-40	8
SPP concentration	0.1mg/ml-1mg/ml	0.5-1mg/ml
SPP fraction	10-13	11&12
NaCl concentration	0-1M	200mM
$MgCl_2$ concentration	0-50mM	5
pH	5-8	6
Temperature	21-30	27
Glycerol	0-20%	20%
Dialysis time	11-22 days	12 days

Table 2.2. Different 2D crystallization parameters tested to improve the quality and size of MCMJR1SPP crystals. For each parameter the range tested, and the optimal condition is identified.

LPR PARAMETERS

LPR3

A 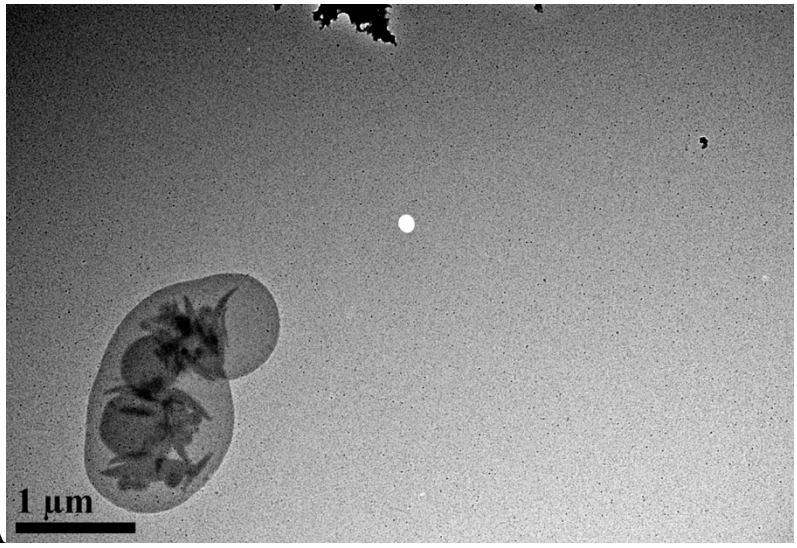

B 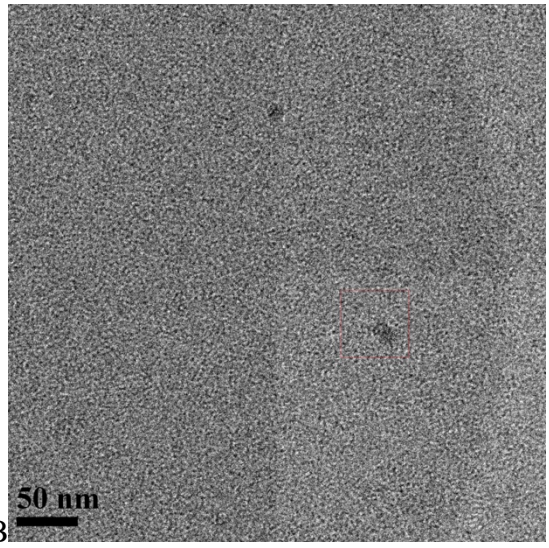

C 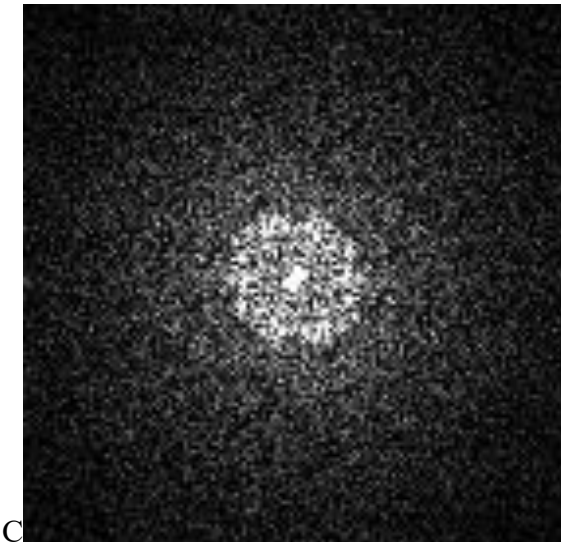

Figure 2.8. Representative micrographs from MCMJR1SPP LPR 2D crystallization trials. **A** shows an overview image of membrane size and morphology from the **LPR3** experiments. Several vesicles and sheetlike membrane can be observed. The scale bar corresponds to 1 µm. **B** shows a high magnification image from one of the membranes. The scale bar corresponds to 50 nm. **C** shows an FFT from the selected areas (red box in B). The ordered array is ~50 nm X 50 nm in size.

LPR8

A 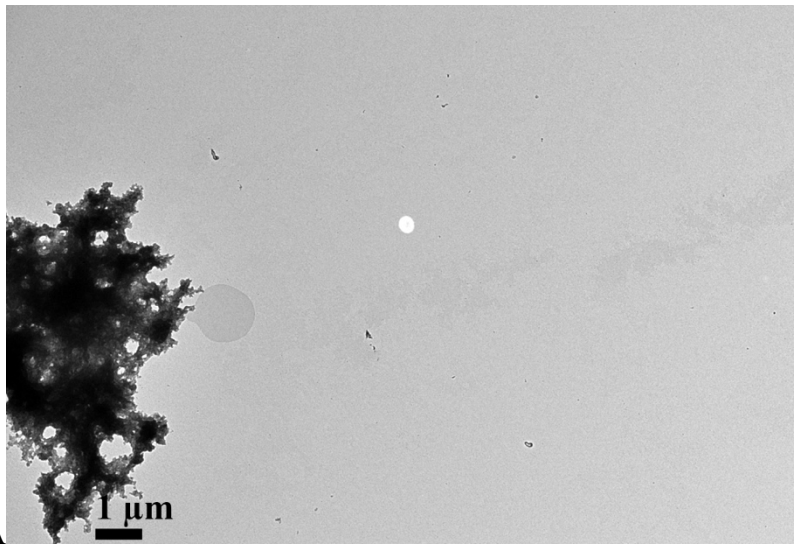

B 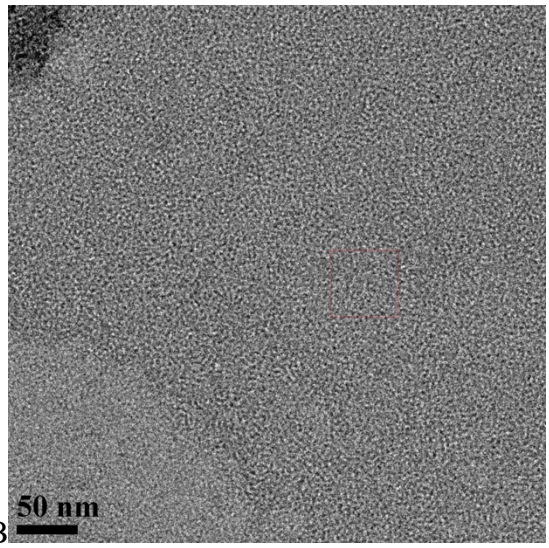

C 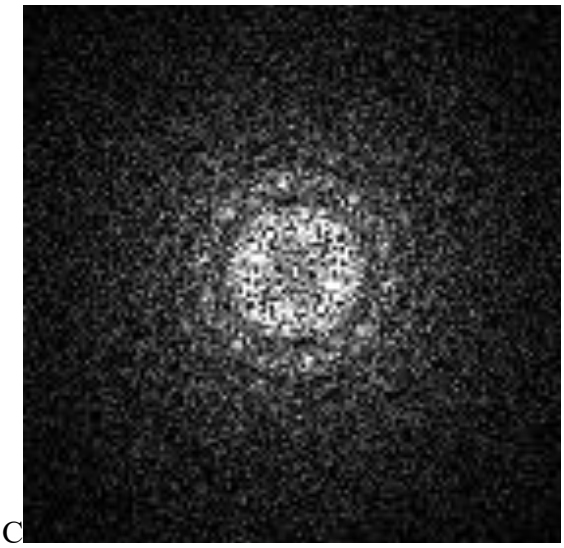

Figure 2.9. Representative micrographs from MCMJR1SPP LPR 2D crystallization trials. **(A)** shows an overview image of membrane size and morphology from the **LPR8** experiment. A vesicle next to an aggregate can be observed. The scale bar corresponds to 1 µm. **(B)** shows a high magnification image from the vesicle. The scale bar corresponds to 50 nm. **(C)** shows an FFT from the selected area (red box in B). The ordered array is ~50 nm X 50 nm in size.

LPR26

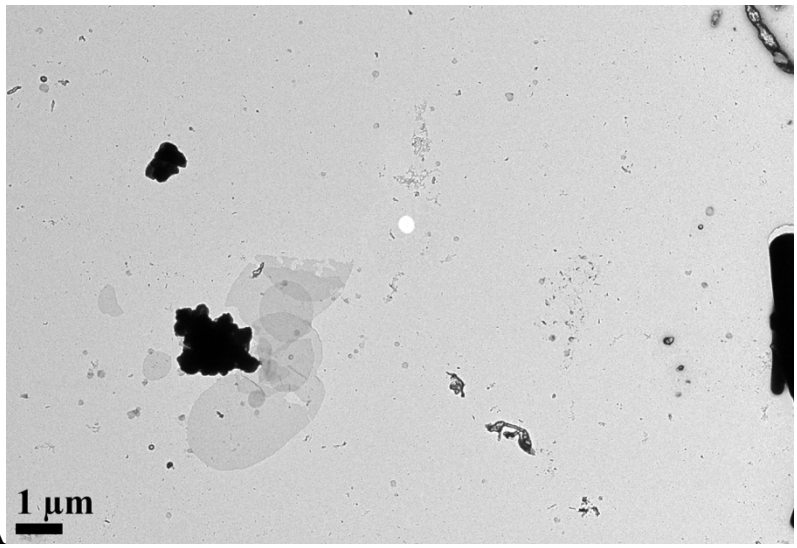

A

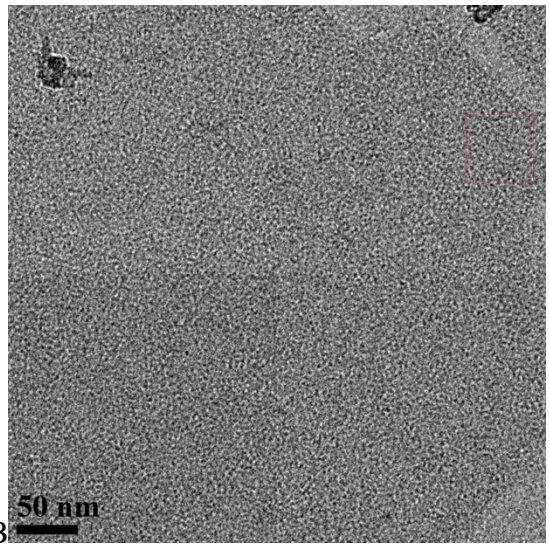

B

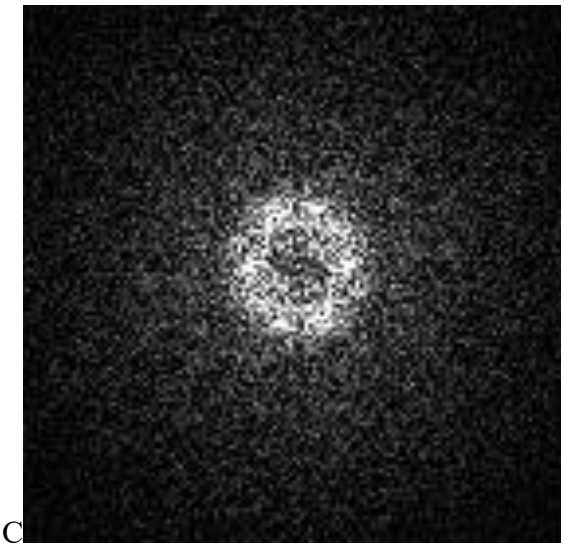

C

Figure 2.10. Representative micrographs from MCMJR1SPP LPR 2D crystallization trials. **(A)** shows an overview image of membrane size and morphology from the **LPR26** experiment. Several vesicles and sheetlike membranes can be observed. The scale bar corresponds to 1 µm. **(B)** shows a high magnification image from one of the membranes. The scale bar corresponds to 50 nm. **(C)** shows an FFT from the selected area (red box in B). The ordered array is ~50 nm X 50 nm in size.

pH PARAMETERS

pH 5.5

A 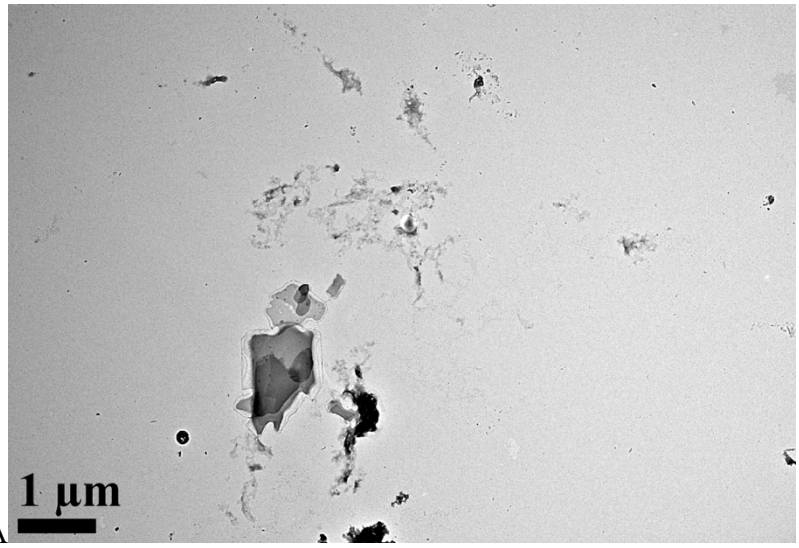

B 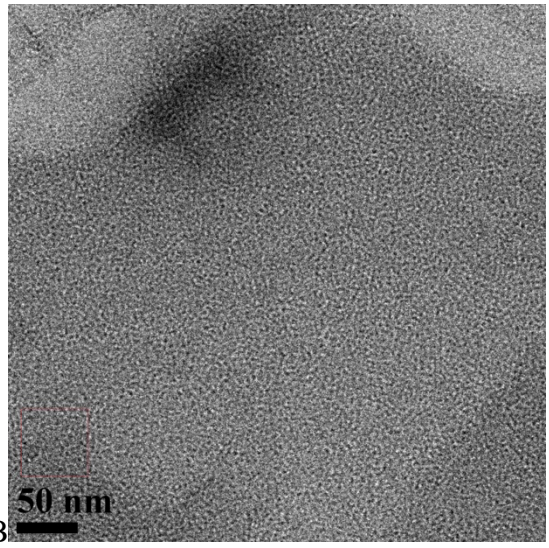

C 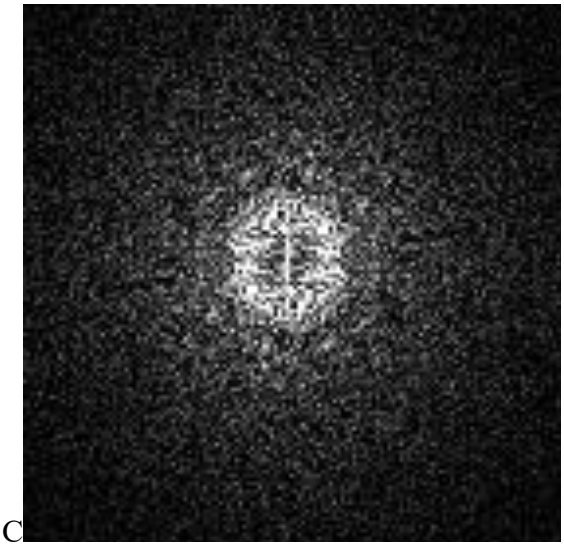

Figure 2.11. Representative micrographs from MCMJR1SPP pH 2D crystallization trials. **(A)** shows an overview image of membrane size and morphology from the **pH5.5** experiment. Sheetlike membranes can be observed. The scale bar corresponds to 1 µm. **(B)** shows a high magnification image from the membranes. The scale bar corresponds to 50 nm. **(C)** shows an FFT from the selected area (red box in B). There is a crystal that is about 50 nm X 50 nm in size.

pH 6

A 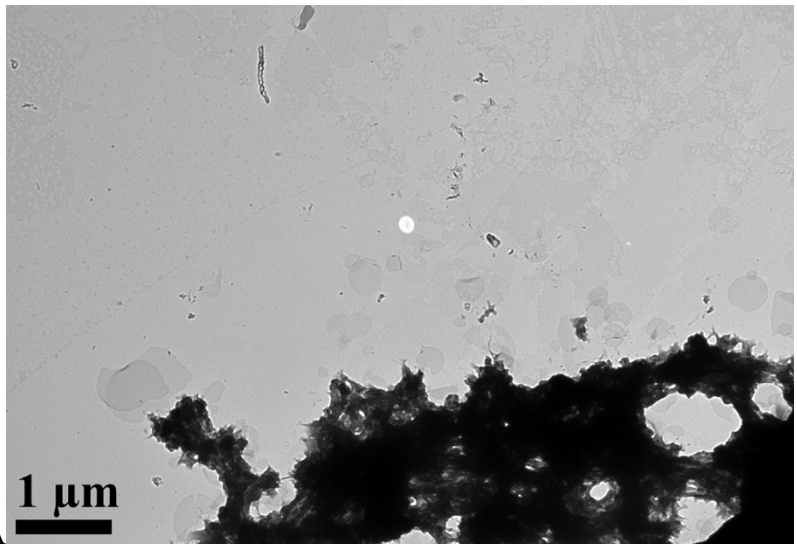

B 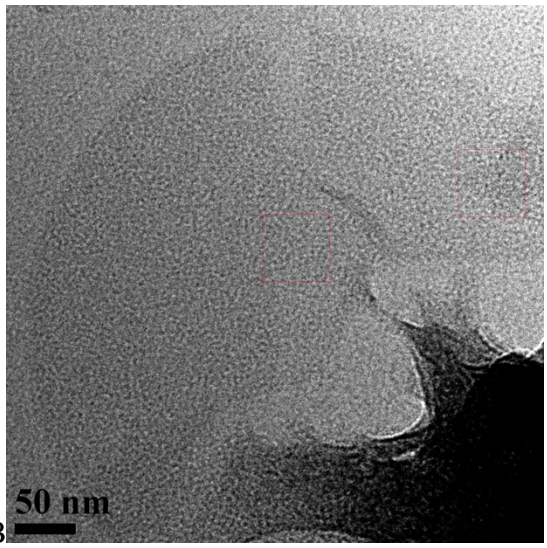

C 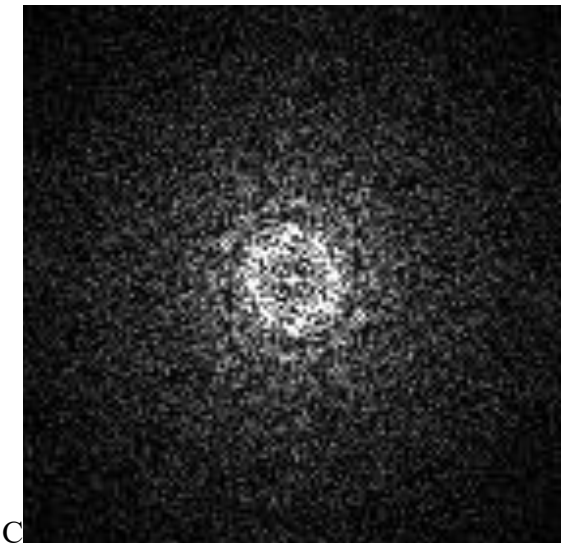

D 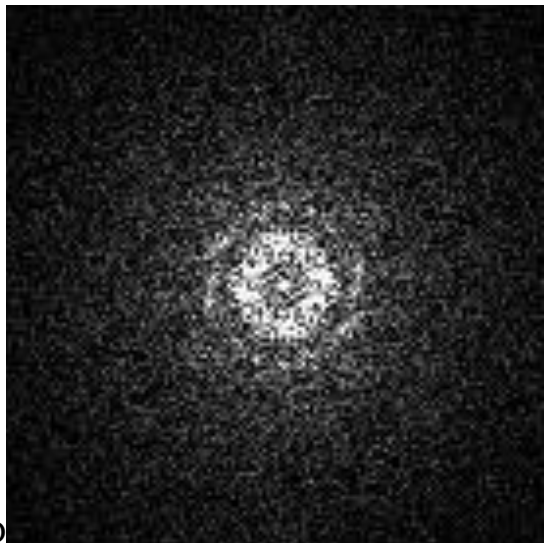

Figure 2.12. Representative micrographs from the MCMJR1SPP pH 2D crystallization trials. **(A)** shows an overview image of membrane sizes and morphologies from the **pH6** experiment. Several vesicles and sheetlike membranes can be observed. The scale bar corresponds to 1 μm. **(B)** shows a high magnification image from one of the vesicles. The scale bar corresponds to 50 nm. **(C and D)** show FFTs from the selected areas (red boxes in B). The ordered arrays are ~50 nm X 50 nm in size and have qualities of 3-5.

pH 8

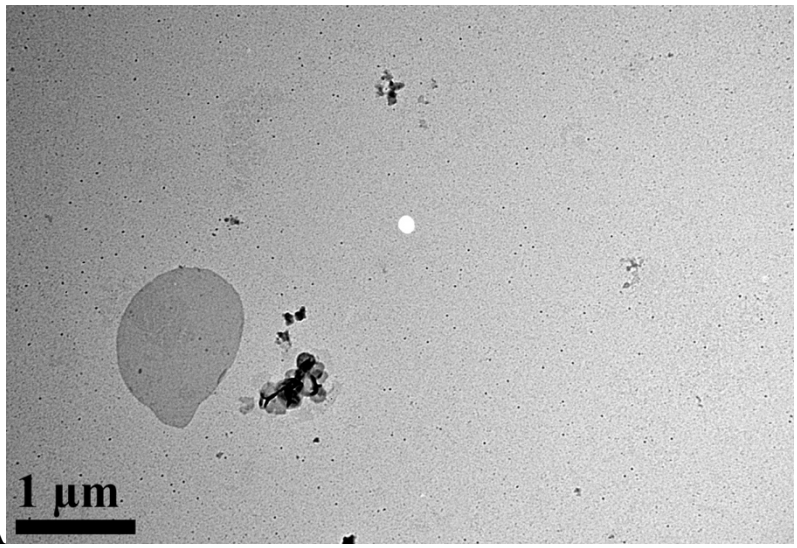

A

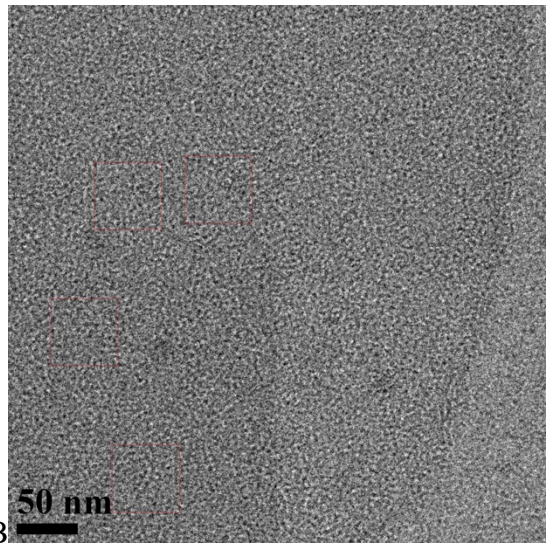

B

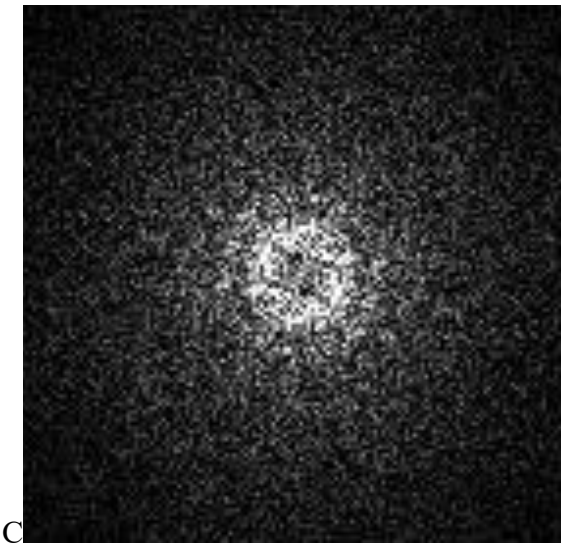

C

Figure 2.13. Representative micrographs from MCMJR1SPP pH 2D crystallization trials. **(A)** shows an overview image of membrane size and morphology from the **pH8** experiment. Several vesicles can be observed. The scale bar corresponds to 1 µm. **(B)** shows a high magnification image from one of the vesicles. The scale bar corresponds to 50 nm. **(C)** shows an FFT from the selected area (red box in B). The ordered arrays are ~50 nm X 50 nm in size.

TEMPERATURE PARAMETERS

21° C

A 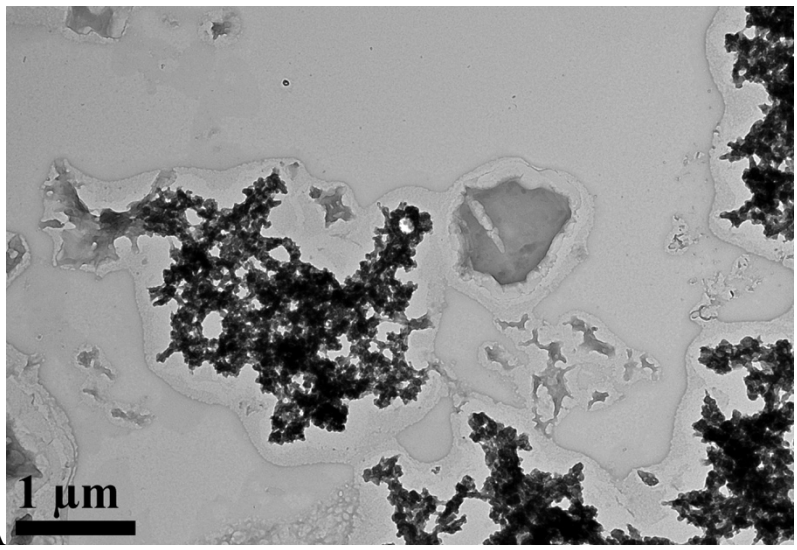

B 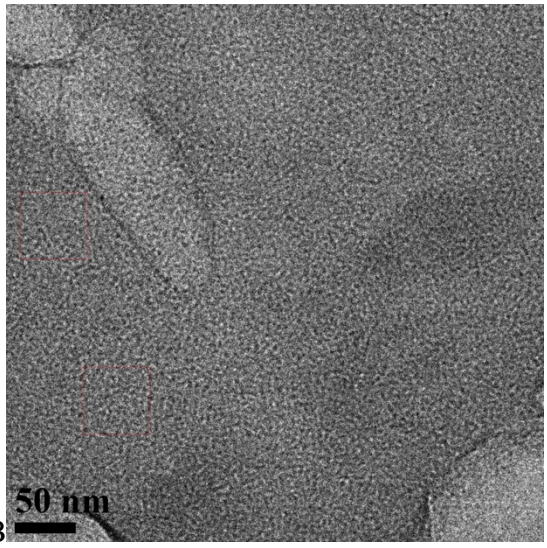

C 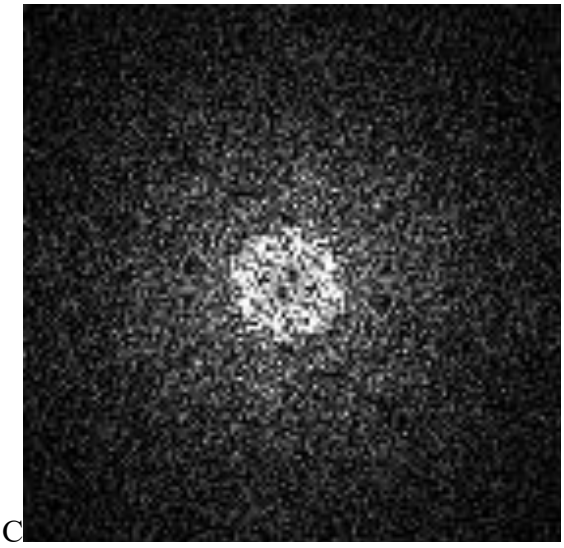

D 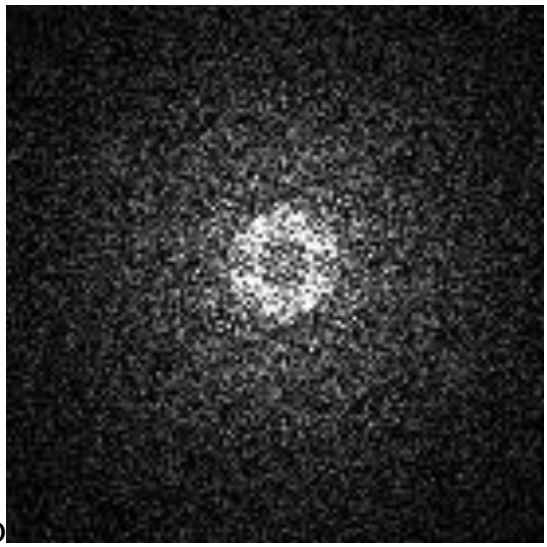

Figure 2.14. Representative micrographs from MCMJR1SPP temperature 2D crystallization trials. **(A)** shows an overview image of membrane size and morphology from the **21°C** experiment. Several sheetlike membranes can be observed. The scale bar corresponds to 1 μm. **(B)** shows a high magnification image from one the membranes. The scale bar corresponds to 50 nm. **(C and D)** show FFTs from the selected areas (red boxes in B). The ordered arrays are ~50 nm X 50 nm in size and have qualities of 1.

27°C

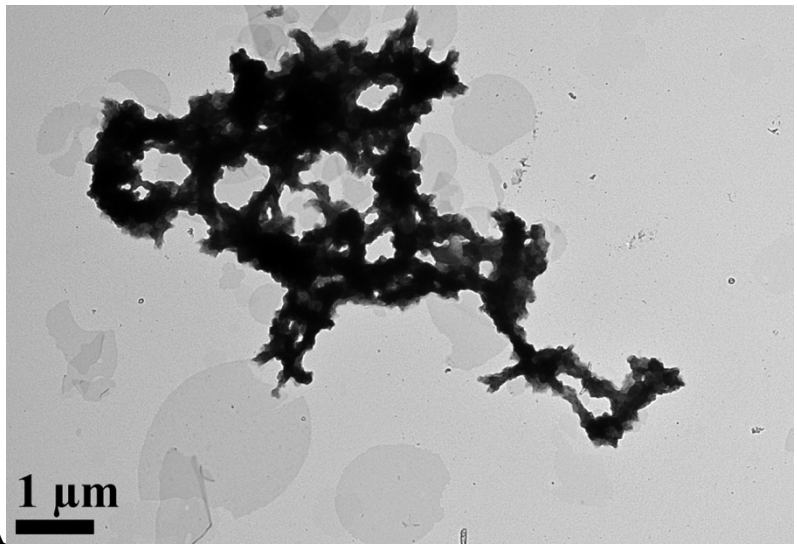

A

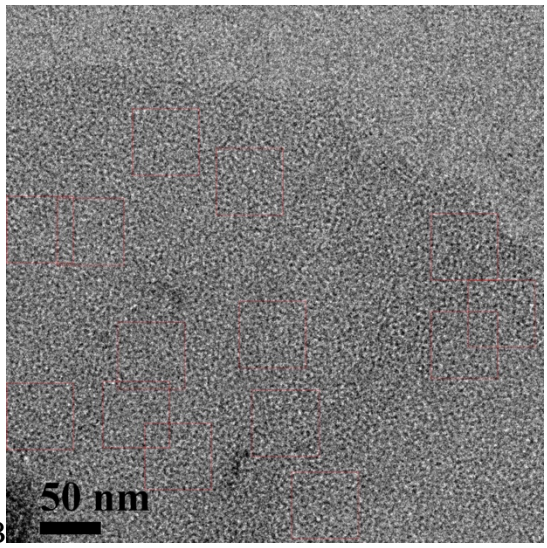

B

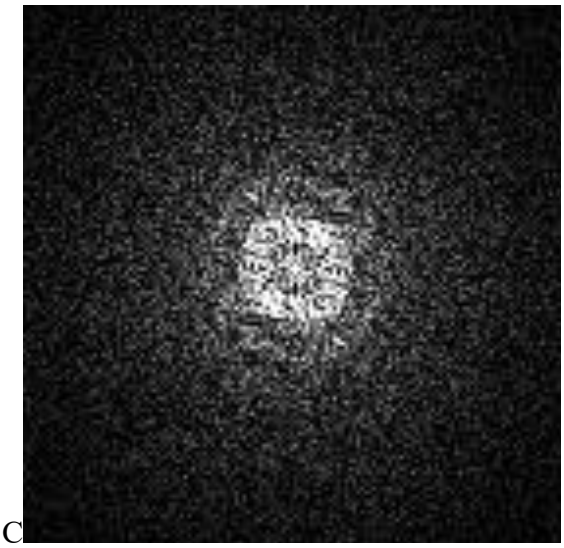

C

D 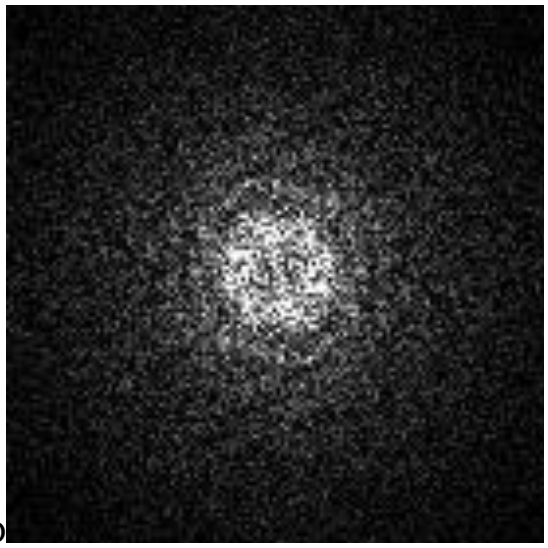

E 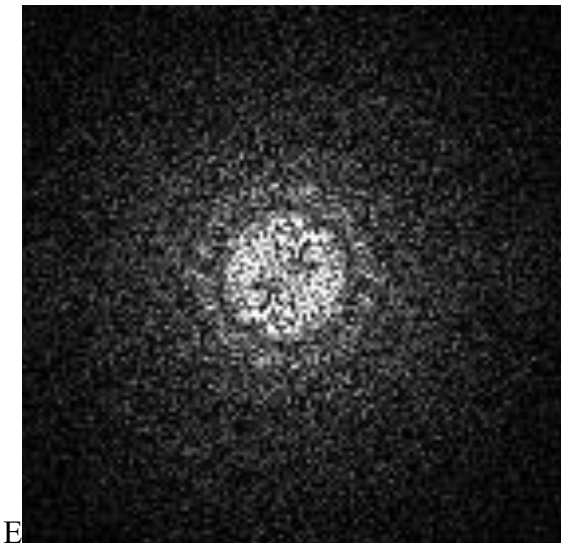

F 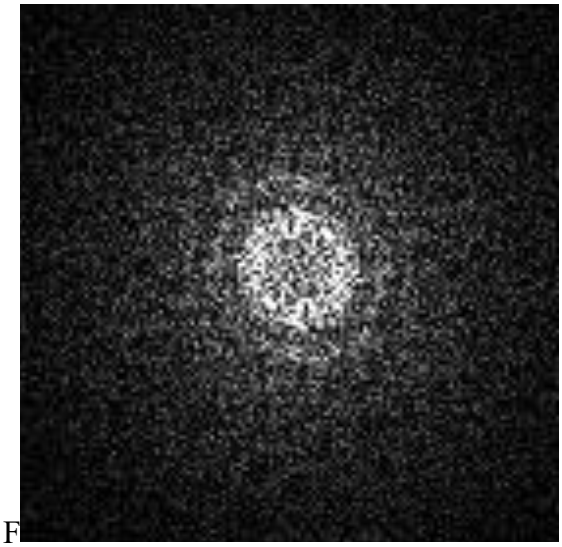

G 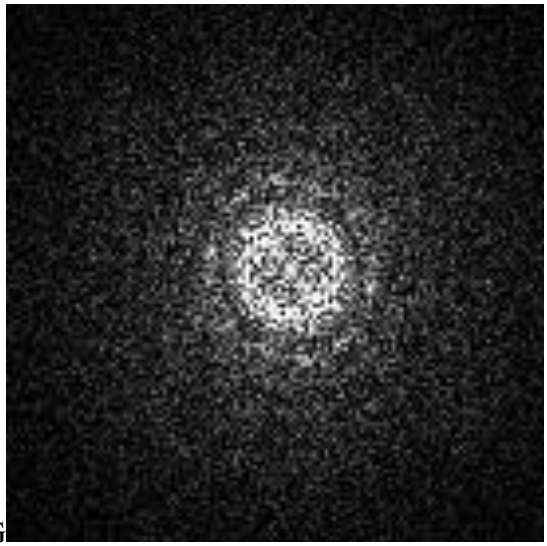

H 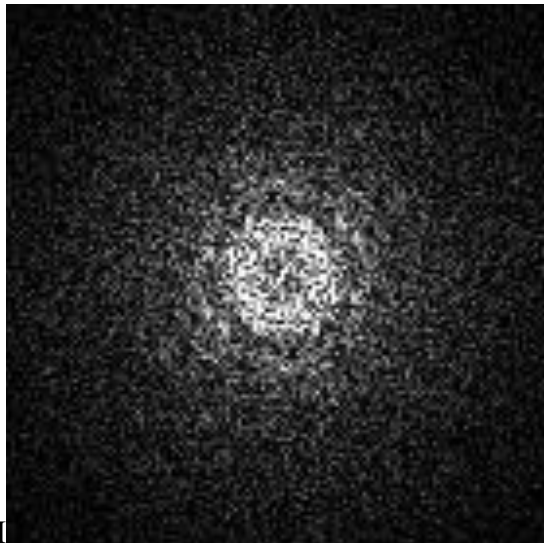

I 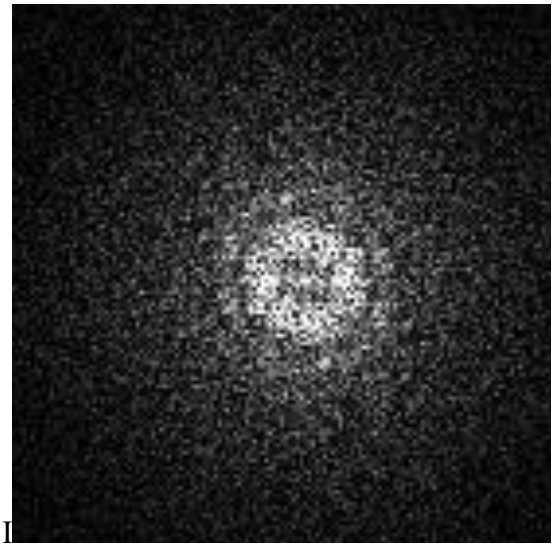

J 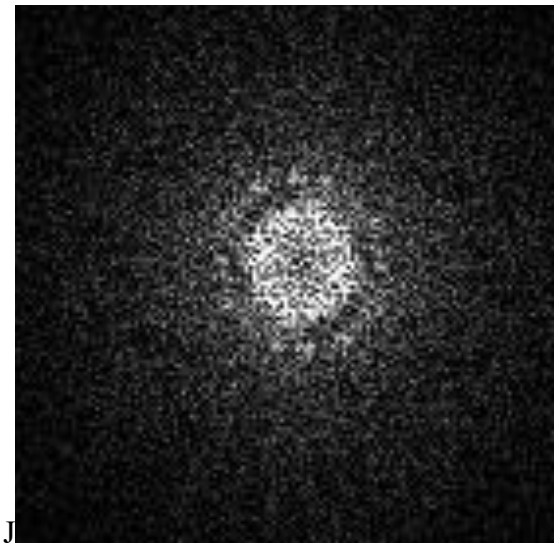

K 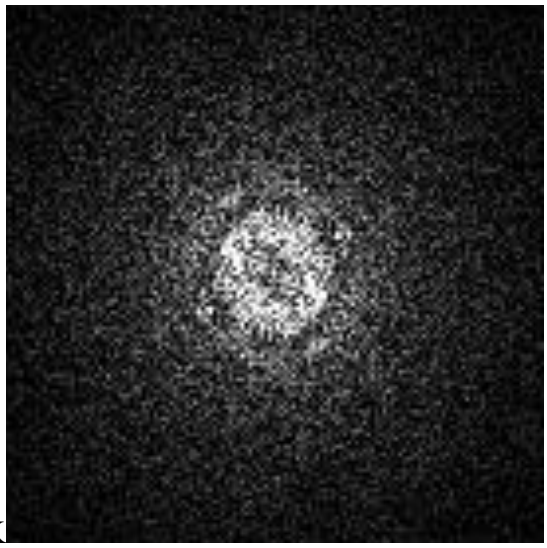

L 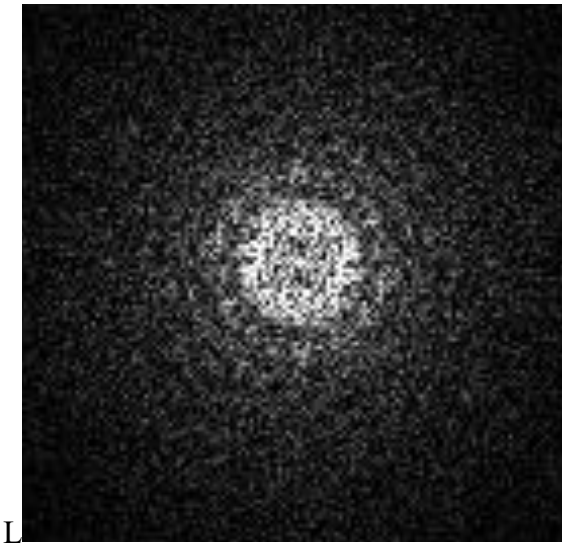

M 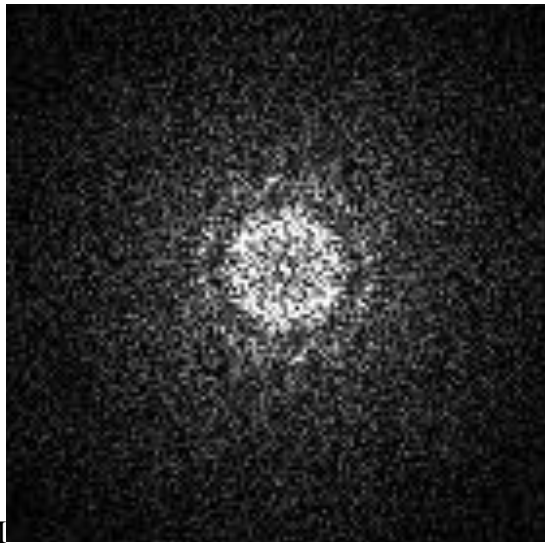

N 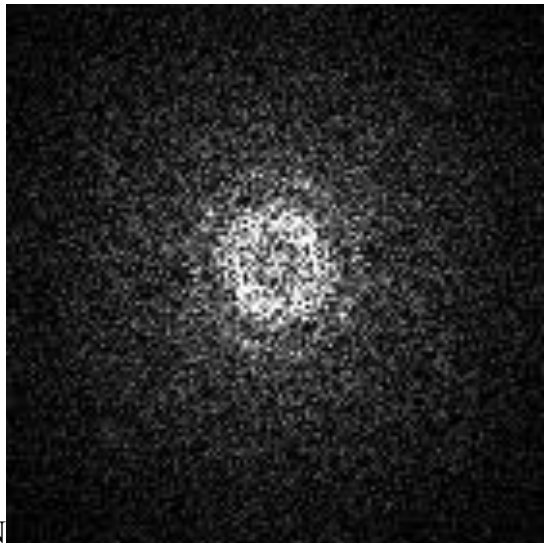

O 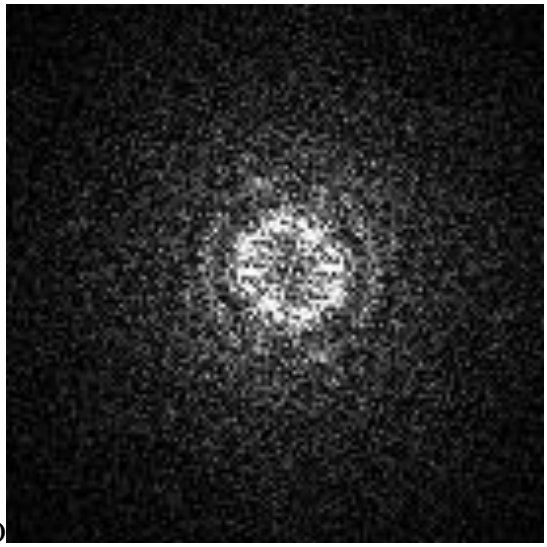

P 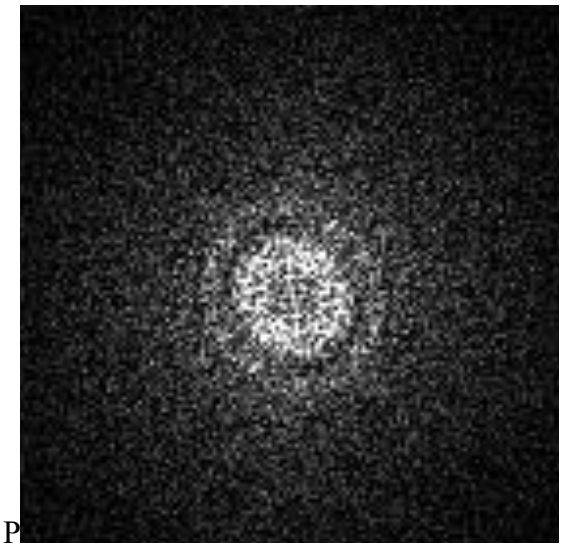

Figure 2.15. Representative micrographs from MCMJR1SPP temperature 2D crystallization trials. **(A)** shows an overview image of membrane size and morphology from the **27°C** experiment. Several vesicles and sheetlike membranes can be observed. The scale bar corresponds to 1 μm. **(B)** shows a high magnification image from one of the vesicles. The scale bar corresponds to 50 nm. **(C-P)** show FFTs from the selected areas (red boxes in B). There are many ordered arrays that are ~50 nm X 50 nm in size and have qualities of 2-5. Some ordered arrays are as big as 150 nm.

30°C

A 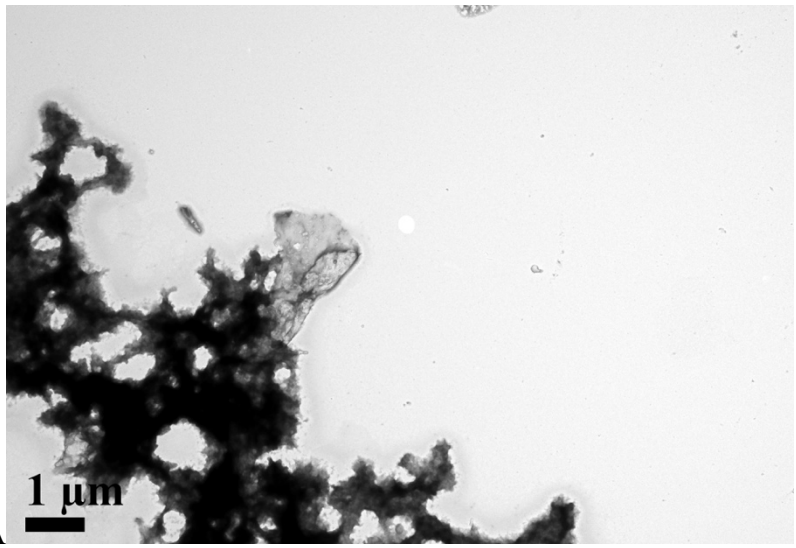

B 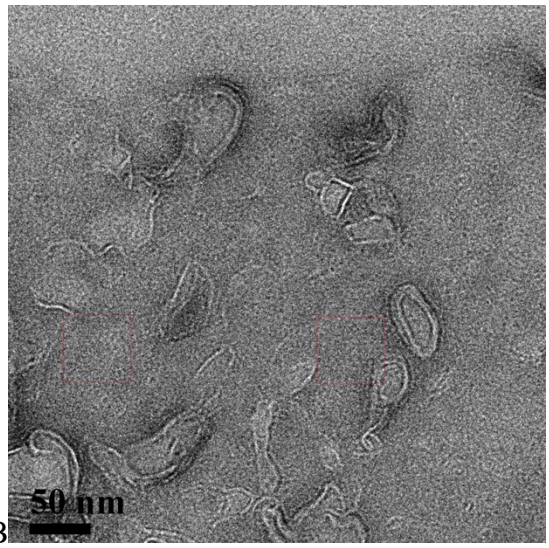

C 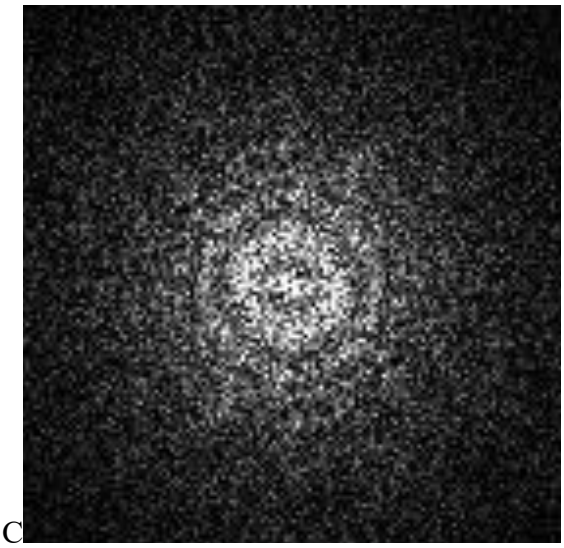

D 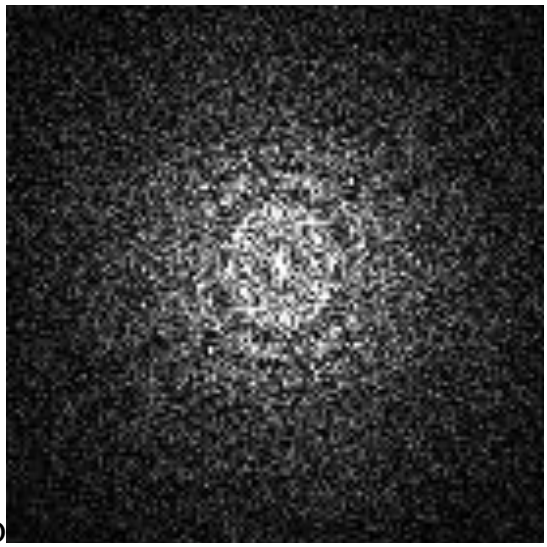

Figure 2.16. Representative micrographs from MCMJR1SPP temperature 2D crystallization trials. **(A)** shows an overview image of membrane size and morphology from the **30°C** experiment. A few membranes can be observed. The scale bar corresponds to 1 μm. **(B)** shows a high magnification image from one the membranes. The scale bar corresponds to 50 nm. **(C and D)** show FFTs from the selected areas (red boxes in B). Two ordered arrays are ~50 nm X 50 nm in size. The membranes have perforations.

GLYCEROL PARAMETERS

0% Glycerol

A 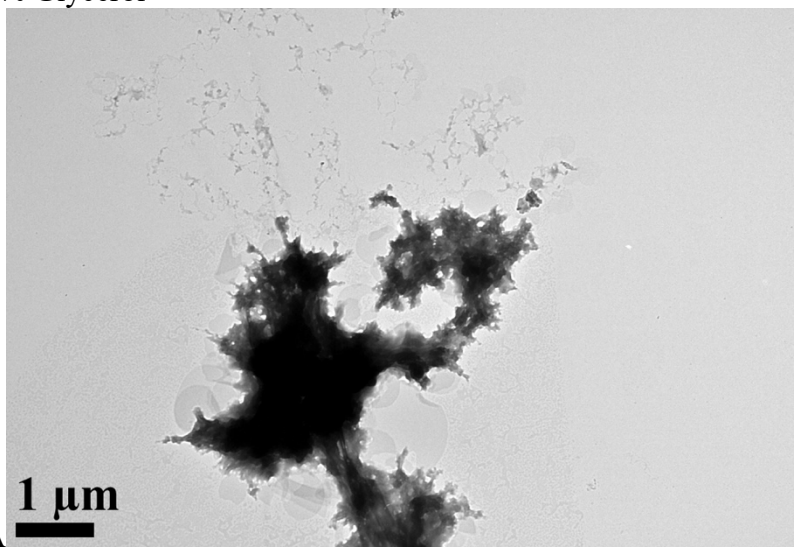

B 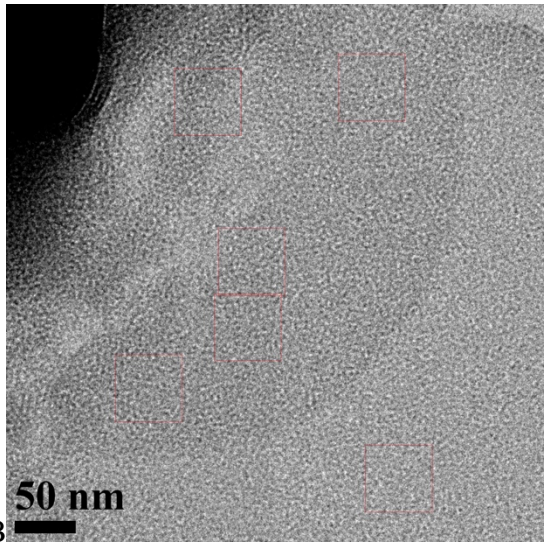

C 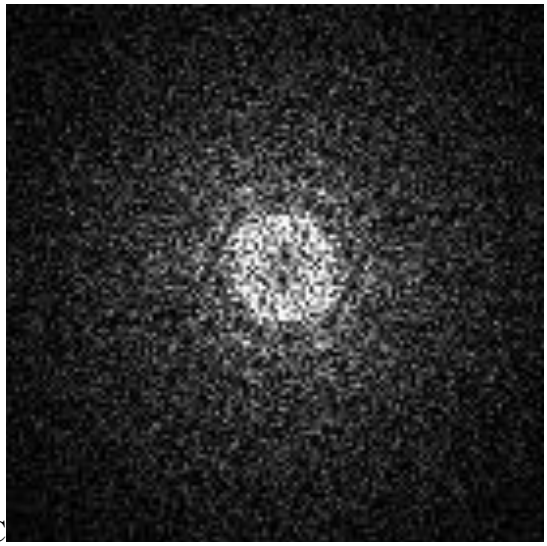

D 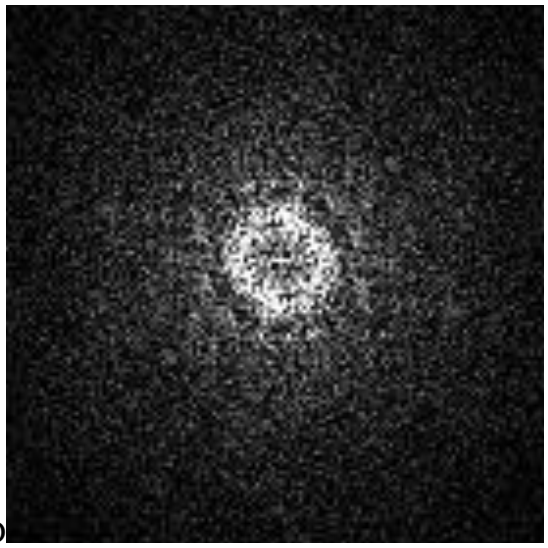 E 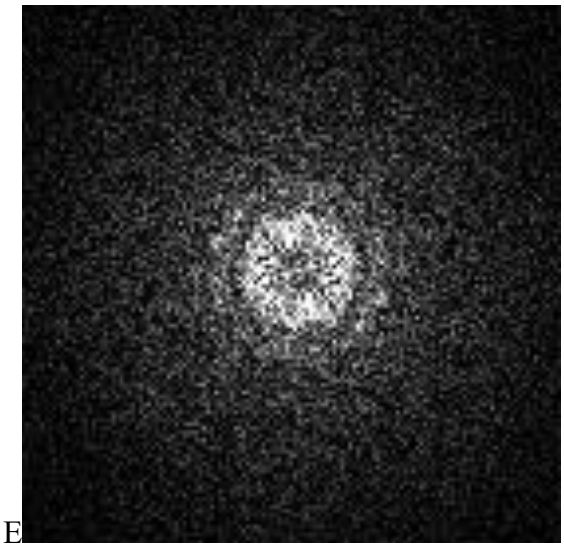

Figure 2.17. Representative micrographs from MCMJR1SPP glycerol 2D crystallization trials. **(A)** shows an overview image of membrane size and morphology from the **0% glycerol.** experiment. A few vesicles and sheetlike membranes can be observed. The scale bar corresponds to 1 μm. **(B)** shows a high magnification image from one the vesicles. The scale bar corresponds to 50 nm. **(C-E)** show FFTs from the selected areas (red boxes in B). Several ordered arrays are ~50 nm X 50 nm in size.

20% Glycerol

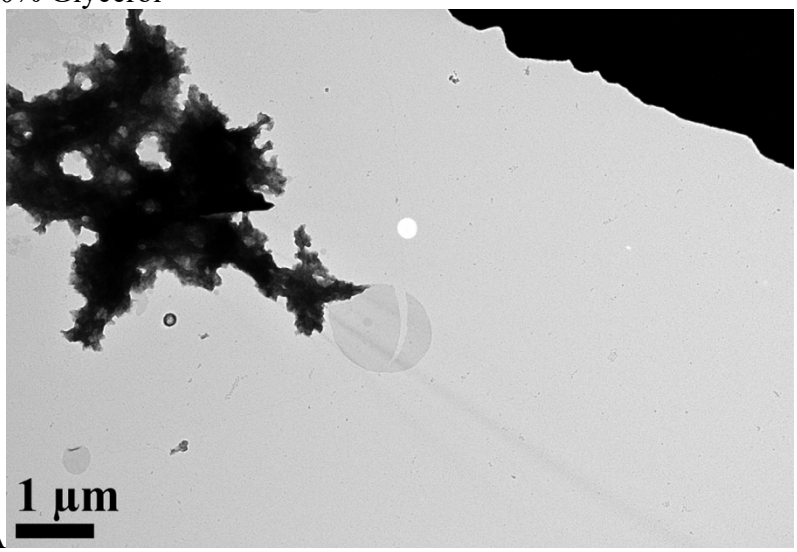

A

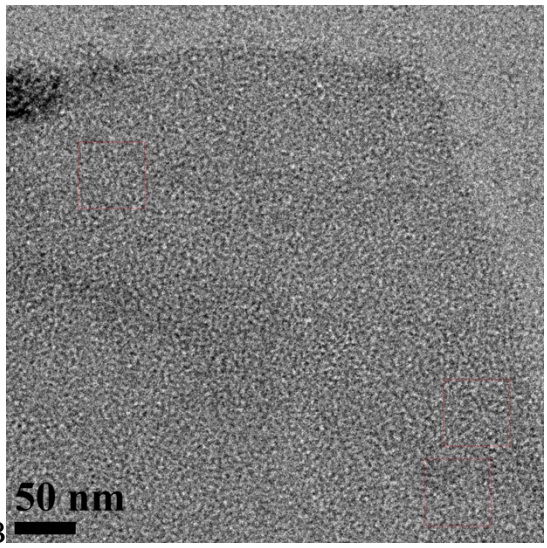

B

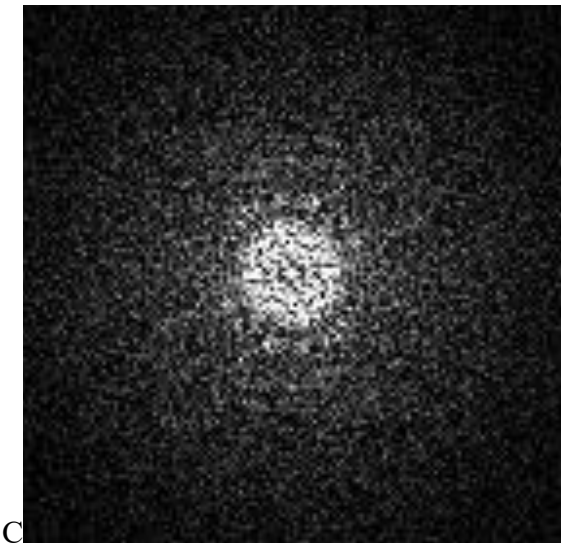

C

D 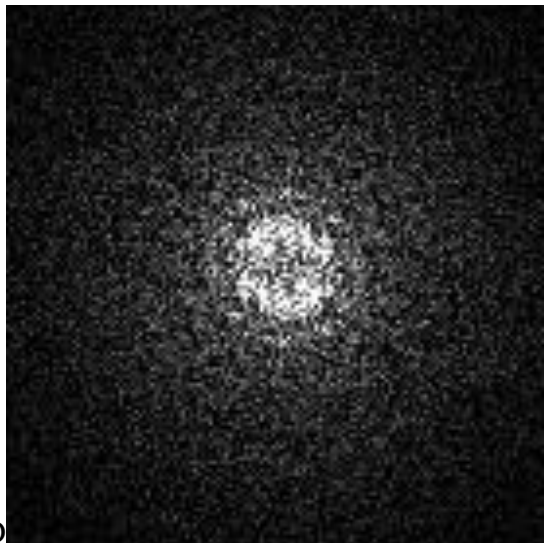 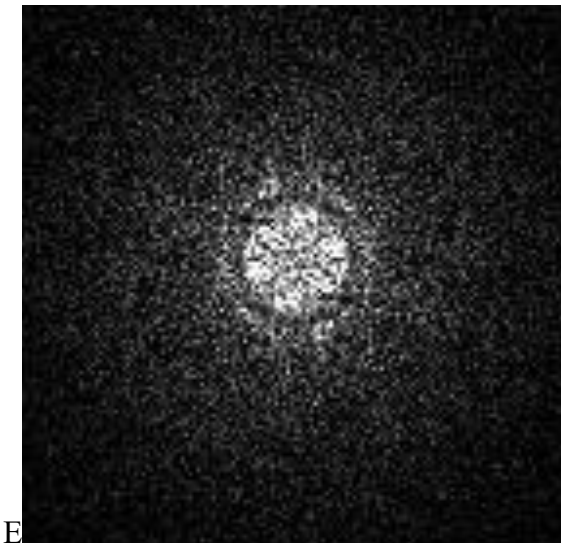 E

Figure 2.18. Representative micrographs from MCMJR1SPP glycerol 2D crystallization trials. **(A)** shows an overview image of membrane size and morphology from the **20% glycerol** experiment. A few vesicles can be observed. The scale bar corresponds to 1 μm. **(B)** shows a high magnification image from one the vesicles. The scale bar corresponds to 50 nm. **(C-E)** show FFTs from the selected areas (red boxes in B). Two ordered arrays are ~50 nm X 50 nm in size.

NaCl PARAMETERS

0mM

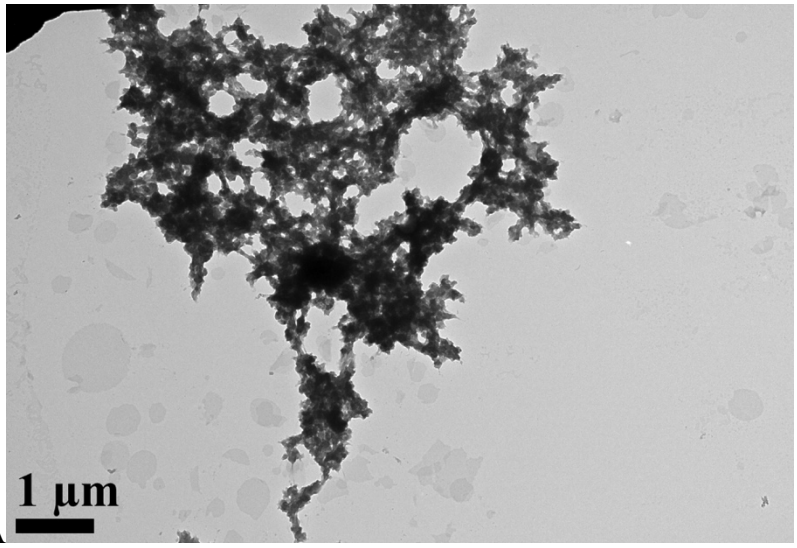

A

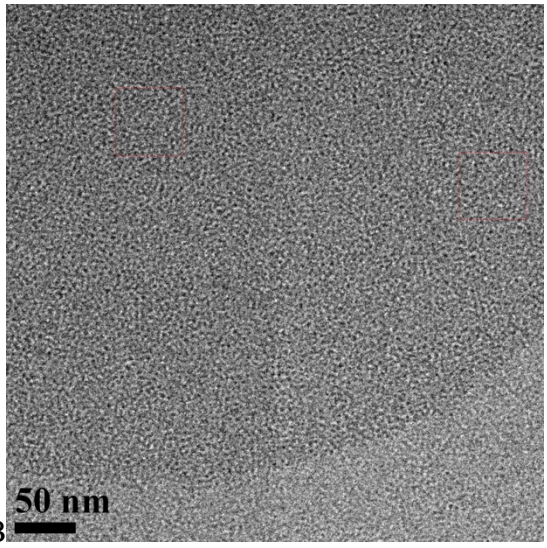

B

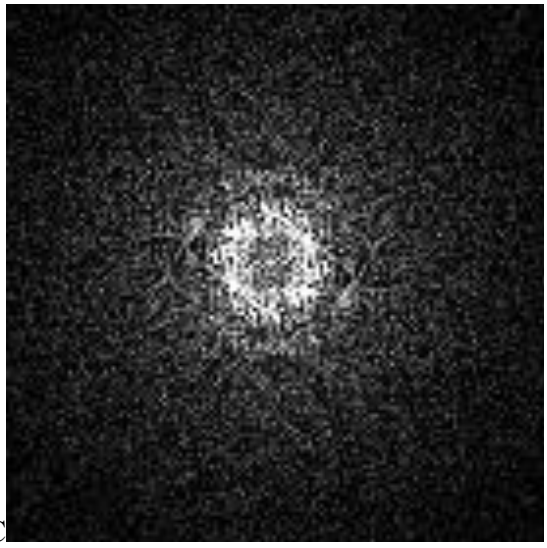

C

D 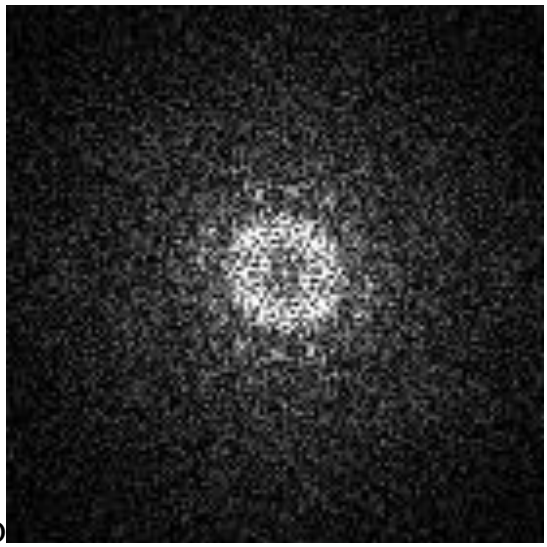

Figure 2.19. Representative micrographs from MCMJR1SPP NaCl 2D crystallization trials. **(A)** shows an overview image of membrane size and morphology from the **0mM NaCl** experiment. Several vesicles and sheetlike membranes can be observed. The scale bar corresponds to 1 μm. **(B)** shows a high magnification image from one the vesicles. The scale bar corresponds to 50 nm. **(C and D)** show FFTs from the selected areas (red boxes in B). Two ordered arrays are ~50 nm X 50 nm in size and have qualities of 2-5.

250mM

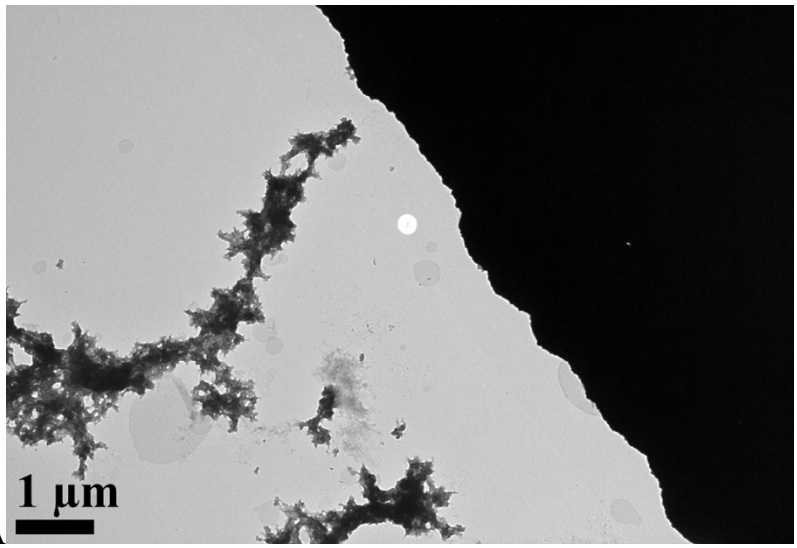

A

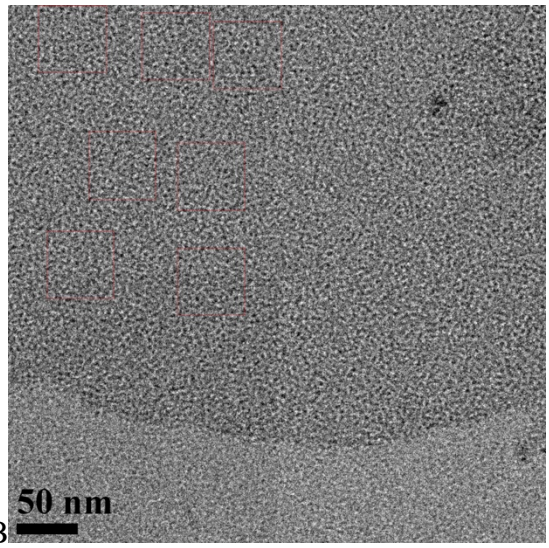

B

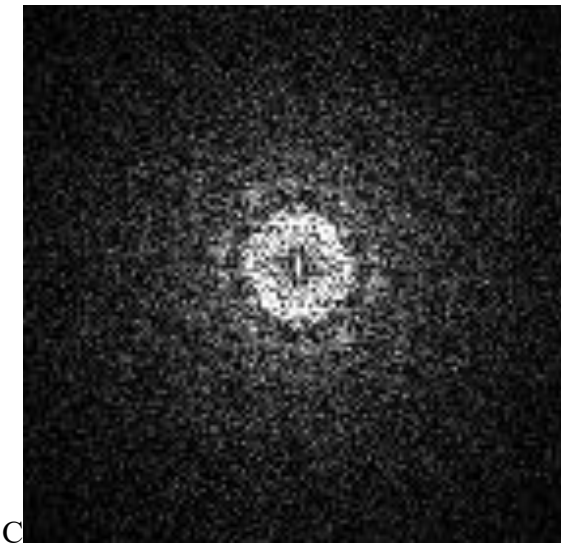

C

Figure 2.20. Representative micrographs from MCMJR1SPP NaCl 2D crystallization trials. **(A)** shows an overview image of membrane size and morphology from the **250mM NaCl** experiment. Several vesicles and sheetlike membranes can be observed. The scale bar corresponds to 1 µm. **(B)** shows a high magnification image from one the vesicles. The scale bar corresponds to 50 nm. **(C-I)** show FFTs from the selected areas (red boxes in B). The many ordered arrays are ~50 nm X 50 nm in size. Some crystals are as big as 150-200nm in size.

D 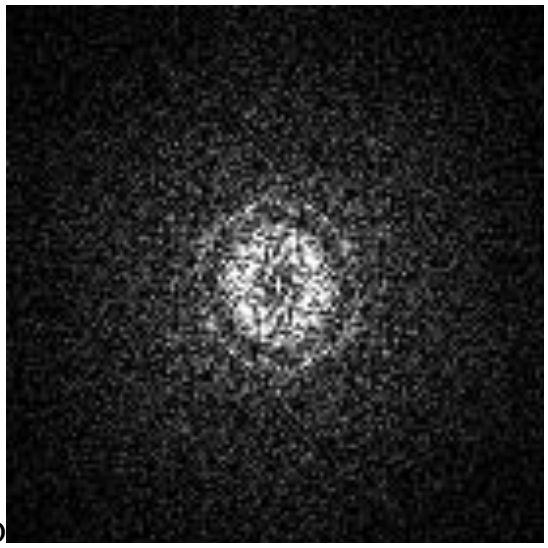

E 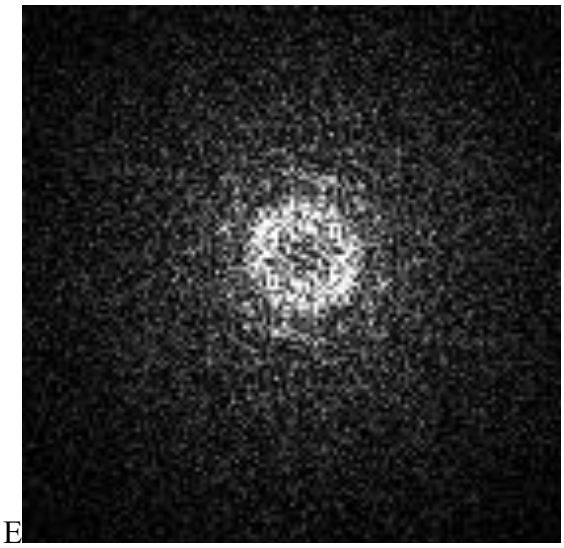

F 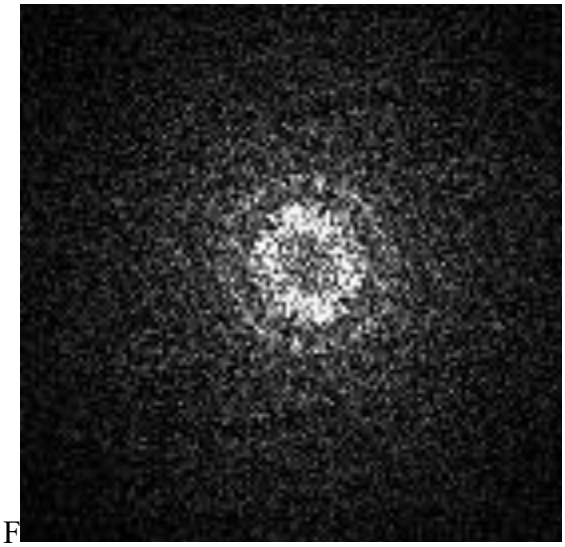

G 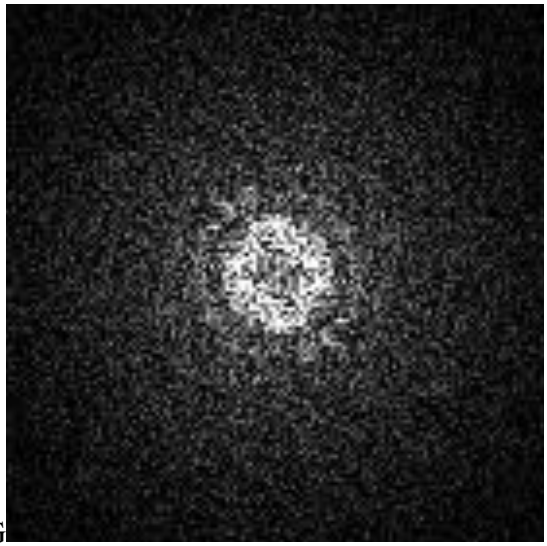

H 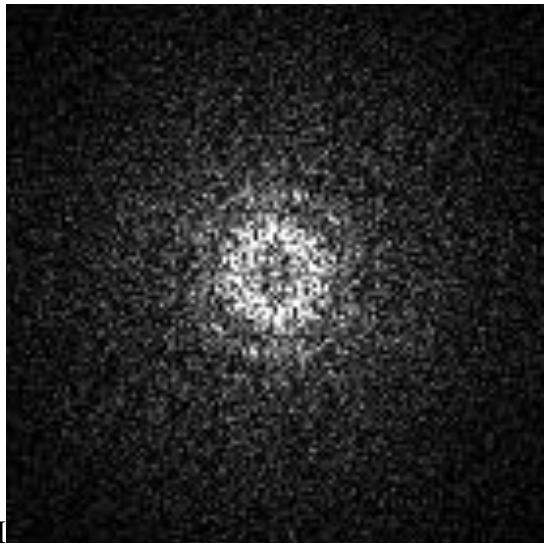

I 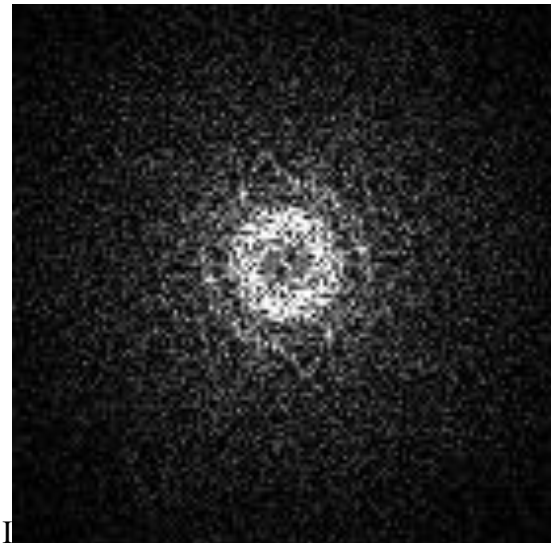

1M

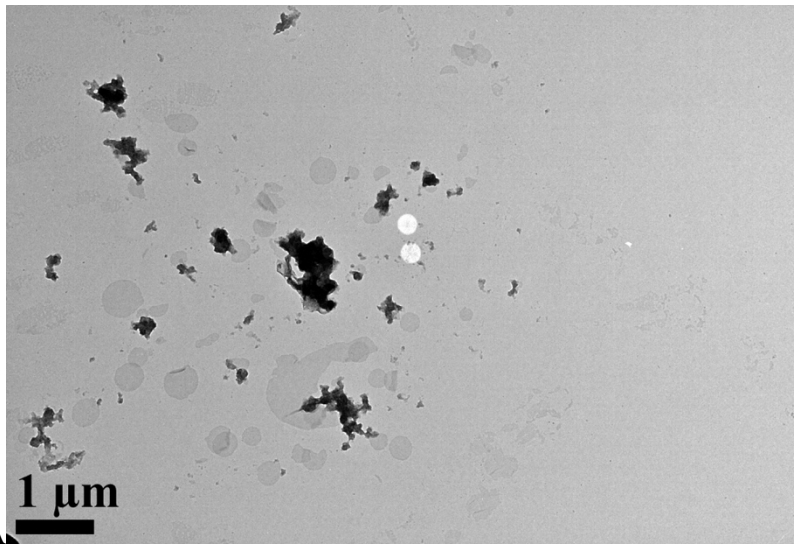

A

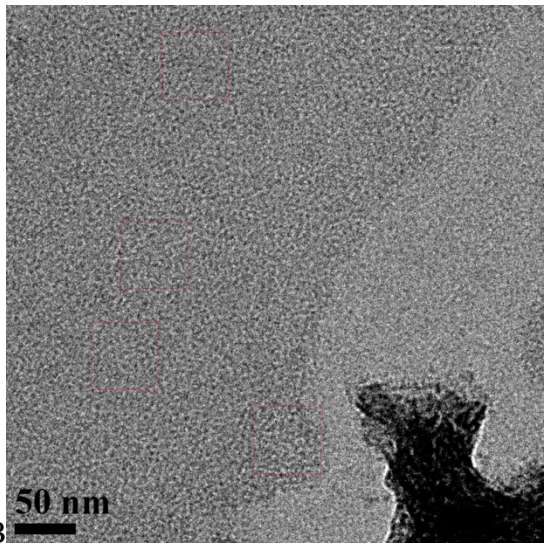

B

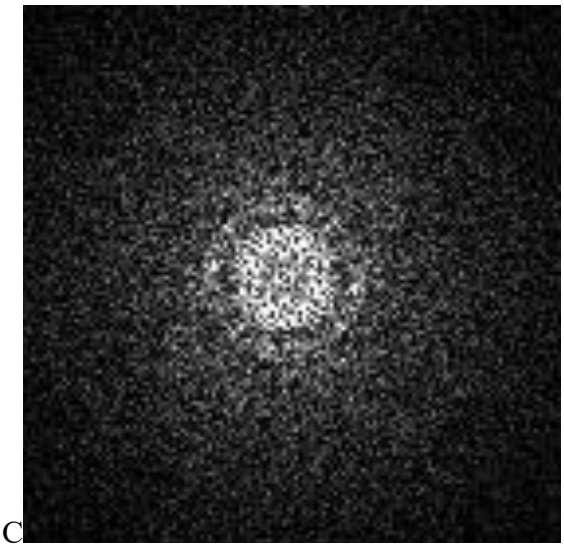

C

D 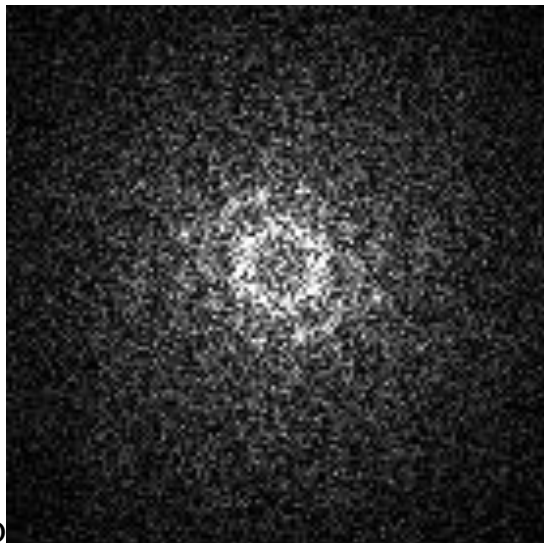 E 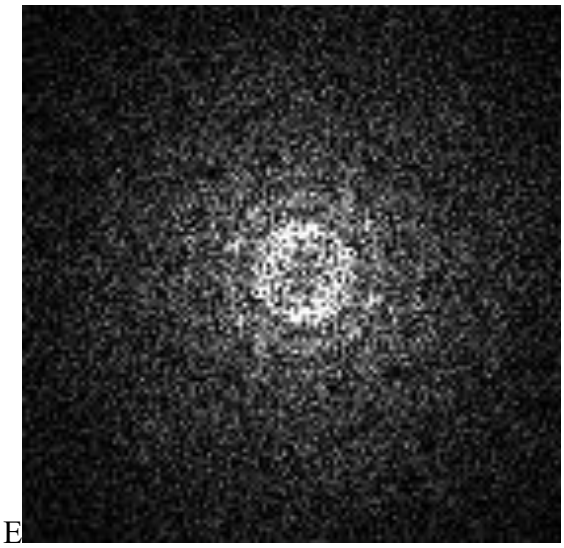

Figure 2.21. Representative micrographs from MCMJR1SPP NaCl 2D crystallization trials. **(A)** shows an overview image of membrane size and morphology from the **1M NaCl** experiment. Several different size vesicles can be observed. The scale bar corresponds to 1 μm. **(B)** shows a high magnification image from one the vesicles. The scale bar corresponds to 50 nm. **(C-E)** show FFTs from the selected areas (red boxes in B). A few ordered arrays are ~50 nm X 50 nm in size.

2.4 DISCUSSION

Several key parameters can affect two-dimensional crystallization of membrane proteins. One of the most important parameters is the lipid-to-protein-ratio (LPR) [12, 31]. For successful two-dimensional crystallization, the optimal mixture of protein and lipid has to be identified. Excessively low lipid concentrations lead to protein aggregation, while excessively high lipid concentrations allow for reconstitution but often not for 2D crystallization. A wide range of LPRs (0-26) was tested[127]. where the optimal LPR was found to fluctuate between purifications. This observation is not uncommon because the amount of copurified lipid can vary between purifications.

In order to reduce the amount of copurified lipid, our collaborators Drs. Sibel Kalyoncu and Swe-Htet Naing from Dr. Lieberman's laboratory, applied an extra wash step during SPP purification. Furthermore, fractions (10-13) were kept separate instead of being combined/pooled and concentrated. A wide range of LPRs (0-26) was tested for each fraction. The use of specific fractions from each purification allowed for the identification of a specific LPR for specific fractions, which could be reproduced between purification experiments: LPR 8 from fractions 11 and 12 gave the best results (***Figure 2.9***) in terms of membrane size and ordered arrays. The 2D crystals under these conditions had qualities of 4 and 5 (1-5 scale). These findings were highly reproducible and allowed for significantly more efficient and reliable investigation of other crystallization parameters.

Another 2D crystallization parameter tested was the pH. The overall charge and conformational state of proteins are greatly influenced by this parameter. We tested a range of pH values (pH 5-8) to study the effect of the pH on SPP crystallization. We found the best results

occurred at pH 6 and pH 6.5 (***Figure 2.12***). Results under these conditions gave crystal qualities of 3-5.

Temperature is another critical two-dimensional crystallization parameter as it influences the membrane fluidity and timeframe for reconstitution[31]. When testing for optimal temperature, it is recommended to examine temperatures near or above the lipid phase transition temperature[31]. DMPC was used for the SPP crystallization trials[127]. A range of temperatures between 21-30°C were tested. Temperatures below 24°C resulted in small crystals that had poor quality, which is just above the phase transition for DMPC. For temperatures around 30°C, perforations in the membranes were observed (***Figure 2.16 B***). These perforations in the membrane prevent the growth of large 2D crystals. The best results were observed between24-27°C. Compared to the other temperatures tested, the crystal quality was better (crystal qualities 3-5) and a large number of areas had ordered arrays.

Next, different components of the detergent-free dialysis buffer were tested and optimized. The first parameter tested was the concentration of glycerol. Glycerol has been shown to increase the crystal size for several membrane proteins[128, 129]. A concentration of 20% glycerol was initially used due to the success for other membrane proteins[128]. We tested buffers with different concentrations of glycerol (0-20%). Our results showed fewer and smaller membranes in 0-5% glycerol compared to 10-20%. Thus, the use of 20% glycerol was continued.

Next, the NaCl concentration was tested. The salt concentration can affect the membrane size and even cause stacking[31]. A wide range of NaCl concentrations (0-1M) were tested. We did not see a significant improvement in the quality of the crystals; however, we did see an increase in the number of areas with ordered arrays (shown by an increased number of red boxes in the high magnification images). NaCl concentrations between 200mM-250mM gave the best

results (***Figure 2.20***). The crystal quality and number of areas with ordered arrays were higher than for any other concentrations. Higher concentrations (1M) also resulted in ordered arrays but the number of ordered arrays and relative abundance were not as high as at 200-300mM NaCl (***Figure 2.21***). This is a significant improvement since optimization of other 2D crystallization conditions may lead to the merging of these small ordered arrays (50nm x 50nm) into large, continuous 2D crystal arrays to be used for high resolution data collection and structure determination.

While we have made substantial progress in improving the crystal size and quality by optimizing various parameters, the order and size of continuous arrays need to be improved before the structure of SPP can be determined. Different approaches and various parameters that can help improve the crystal size and quality are discussed in chapter 5. Ultimately, the goal is to obtain well-ordered 2D crystals that are approximately one micron in size in order to determine the cryo-EM structure of SPP within a phospholipid bilayer.

2.5 ACKNOWLEDGEMENTS

I would like to thank Dr. Raquel Lieberman and her laboratory for their collaboration with the MCMJR1SPP project. Drs. Sibel Kalyoncu and Swe-Htet Naing have provided me with samples for the 2D crystallization experiments. I want to thank Dr. Lieberman for her support and feedbacks on my experiments.

I want to thank Maureen Metcalfe, my predecessor on this project. She has mentored me when I was taking over the project and has always been willing to help. I want to thank my Ph.D. Advisor Dr. Schmidt-Krey for her guidance and encouragements. She taught me how to use the electron microscope and has always given me constructive feedback on my experiments.

CHAPTER 3: CRYO-EM: SINGLE PARTICLE ANALYSIS OF ACTIVE PSII

3.1 INTRODUCTION

Plants, cyanobacteria, and algae conduct photosynthesis. During photosynthesis, water and carbon dioxide molecules are converted into glucose and other organic molecules[130]. This process takes place via photosystem I and Photosystem II. Photosystem II (PSII) is a multisubunit membrane protein complex located in the thylakoid membrane of chloroplasts. PSII contains approximately 20 subunits as well as chlorophyll molecules, cofactors, and a Mn4CaO5 cluster that are required for the proper functioning of PSII[131]. PSII is constituted of a core complex which is comprised of intrinsic subunits and surrounded by various light harvesting complex subunits. The core PSII complex is conserved across all photosynthetic organisms while the light harvesting subunits have variations across species[132]. Furthermore, the core is conserved in all photosynthetic organisms from unicellular cyanobacteria to multicellular organism like plants. The degree of core complex conservation across all photosynthetic organisms shows how important it is for optimal function.

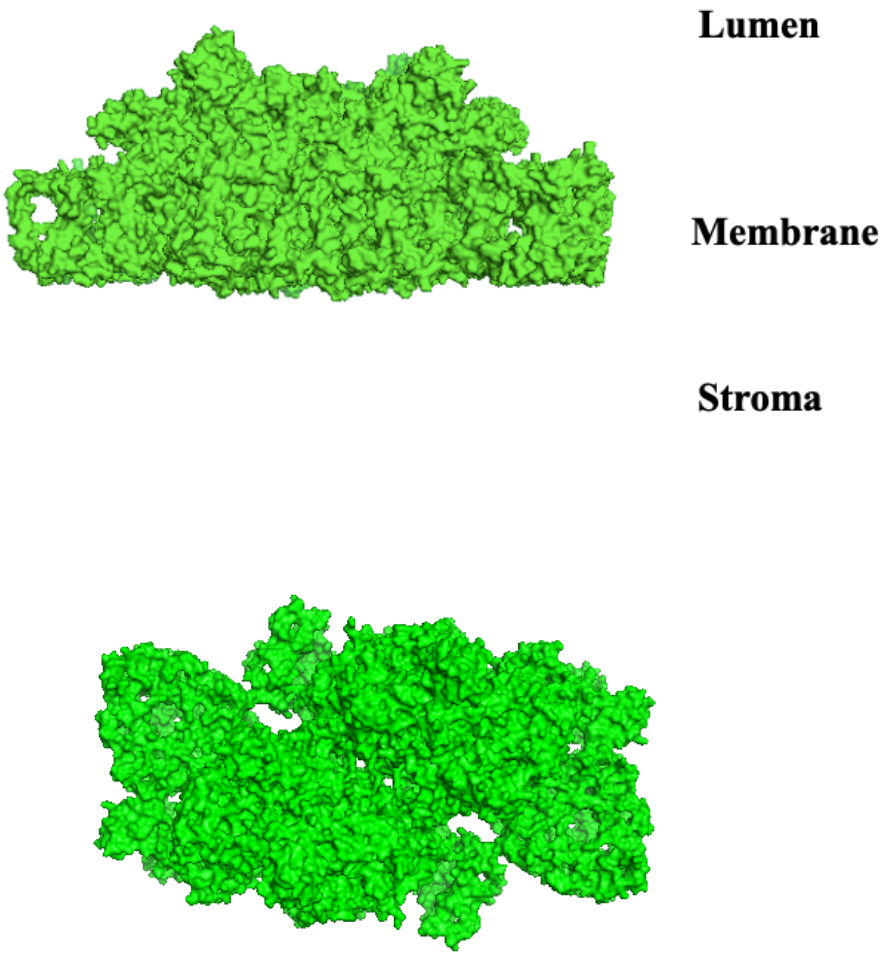

Figure 3.1. Structure of spinach PSII (PDB ID: 3JCU). Side view **(A)** and top view **(B)** of the overall structure is shown. These figures show the overall architecture of PSII. When viewed from the side (parallel to the plane of the membrane, shown in A), PSII resembles a crown. PSII has a rectangular shape when viewed perpendicular to the plane of the membrane.

Several structures of PSII have been solved to date [133-142]. These structures are from different organisms such as algae, cyanobacteria, spinach, and peas and allow for the comparison across a wide range of species. However, these structures are of inactive PSII or PSII with substantially reduced activity. These problem of solving a structure of active PSII is associated with the difficulties to purify membrane proteins and especially when the membrane protein is a

complex. PSII tends to lose up to several of its subunits during purification[143, 144]. This results in PSII preparations with reduced activity or lost activity[135]. The structures solved from these protein preparations may not represent the active PSII but have still provided important insights into the overall architecture and detailed visualization of the complex[135, 141].

In order to obtain structural information of active PSII, the complex was purified from market spinach (*Spinacea oleracea*) with gentle purification that allows PSII to retain its activity[145]. While this purification allows PSII to retain its function, it comes with a cost. The purified sample is heterogeneous. There are differently-sized PSII complexes present in the resulting purification. The single particle cryo-EM approach allows for selection of specific sizes of PSII complexes in order to generate a 3D reconstruction using only the selected PSII complexes. This is done during image processing of the cryo-EM data.

3.2 PSII EXPERIMENTAL PROCEDURES

3.2.1 PURIFICATION OF ACTIVE PSII

PSII samples were purified from market spinach (*Spinacea oleracea*) leaves. The leaves were ground in a blender and grind buffer (50 mM HEPES-NaOH, 400 mM NaCl, 2mM $MgCl_2.6H2O$, 1 mM EGTA, 2 mg/mL BSA, pH 7.5) was used to break the cells and suspend them. Cheesecloth was used to filter the slurry and remove large plant matter and centrifuged to remove contaminants. The pellet was solubilized with Triton X-100. This sample is named the BBY PSII sample[145]. The BBY sample was then washed with SMN buffer (400 mM sucrose, 50 mM MES-NaOH, 15 mM NaCl, pH 6) a few times and solubilized using octyl β-D-thioglucopyranoside (OTG). This sample is named the OTG-PSII sample[146]. The OTG-PSII sample was centrifuged at 50,000*g for 15 minutes at 4°C. The supernatant was discarded, and the pellet was resuspended in OPDM buffer (0.3% β-DDM, 50 mM MES-NaOH, 10 mM NaCl, 20% sucrose, pH 6).

My collaborator Dr. Yusuf Uddin performed SDS-PAGE, UV-vis absorption spectroscopy, the oxygen evolution assay and mass spectrometry to characterize the biochemistry of PSII[147] The results show PSII retains full activity under the purification conditions outlined above and used for these studies (unpublished data)[147].

3.2.2 CRYO-EM GRID PREPARATION OF ACTIVE PSII

Cryo-EM grid preparation was performed in a dark room equipped with green light. Quantifoil 2-2 grids or C-flat EM grids were used for cryo-EM grid preparation. A thin layer of carbon was used to make cryo-wells for the C-flat grids. The C-flat grids with cryo-wells were baked overnight at 50°C. The grids were glow-discharged at 15 mM for 15 seconds in an Argon

gas environment. In a dark room, 3 μL of the active PSII sample was applied to the grid. Then the sample was placed inside a Vitrobot[72] at 100% humidity and 4°C. Blot times of 4-6s in 0.5s increments were tested, and the grids were plunge-frozen inside liquid ethane. The PSII cryo-EM grids were stored in a liquid nitrogen dewar until data collection.

3.2.3 CRYO-EM DATA COLLECTION AND IMAGE PROCESSING OF ACTIVE PSII

Cryo-EM data was collected with a Titan Krios cryo-EM, equipped with DE-64 and Gatan K3 direct electron detectors, via NIH U24 Consortium access at Florida State University. Leginon software was used for automatic data collection[44]. Each image was evaluated using Appion[148]. After frame alignment and CTF estimation, particles were manually picked from each micrograph using RELION software[49]. Particle stacks were created and imported from Florida State University High Performance Computing (HPC) to Georgia Institute of Technology Partnership for Advance Computing Environment (PACE). cisTEM software[50] was used to test image processing parameters and generate 3D reconstructions. The 3D reconstructions were moved to a local desktop to view and interpret the data with Chimera[149].

3.3 RESULTS

Figure 3.2. shows a representative cryo-EM micrograph collected with the Titan Krios and the Gatan K3 direct electron detector. High quality images with good particle distribution were selected from areas in the perforated carbon holes and used for further image processing, ***Figure 3.3.*** Using RELION manual picking, 53,742 PSII particles were picked and a particle stack was generated. The stack was imported into the cisTEM software for further image processing. Using cisTEM, image processing parameters were tested to generate the 3D reconstruction. A wide range of class averages were tested (5-750 class averages). The best 3D reconstructions were from class averages between 10-25.

The initial 53,742 particles were grouped into 500 class averages (20 cycles). ***Figure 3.4*** shows the resulting class averages. A large number of particles are averaged into each class average to enhance the SNR. ***Figure 3.5*** shows individual particles that were averaged to generate the first class average. Then a 3D reconstruction was generated. ***Figure 3.6*** shows side and top view of the resulting 3D reconstruction. The estimated resolution is 18.48Å.

The 53,742 control PSII particles were grouped into 250 class averages (50 cycles). From these class averages, the best 40 class averages were selected (***Figure 3.7***). Using the selected class averages, a new Refinement Package (24,116 particles) was generated. Then the 24,116 particles from the new refinement package were grouped into 50 class averages (20 cycles) (***Figure 3.9***) From these classes, the best 10 class averages were selected, and a new Refinement Package (12,158 particles) was created. These 12,158 particles were grouped into 10 class averages (20 cycles) (***Figure 3.*10**) and a 3D reconstruction was generated. ***Figure 3.11*** shows side and top view of the resulting 3D reconstruction. The estimated resolution is 15.04Å.

Similar strategies were applied to select class averages of longer particles, which were assumed to be equivalent to the complete complex, from the initial 53,742 particles and generate a 3D reconstruction using class averages of longer particles only. ***Figure 3.***12 shows the resulting 3D reconstruction.

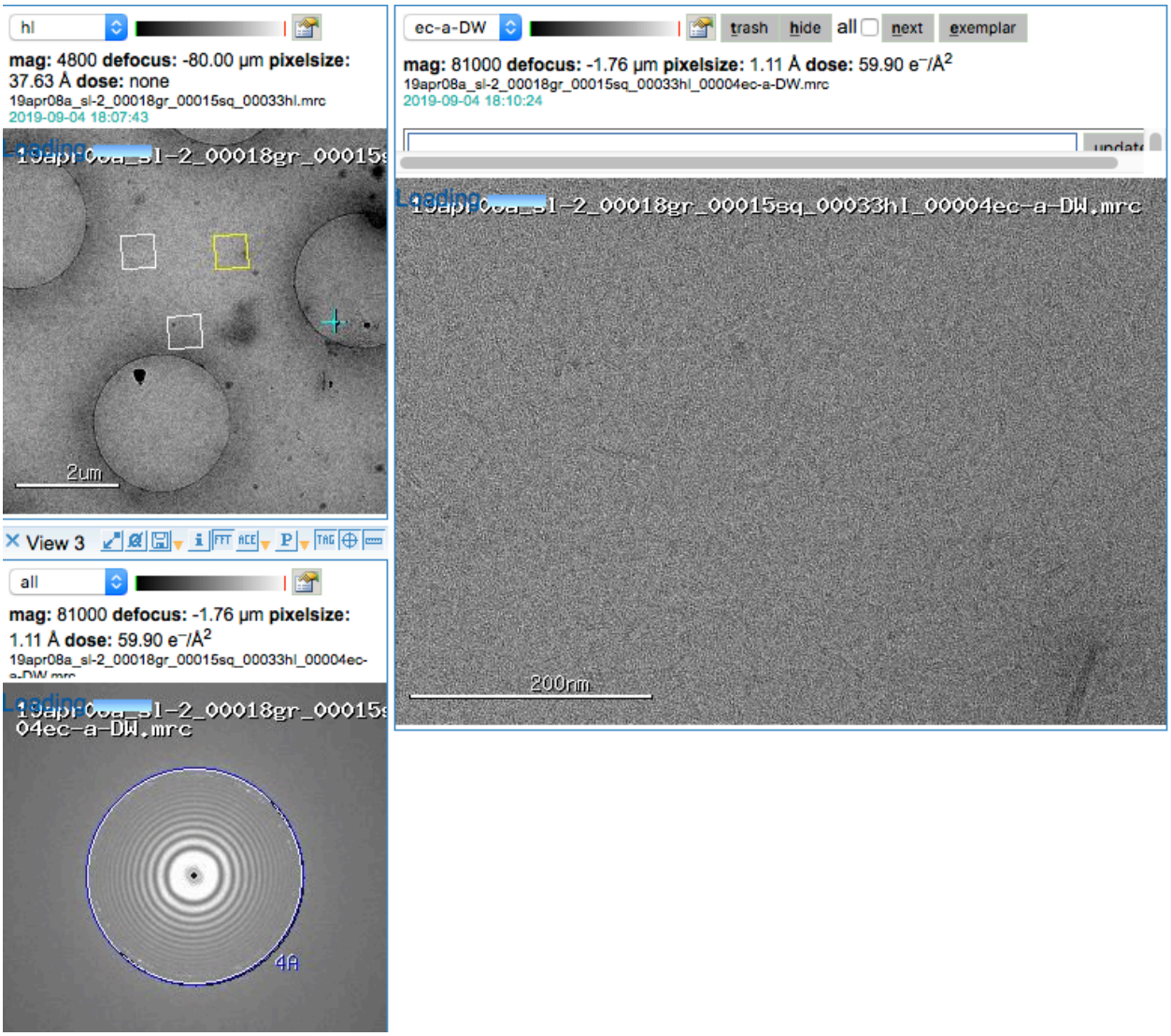

Figure 3.2. Cryo-EM image quality assessment of active (control) PSII sample. Cryo-EM image quality was evaluated for each image using 3 criteria: Particle presence and distribution (*right image*), location of the image area (*upper left window*), and the quality of the images via assessment of the CTF(*lower left window*). The image at the top was discarded because it was taken outside of the well.

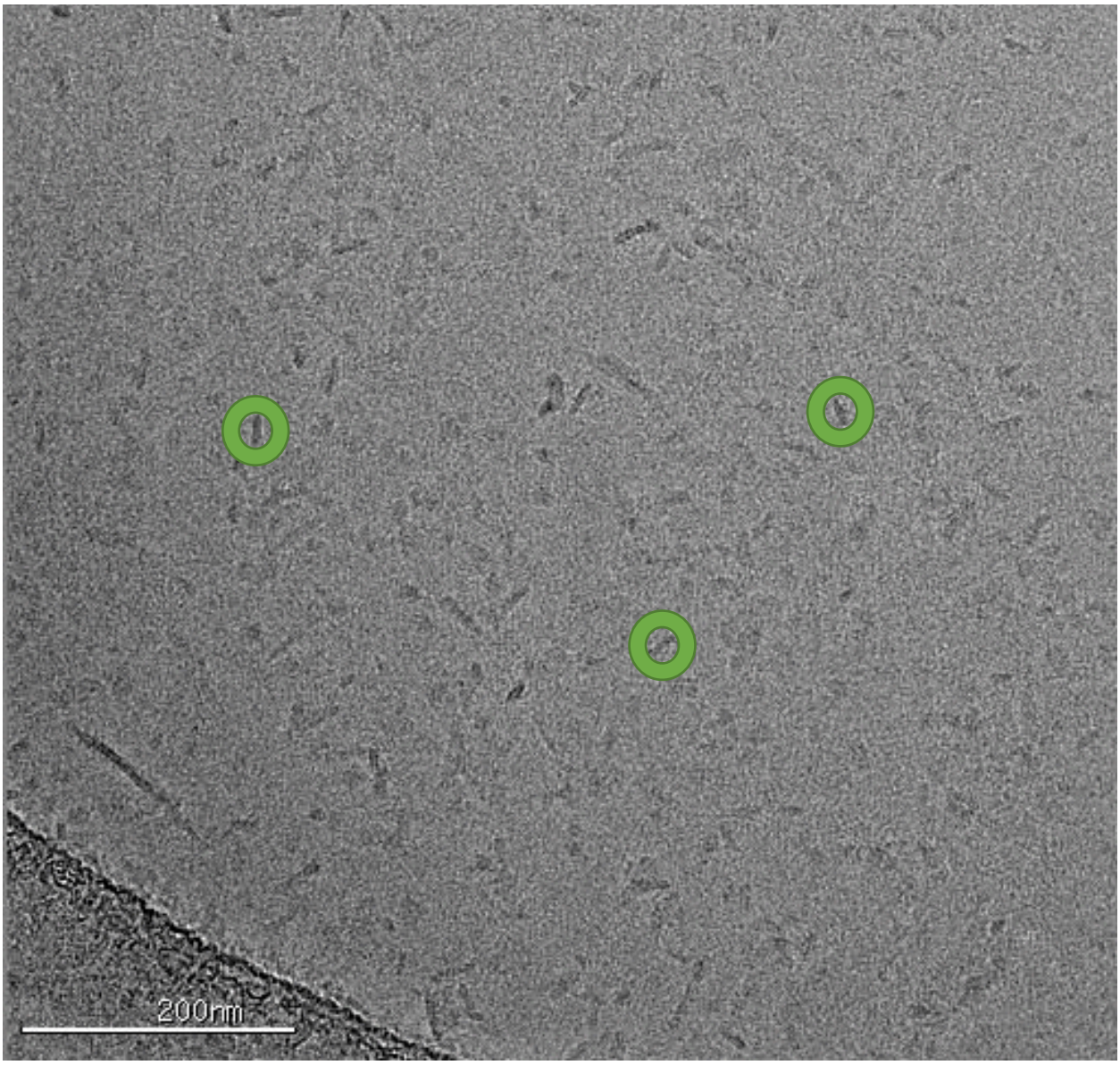

Figure 3.3. Representative Cryo-EM micrograph from the active (control) PSII data collection. The image shows a high quality micrograph that was taken from inside the perforated carbon. There is a good particle distribution, and the image was used for manual particle picking. Some of the particles are highlighted (green circles) The scale bar corresponds to 200nm.

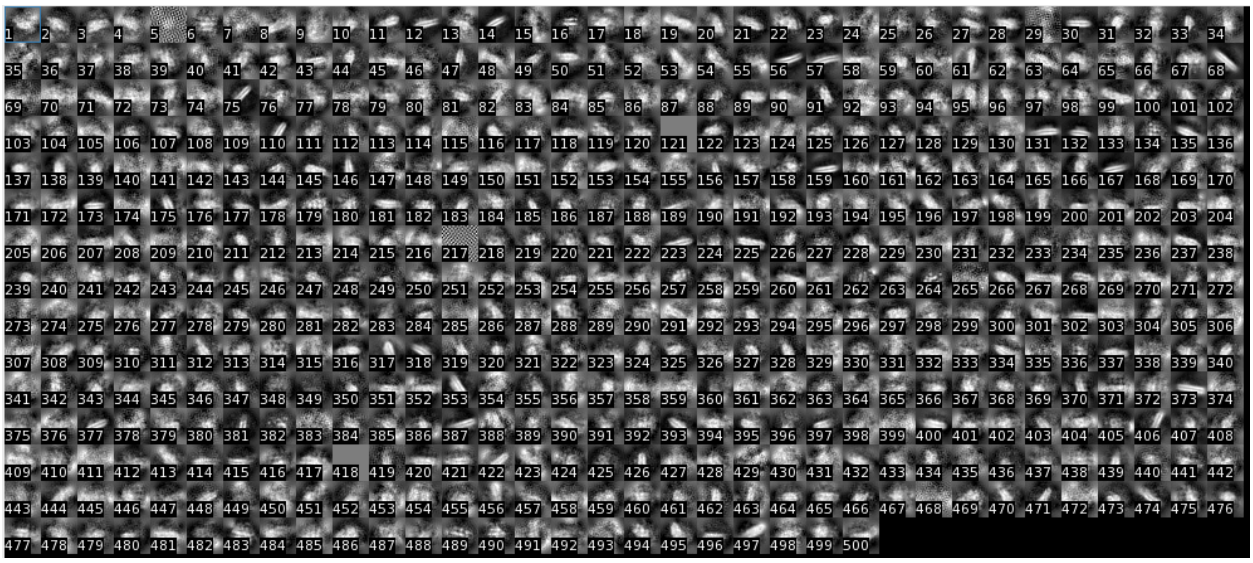

Figure 3.4. Class averages generated from active (control) PSII particles using cisTEM. The initial control PSII particles (53,742 particles) were grouped into 500 classes and averaged to enhance the signal. These class averages were used to generate the first 3D reconstruction of the control PSII sample.

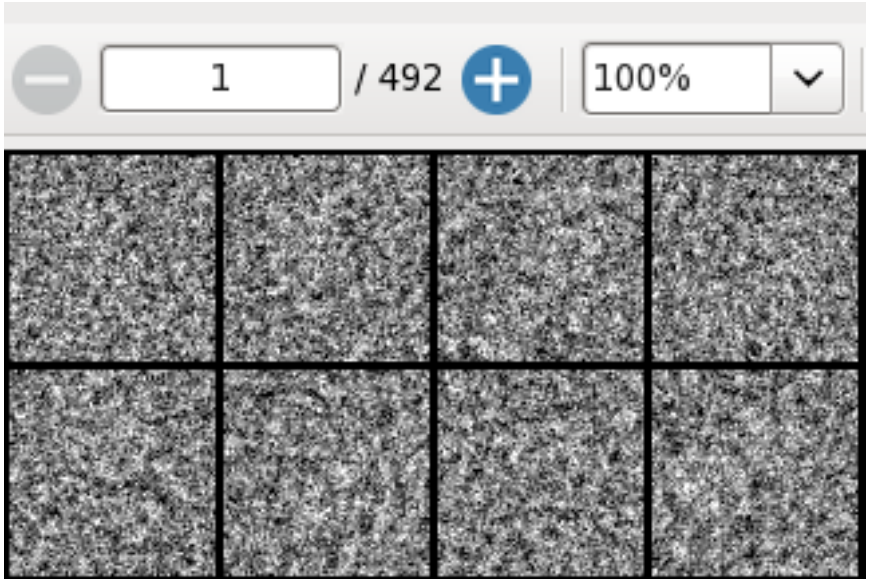

Figure 3.5. Images of individual PSII particles. By averaging 492 particles with the same orientation, the first class average in ***figure 3.4*** was generated.

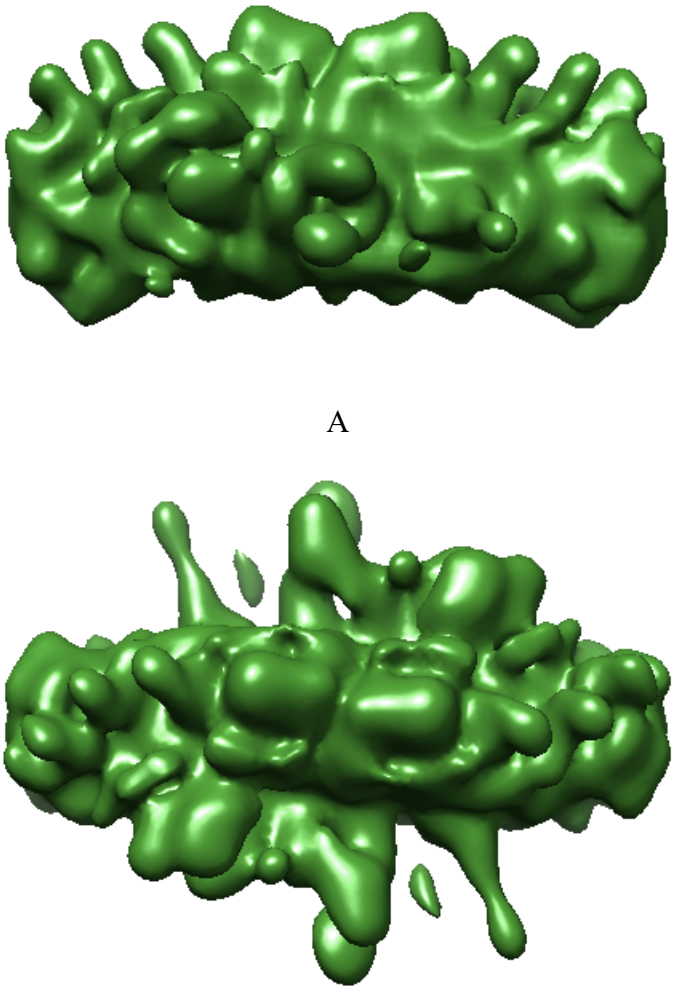

A

B

Figure 3.6. Class averages of active PSII were used to generate a 3D reconstruction. (A) shows a side view (the view parallel to the membrane) and (B) shows a top view (the view perpendicular to the plane of the membrane) of the 3D reconstruction. The estimated resolution is 18.48Å.

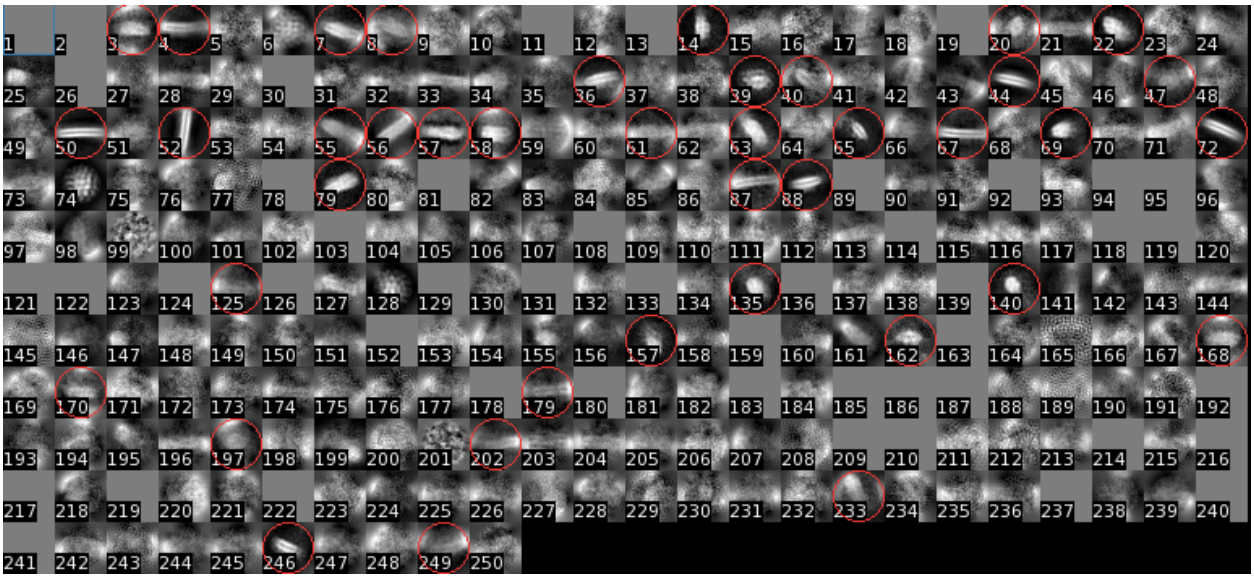

Figure 3.7. Class averages generated from active (control) PSII particles using cisTEM. The initial control PSII particles (53,742 particles) were used to generate 250 class averages (50 cycles). The best 40 class averages were chosen (red circles) to make a smaller but better-quality Refinement Package (24,116 particles).

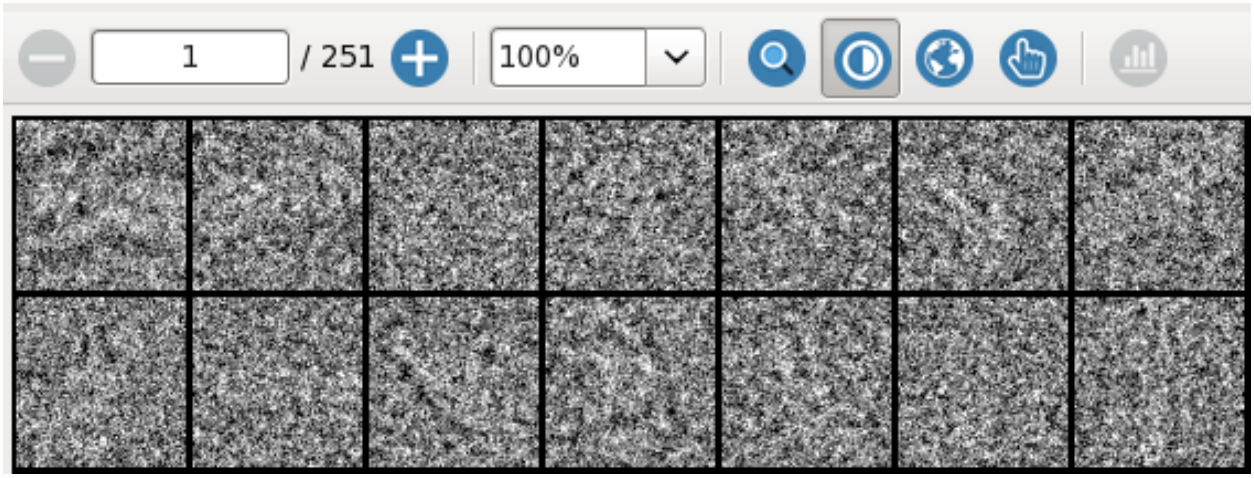

Figure 3.8. Individual PSII particles. By averaging 251 particles with the same orientation, the third class average was generated in ***figure 3.7.***

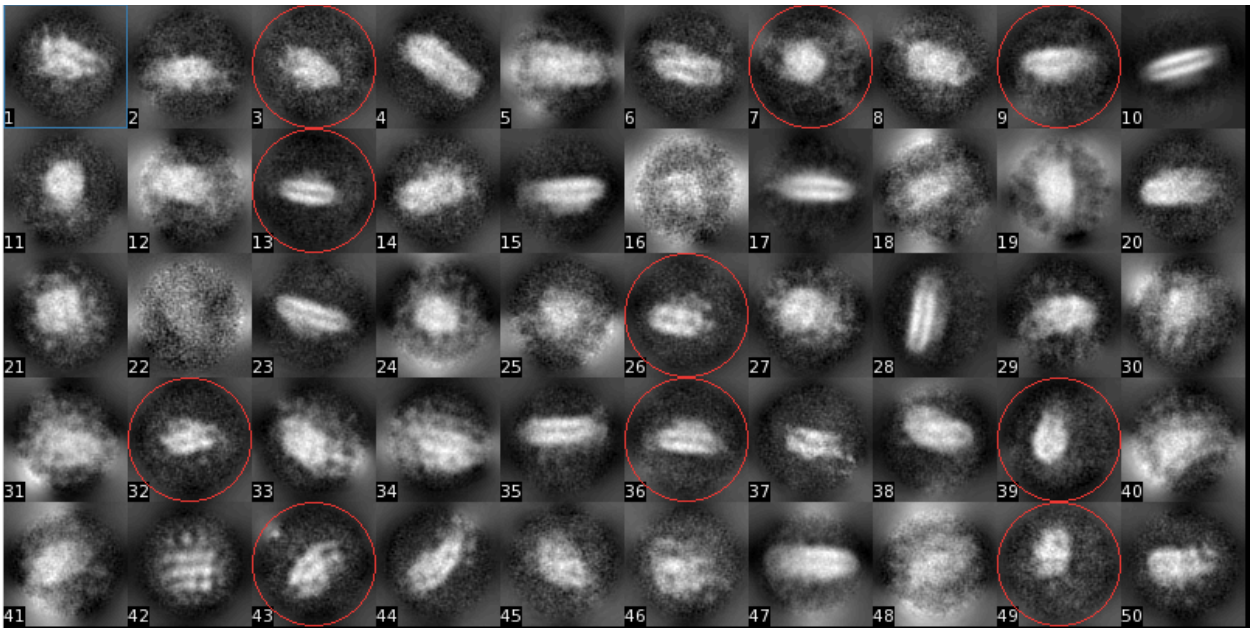

Figure 3.9. Class averages generated from active (control) PSII particles using cisTEM. A Refinement Package containing 24,116 particles was used to generate 50 class averages. From these class averages, the best 10 class averages were selected (red circles) to make a smaller but higher-quality Refinement Package (12,158 particles).

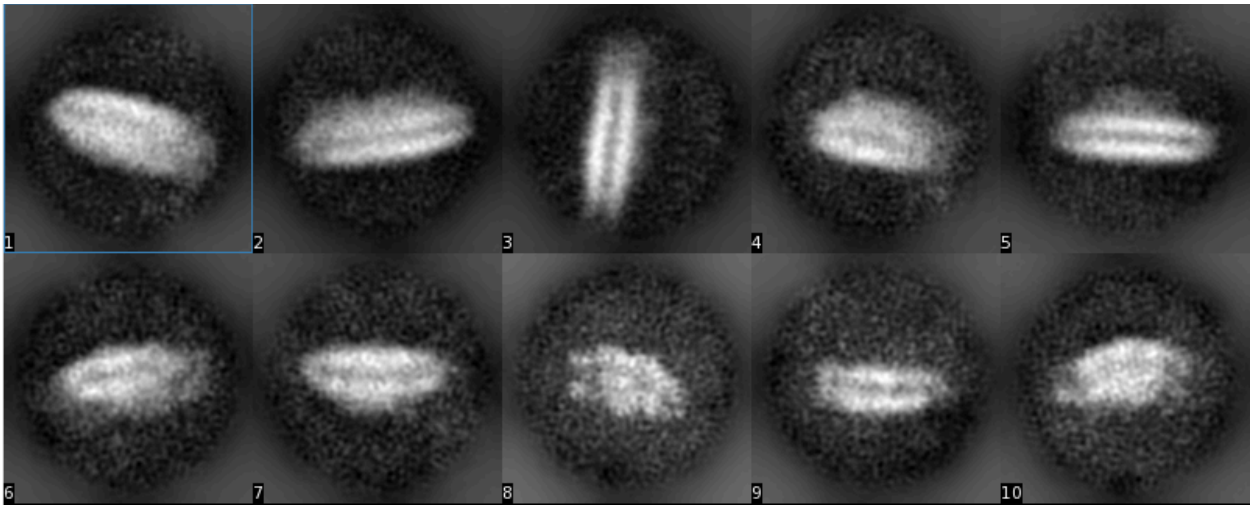

Figure 3.10. Class averages generated from active (control) PSII particles using cisTEM. A Refinement Package containing 12,158 particles was used to generate 10 class averages. These class averages were used to generate a 3D reconstruction for the control PSII sample.

A

B

Figure 3.11. Active PSII class averages (12,158 particles) were used to generate a 3D reconstruction. (A) shows a side view and (B) shows a top view of the 3D reconstruction. The estimated resolution is 15.04Å.

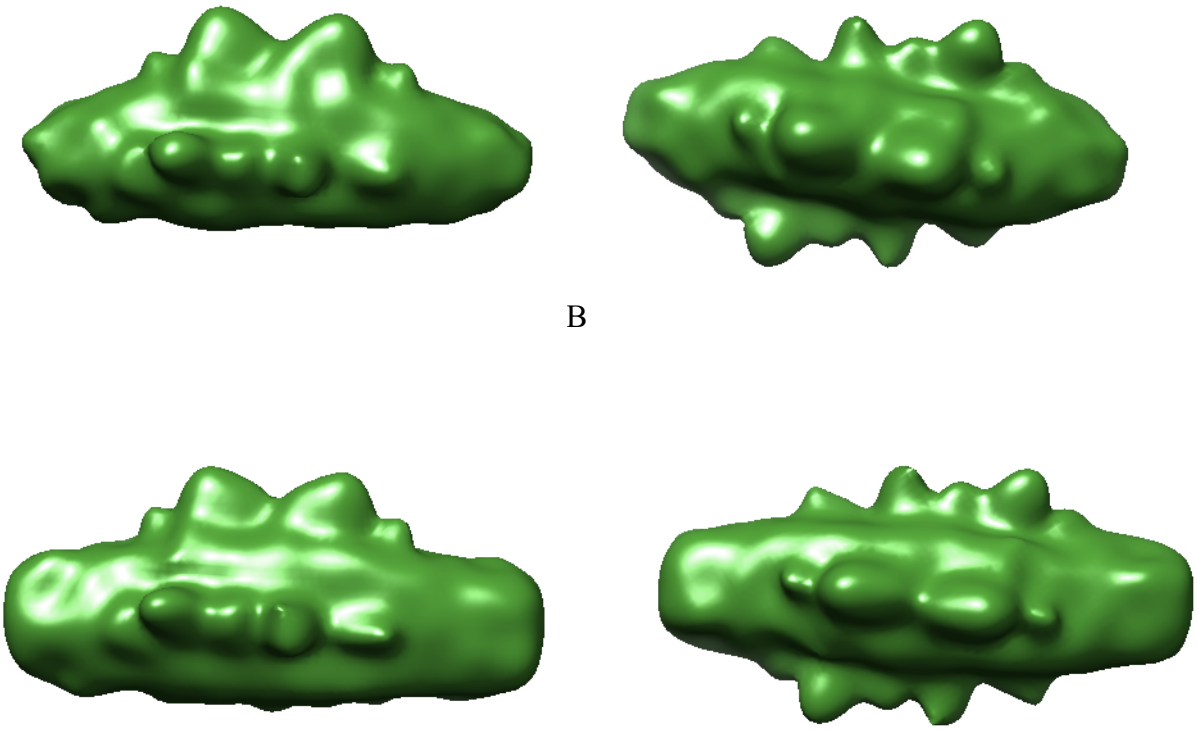

A B

C D

Figure 3.12. 3D reconstructions from short and long class averages, thought to correspond to the core complex and the complete/intact complex, respectively. Figure A (side view) and B (top view) show 3D reconstructions from selected short class averages. Figures C (side view) and D (top view) show 3D reconstructions from selected long class averages. The longer class averages contain PSII particles that still have their light harvesting complexes in place. Two different 3D reconstructions resulted from two different smaller Refinement Packages generated from the same initial Refinement Package.

3.4 DISCUSSION

Automatic particle picking was tested during initial image processing trials. Because of the gentle PSII purification, the PSII samples were heterogenous. The Appion DOG particle picker was not able to discern between particles and artifacts. In addition, it selected noise as well as small ice crystals. As a result, we chose manual particle picking, which resulted in a marked improvement of particles and resulting structures as well as control in the selection of specific particle sizes.

Each image was examined and particles matching the size and shape of PSII were picked using the RELION software[49]. We obtained 53,742 particles for the control PSII sample. The remaining steps of the image processing were done in cisTEM[50]. This software has been used successfully for a number of projects[150-153]. It is user friendly and at the same time the graphical user interface (GUI) allows substantial control over a large number of image processing steps. The software contains all necessary programs[154-157] which makes it a complete image processing pipeline for single particle cryo-EM.

Ideally, when doing single particle analysis, the particle of interest has random orientations in the vitrified ice which will provide a large number of different views that are important in obtaining the highest quality 3D structures in terms of resolution and completeness. In addition, the largest possible number of particles is often critical towards achieving these goals. These two parameters were hurdles for the active PSII samples. During particle picking, preferred orientations were observed. There were many side views and few particles that appeared to be top and bottom views as well as other orientations of PSII (***Figure 3.3***). Several rounds of class averaging were performed and inferior, or "bad", particles were excluded from further image processing after the initial class averaging step. Only the best class averages were

selected, and a new Refinement Package was generated. In the process, the bad particles were discarded. This can be considered purification at the image processing step. The process was iterated multiple times, each time the best class averages were kept, and the bad ones were excluded. Even though the number of particles were reduced, the 3D reconstruction resulting from these particles appeared substantially less noisy and had higher resolution (15Å). However, there is a limit to the number of particles that can be discarded without the 3D reconstruction becoming noisy and a decrease in resolution.

After several rounds of conservative removal of substandard particles, the resolution of the 3D reconstruction eventually became worse. Even though bad particles were discarded, good particles that may have been averaged with bad particles in the same class were lost. It is also possible the lost particles were rare views of PSII. The class average from few rare views can be expected to be noisy. These rare but important views were likely lost in the process. As a result, the 3D reconstruction generated from a Refinement Package that did not contain these particles eventually became noisy and lower in resolution. To avoid this type of deterioration, we used one of the best Refinement Packages (24,116 particles) that provided the highest resolution. This Refinement Package contained approximately half of our initial particles for the control PSII sample. All of the obvious noisy class averages were discarded, however it likely contained rare PSII views that were discarded along with bad class averages during the multiple rounds of Refinement Package cleaning. Another smaller Refinement Package (12,158 particles) provided similar results. These two Refinement Packages were very useful for the control PSII sample processing because they gave the best results and made it possible to investigate other image processing parameters.

While examining the quality of the class averages, some interesting variations in the class averages could be identified. Several of the class averages showed longer particles than others. The differently-sized class averages represent the different species of PSII complexes, which were to be expected based on the gentle purification and sample characterization [147]. The shorter class averages of an approximate size of 25nm correspond to PSII species that consist of mainly the core complex while the longer class averages class averages were approximately 32-35nm. These particles correspond to the entire PSII complex and particles that may be missing certain subunits. Among these subunits are light harvesting complexes present and chlorophyll binding protein 26kD (CP26). This is not surprising because PSII particles lose subunits during purification.

Generally, a homogenous sample is by far preferred. However, the heterogeneous nature of our sample provided an opportunity to pick only a specific PSII species and use this subset of particles for a new Refinement Package. That Refinement Package was then used to generate a 3D reconstruction. Two different Refinement Packages were generated based on two subsets of class averages. The first Refinement Package contained short class averages which consisted of short particles while the second Refinement Package contained long class averages which consisted of long particles. Indeed, the two Refinement Packages resulted in two different 3D reconstructions (***figure 3.12.***).

Given that a large data set is available, this kind of image processing can be used for heterogeneous samples in various ways. In our studies, we are categorizing particles by size. However, it is also possible to use this approach to determine the structure of a protein in different conformational states and to capture entire mechanisms depending on the sample[158]. After aligning our structure with other structures, we were able to determine the 3D

reconstruction from the shorter class averages is missing the CP26 subunit ***Figure 3.12***. This subunit is present in the 3D reconstruction generated from the longer class averages ***Figure 3.12***. A comparison of our active PSII 3D reconstruction onto a spinach structure is shown in chapter 4.

In this study, we were able to obtain different low resolution 3D reconstruction from a heterogeneous sample. Ultimately, our goal is to obtain high resolution structure of the active PSII. Chapter 5 discusses the different approaches we can take to achieve this goal at the sample preparation, data collection, and image processing steps.

3.5 ACKNOWLEDGMENTS

I would like to thank Dr. Bridgette Barry's laboratory for the PSII project collaboration. Dr. Yusuf Uddin provided the PSII sample and training in the gentle PSII purification.

I would also like to thank Carolann Espy, Tajah Damm, and Eric Woods for helping with manual particle picking and image processing. I want to thank my Ph.D. Advisor Dr. Schmidt-Krey for her feedback and guidance on our PSII data collection and image processing

I also would like to thank Dr. Stroupe's Laboratory at Florida State University and particularly Dr. Jay Rai. Dr. Nilakshee Bhattacharya is much appreciated for overseeing the automated cryo-EM data collection via the NIH U24 consortium on the Titan Krios at Florida State University and many valuable discussions.

CHAPTER 4: SINGLE PARTICLE ANALYSIS OF PSII SALT WASH AND UREA WASH COMPLEXES

4.1 INTRODUCTION

Light is critical to PSII to function. Under light stress, however, PSII can lose its activity because of damaged subunits. This process is known as photoinhibition[159]. In order for PSII to function properly, the damaged subunits have to be replaced. Usually, these damaged subunits are the extrinsic subunits PsbO (26.5 kDa), PsbP (16.5 kDa), and PsbQ (20 kDa) that play key roles in PSII function[160]. PSII replaces the damaged subunits with new subunits. This repair mechanism is thought to involve conformational changes to accommodate the repair[161].

In the laboratory, photoinhibition conditions can be mimicked by treating purified PSII sample with high levels of salt and urea to remove specific subunits in a controlled manner[162] [163]. Treatment with a "salt wash" removes PsbP and PsbQ while treatment with a "urea wash" removes PsbO, PsbP, and PsbQ[160, 163, 164].

PSII Sample	Extrinsic Subunits Present
Control PSII	PsbO, PsbP, and PsbQ
Salt Wash PSII	PsbO (PsbP and PsbQ are removed)
Urea Wash PSII	No Extrinsic Subunits (PsbO, PsbP, and PsbQ are removed)

Table 4.1. Extrinsic subunits present in the 3 PSII samples. The control PSII sample has all of its extrinsic subunits present. Salt wash PSII retains only one extrinsic subunit (PsbO). Urea wash PSII has no extrinsic subunits present.

A

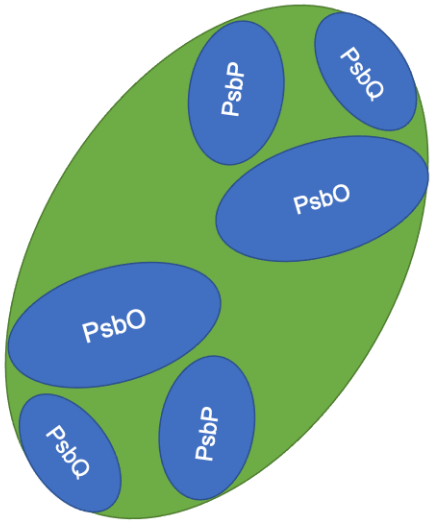

A

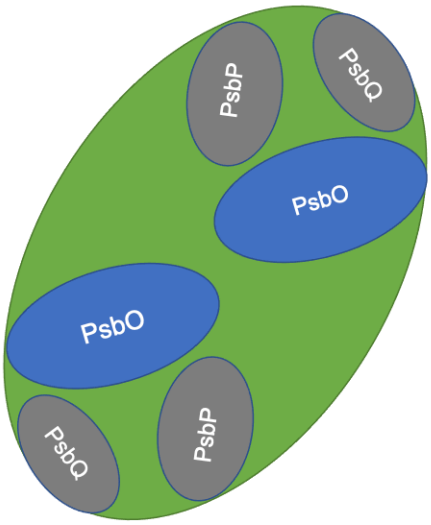

B

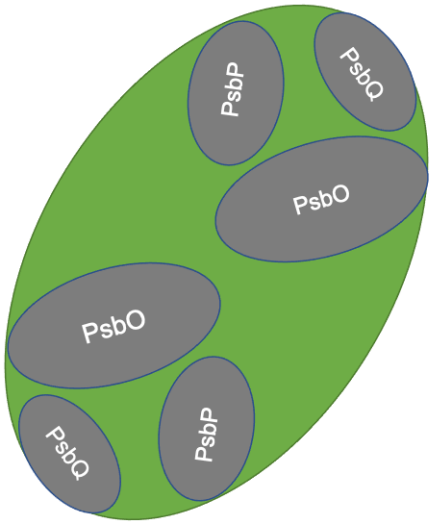

C

Figure 4.1. Schematic representation showing location of the extrinsic subunits in active (control) PSII, salt wash PSII, and urea wash PSII. (A) In the active PSII, all extrinsic subunits (PsbO, PsbP, and PsbQ) are present (shown in blue). (B) Salt wash treatment removes PsbP and PsbQ (shown in grey). (C) Urea wash treatment removes all extrinsic subunits (shown in grey).

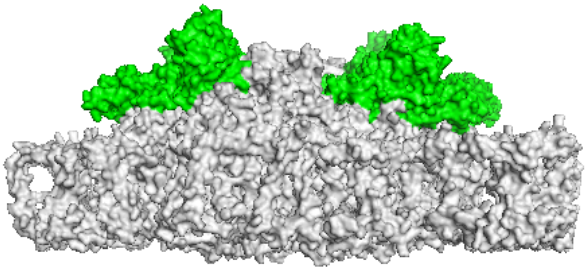

A

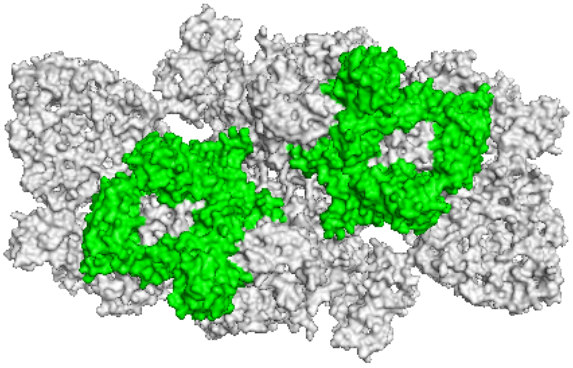

B

Figure 4.2. Inactive spinach PSII (PDB ID: 3JCU) showing extrinsic subunits (PsbO, PsbP, and PsbQ. **(A)** shows the side view and **(B)** shows the top view.

The active (control) PSII, which has all of the extrinsic subunits, was studied along with salt and urea treated PSII in order to examine the structures of these PSII complexes to ultimately understand the conformational changes that take place in the photoinhibition repair mechanism. Furthermore, by comparing the 3D reconstructions from the control, salt wash, and urea wash PSII samples, it is possible to examine the presence of the extrinsic subunits and determine their

exact locations under these conditions [163, 164]. Studying and understanding the conformational changes that take place under these conditions not only give fundamental insights into the photoinhibition and PSII repair mechanism, but it also has other potential practical applications. The information can potentially be used to plants more resistant to stressful conditions. This is critical as the world's population is increasing rapidly and the need for plants as a source of food is becoming a necessity in a changing environment.

4.2 PSII EXPERIMENTAL PROCEDURES

4.2.1 PURIFICATION OF ACTIVE PSII AND SALT AND UREA TREATMENTS

PSII samples were purified as detailed in chapter 3 to obtain the OTG-PSII sample. In order to mimic photoinhibition, OTG-PSII was treated with either high salt or urea buffers to remove the extrinsic subunits in a controlled manner. For the salt wash PSII sample, OTG-PSII was treated with high ionic strength buffer (2M NaCl, 400 mM sucrose, 50 mM MES-NaOH, pH 6). This removed the extrinsic subunits PsbP, and PsbQ. For the urea wash PSII sample, OTG-PSII was treated with urea-containing buffer (2.6 M urea, 400 mM sucrose, 50 mM MES-NaOH, 200 mM NaCl, pH 6). After either the salt wash or urea wash treatment, the buffer was exchanged to OPDM buffer (0.3% β-DDM, 50 mM MES-NaOH, 10 mM NaCl, 20% sucrose, pH 6). The sample concentration was adjusted to 1mg/ml and samples were flash frozen in liquid nitrogen.

4.2.2 SALT WASH AND UREA WASH PSII CRYO-EM GRID PREPARATION

A thin layer of carbon was used to make cryo-wells using C-flat grids. These grids were baked overnight at 50°C. The grids were glow discharged at 15 mA for 15 seconds in an Argon gas environment. For both salt wash and urea wash samples, cryo-EM grids were prepared by pipetting 3 μL of sample onto the glow-discharged grids in a dark room. A Vitrobot was used to plunge-freeze the grids in a controlled environment (100% humidity, 4°C, blot times of 3-6 seconds). Then the grids were stored in liquid nitrogen until data collection.

4.2.3 SALT WASH AND UREA WASH PSII DATA COLLECTION AND IMAGE PROCESSING

Salt wash and urea wash samples were imaged at Florida State University using Titan-Krios cryo-EM equipped with DE-64 and K3 direct electron detectors. The DE-64 direct electron detector was used to collect images of the salt wash PSII and urea wash samples. Each image was evaluated via Appion[148]. After frame alignment and CTF estimation, particles were manually picked from each micrograph using the RELION software[49]. Then particle stacks were created and imported from Florida State University High Performance Computing (HPC) to the Georgia Institute of Technology Partnership for Advance Computing Environment (PACE). The cisTEM software[50] was used to test image processing parameters and generate 3D reconstructions. The 3D reconstructions were moved to local desktop to view and interpret them using Chimera[149].

4.3 RESULTS

From the micrographs collected with the Titan Krios, 1,475 salt wash PSII particles and 9,192 urea wash PSII particles were manually picked using RELION. ***Figure 4.3*** and ***Figure 4.6*** show representative cryo-EM micrographs from the salt wash and urea wash PSII samples. After picking particles from the salt wash and urea wash PSII samples, particle stacks were generated. The stacks were imported into cisTEM software to complete image processing. Using cisTEM, various image processing parameters were examined to optimize the resulting 3D reconstruction. Class Averages between 5-100 were tested for both salt and urea wash samples. The best 3D reconstructions were from class averages between 10-25. ***Figure 4.4*** and ***Figure 4.7*** show 25 class averages generated using 1,475 salt wash and 9,192 urea wash PSII particles respectively. Then the class averages were used to generate 3D reconstruction. The 3D reconstructions had estimated resolution of 17.37Å for both salt wash and urea wash samples.

The 3D reconstructions from each sample were analyzed using UCSF Chimera. ***Figure 4.5*** and ***Figure 4.8*** show the side and top view of the 3D reconstructions generated from the salt wash and urea wash PSII samples, respectively. Consistent with anticipated results, the densities for PsbP and PsbQ were missing in the salt wash 3D reconstruction. The densities for PsbO, PsbP, and PsbQ were missing in the urea wash 3D reconstruction. The presence and absence of the extrinsic subunits also can be clearly observed in the class averages. ***Figures 4.9-4.11*** show the class averages from the control, salt wash, and urea wash PSII samples.

The 3D reconstructions from active, salt wash, and urea wash were superimposed with a spinach structure (PDB ID: 3JCU) to compare our work with others (***Figure 4.12- Figure 4.14***). In the superimposed figures, the presence and absence of different extrinsic subunits were examined. When comparing the active PSII 3D reconstruction with the spinach structure, the

densities for all extrinsic subunits are present in the active PSII reconstruction (***Figure 4.11***). In the comparison between the spinach structure and the salt wash PSII 3D reconstruction, it is clear PsbP and PsbQ are missing from the 3D reconstruction (***Figure 4.12***). When comparing the urea wash 3D reconstruction with the 3JCU structure, the densities for all the extrinsic subunits are missing (***Figure 4.13***). Furthermore, all of the 3D reconstructions were compared with one another (***Figure 4.15- Figure 4.17***). When comparing the control 3D reconstruction with the salt wash 3D reconstruction, we see the missing densities for PsbP and PsbQ. When comparing the control 3D reconstruction with the urea wash, the crown like density is missing in the urea wash 3D reconstruction. When the salt and urea wash are compared, we see density for PsbO in the salt wash but not in the urea wash. This is expected as the urea wash removes all extrinsic subunits. While the presence and absence of the extrinsic subunits can be analyzed, it is definitely worth being cautious as it would be better supported with higher resolution 3D reconstruction. Some areas of the 3D reconstructions are very noisy.

Salt Wash PSII

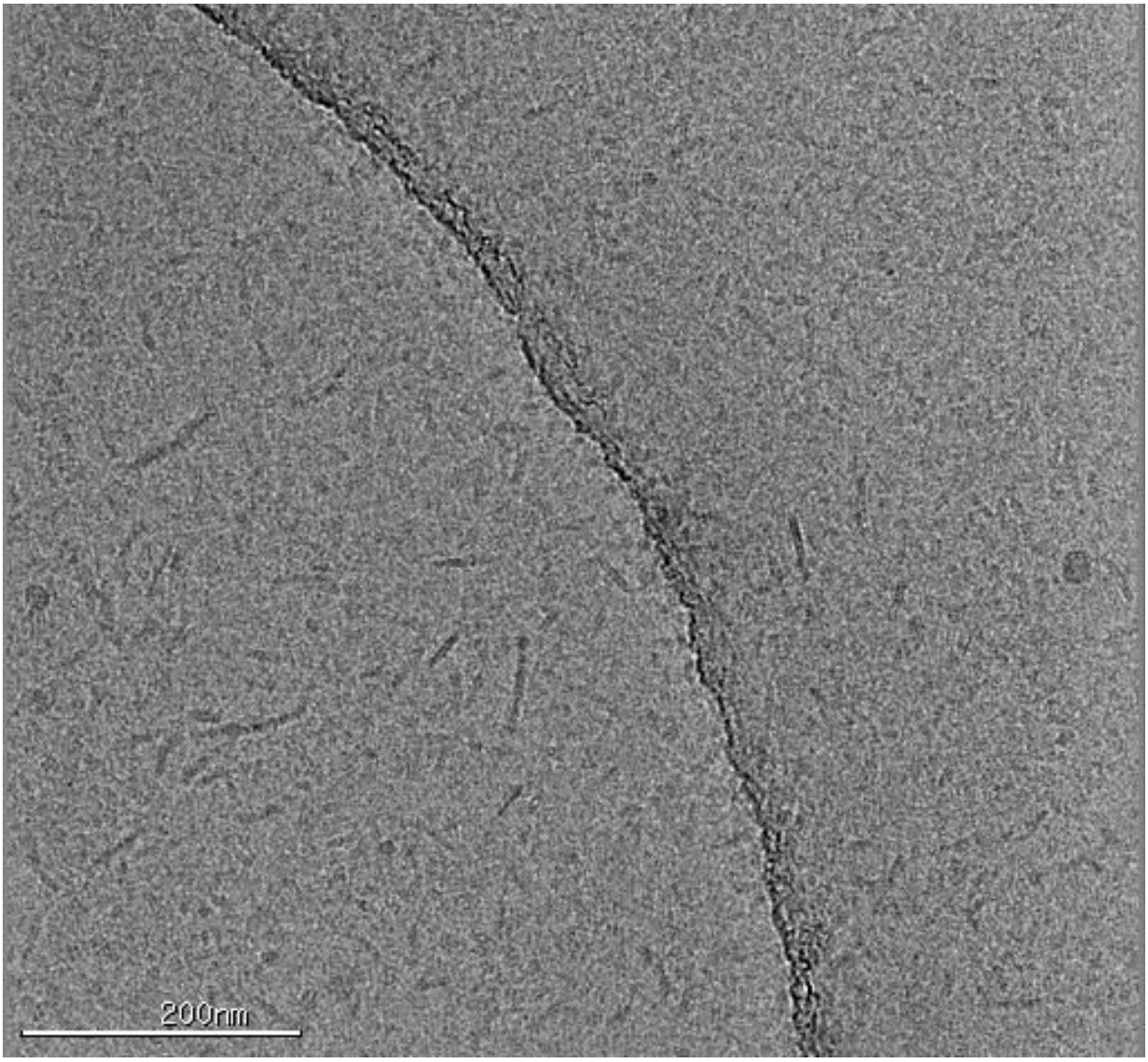

Figure 4.3. Representative Cryo-EM micrograph from the salt wash PSII data collection. PSII sample was treated with ionic strength buffer containing high salt concentrations to remove the extrinsic subunits PsbP and PsbQ. The scale bar corresponds to 200nm.

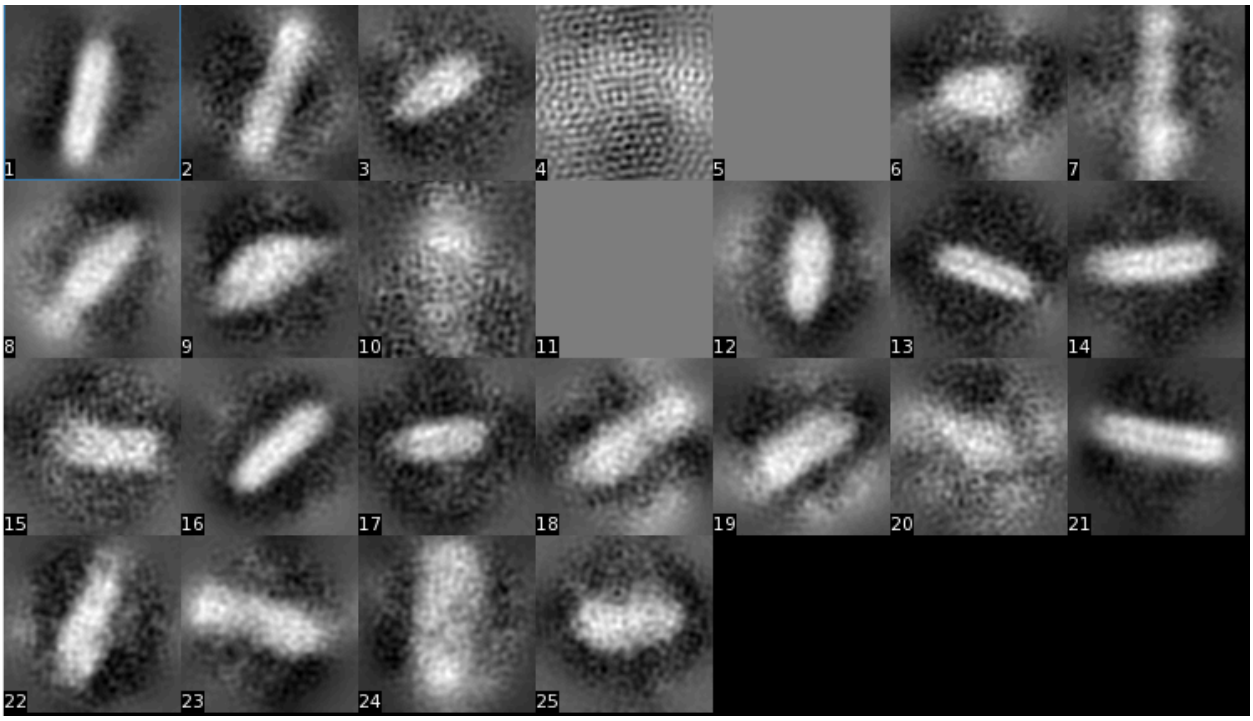

Figure 4.4. Class averages generated from salt wash PSII particles using cisTEM. Salt wash PSII particles (1,475 particles) were categorized into 25 classes and averaged to enhance the signal. These class averages were used for 3D reconstruction.

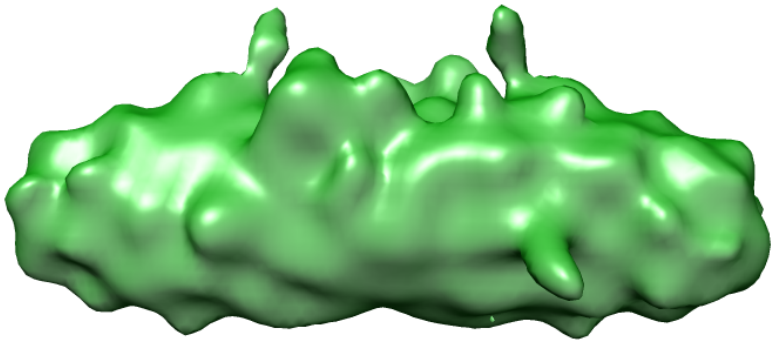

A

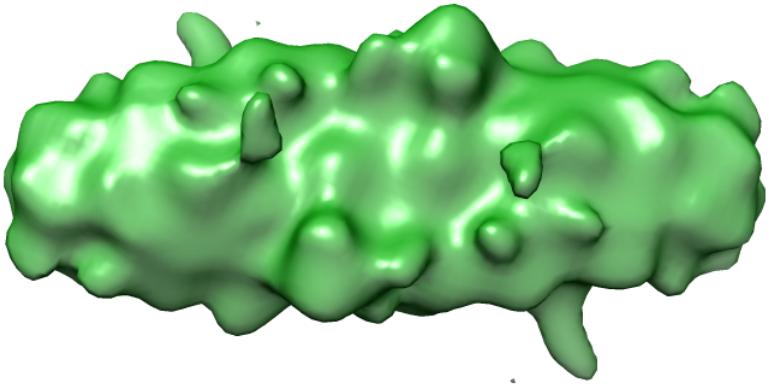

B

Figure 4.5. Salt wash PSII class averages were used to generate 3D reconstruction. **(A)** shows a side view and **(B)** shows a top view of the 3D reconstruction. Estimated resolution = 17.37Å. The densities for PsbP and PsbQ are missing.

Urea Wash PSII

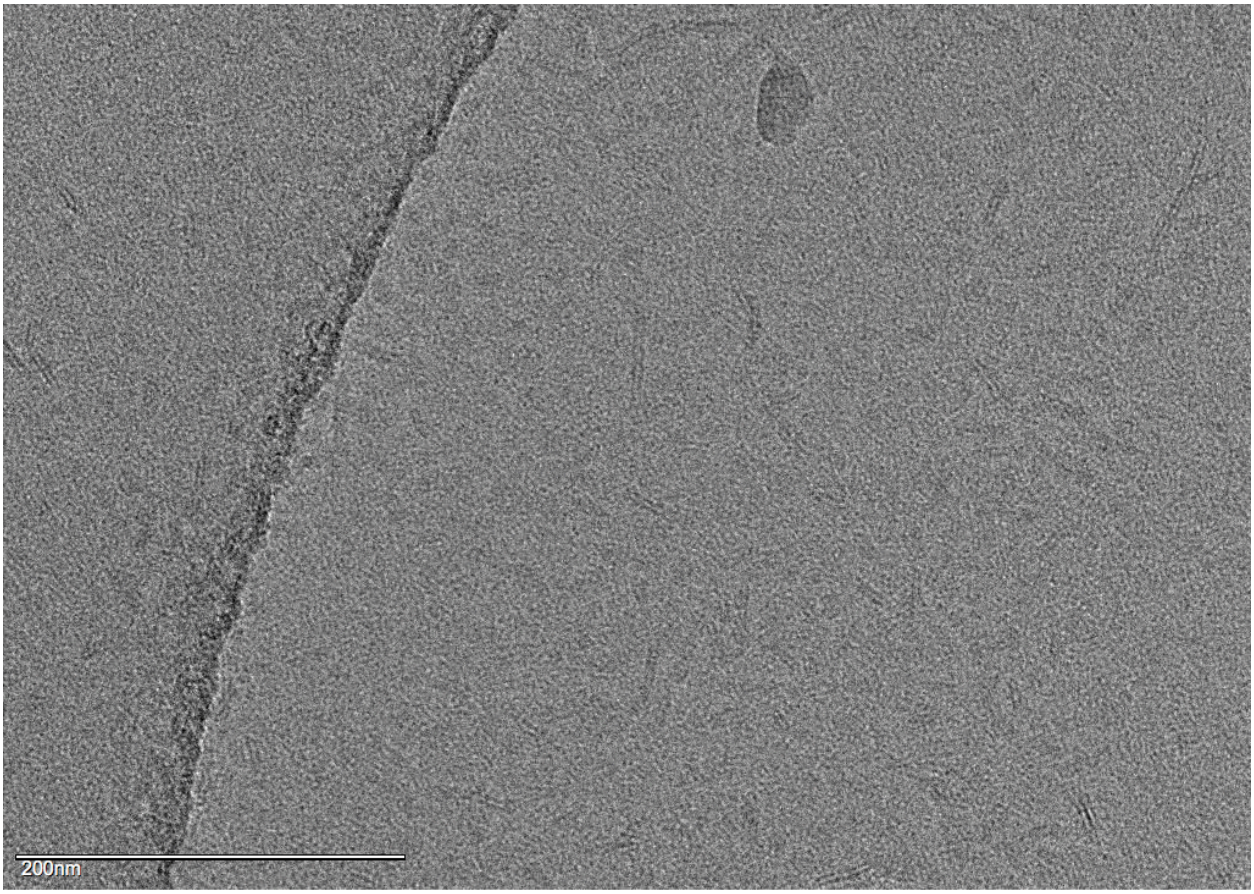

Figure 4.6. Representative Cryo-EM micrograph from the urea wash PSII data collection. PSII sample was treated with urea buffer to remove the extrinsic subunits PsbO, PsbP, and PsbQ. The scale bar corresponds to 200nm.

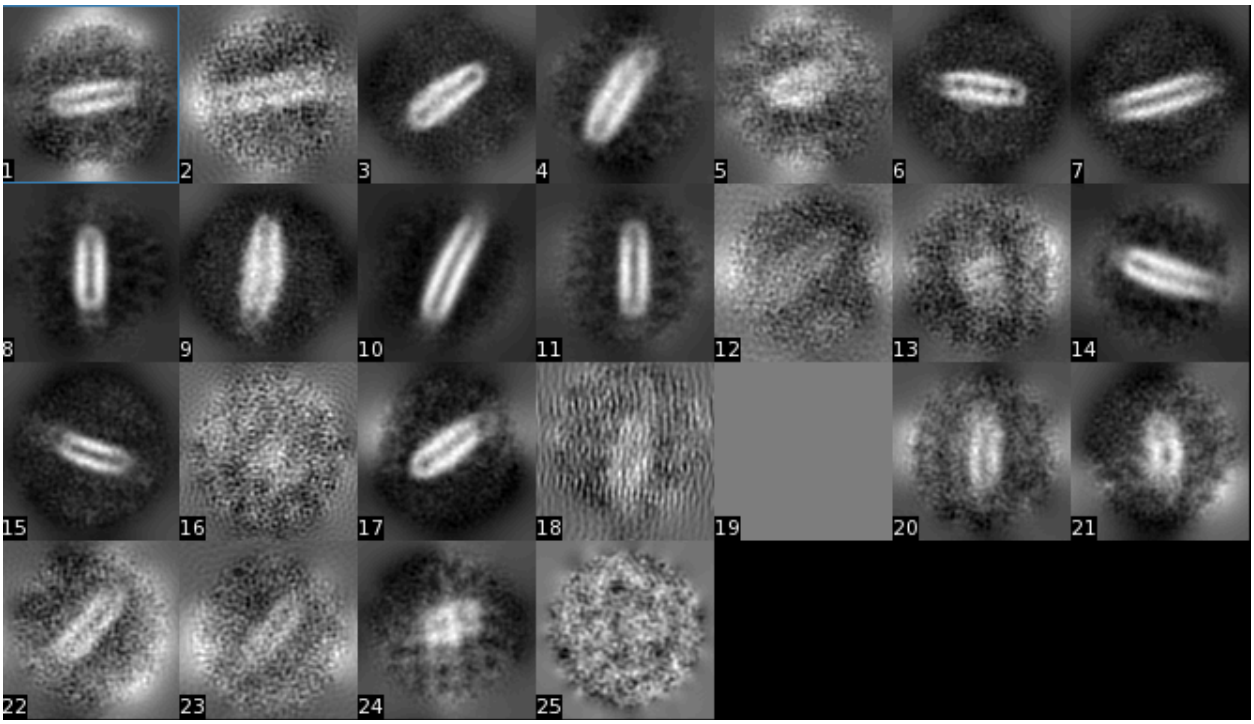

Figure 4.7. Class averages generated from urea wash PSII particles using cisTEM. Urea wash PSII particles (9,192 particles) were categorized into 25 classes and averaged to enhance the signal. These class averages were used for the 3D reconstruction.

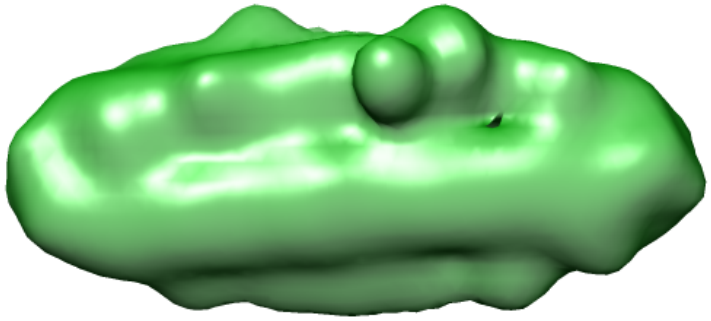

A

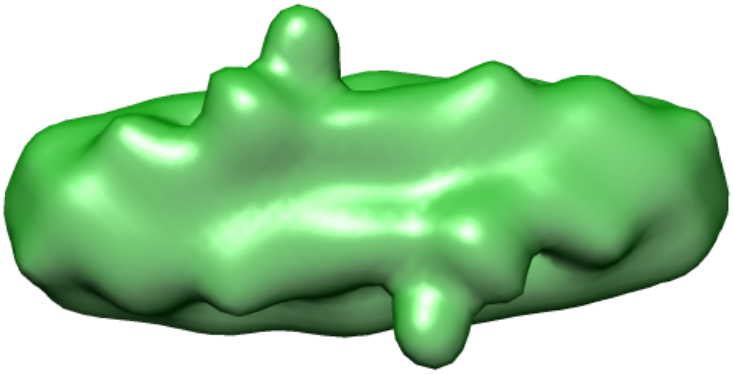

B

Figure 4.8. Urea wash PSII class averages were used to generate 3D reconstruction. (A) shows a side view and (B) shows a top view of the 3D reconstruction. The estimated resolution is 17.37Å. The densities for all extrinsic subunits (PsbO, PsbP, and PsbQ) are missing.

CLASS AVERAGES: CONTROL, SALT WASH, AND UREA WASH PSII

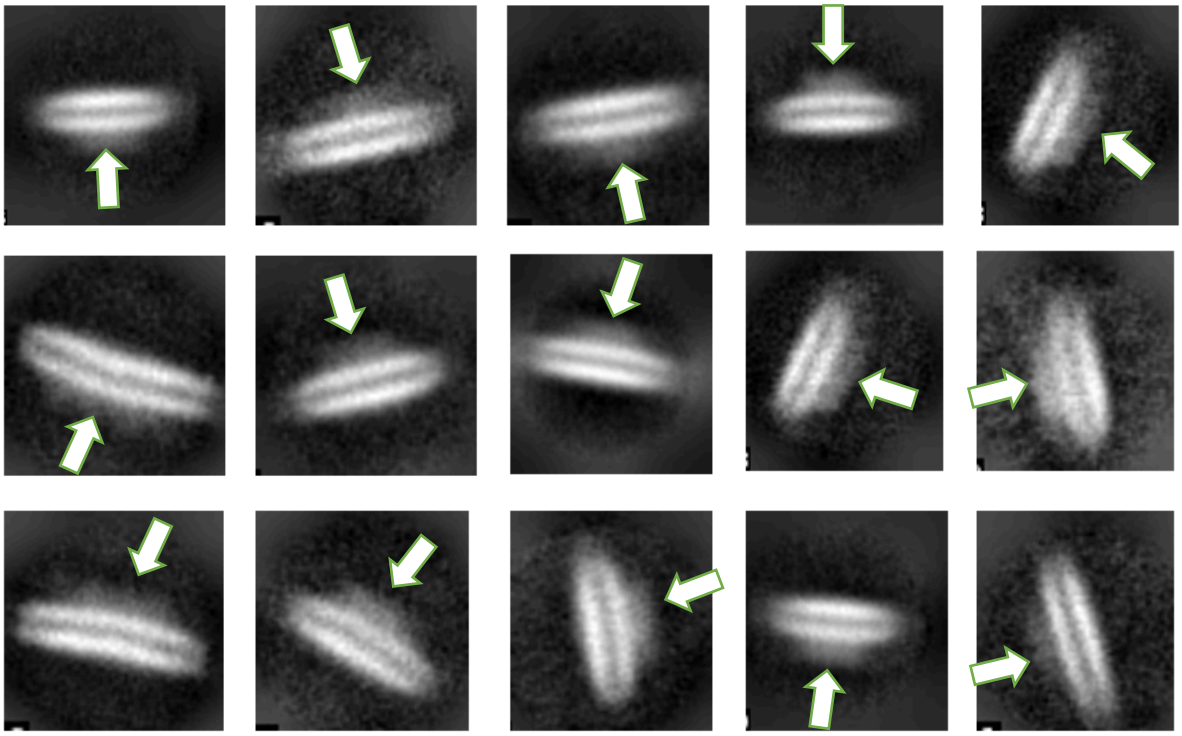

Figure 4.9. Class averages from the control PSII sample. The class averages clearly show the presence of the extrinsic subunits PsbO, PsbP, and PsbQ (Indicated by the arrows).

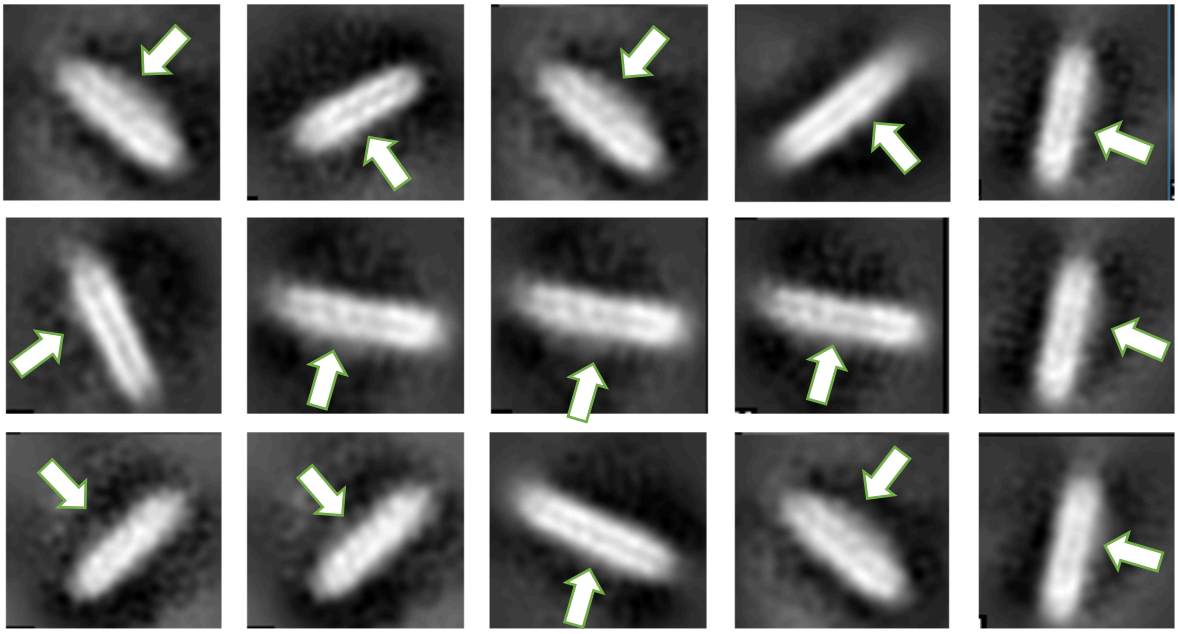

Figure 4.10. Class averages from the salt wash PSII sample. The class averages show a weaker density, possibly indicating the presence of the extrinsic subunit (PsbO) (Indicated by the arrow) and absence of the PsbP and PsbQ subunits.

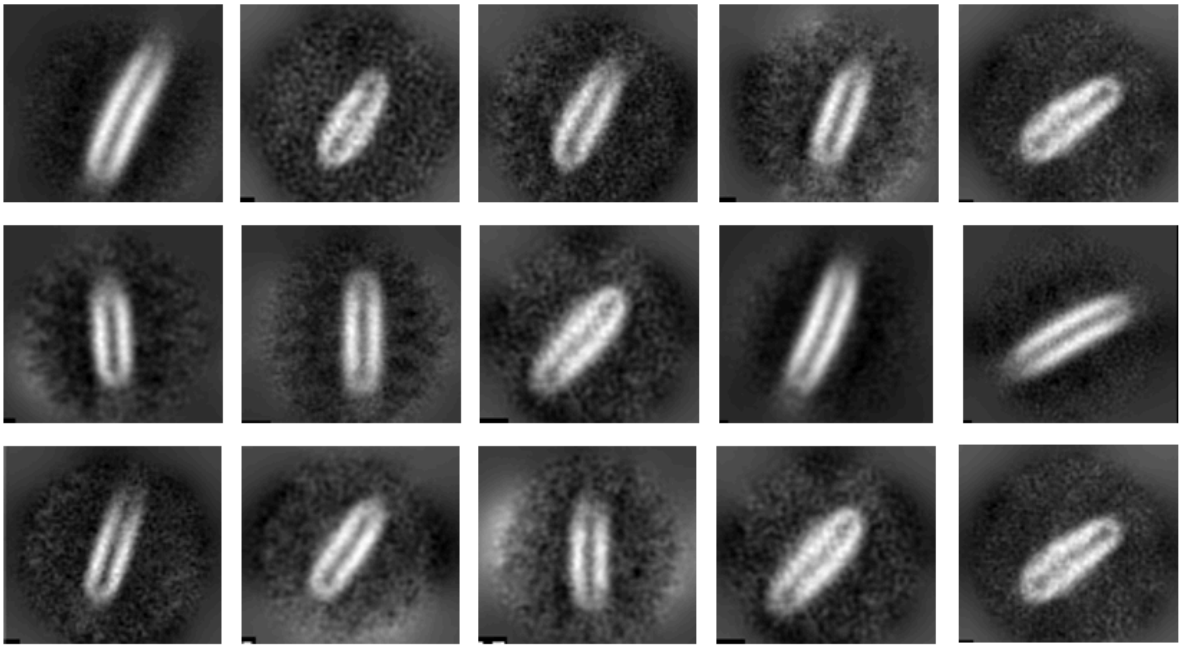

Figure 4.11. Class averages from the urea wash PSII sample. The class averages show no extrinsic subunits are present. The crown shape is not visible in the class averages.

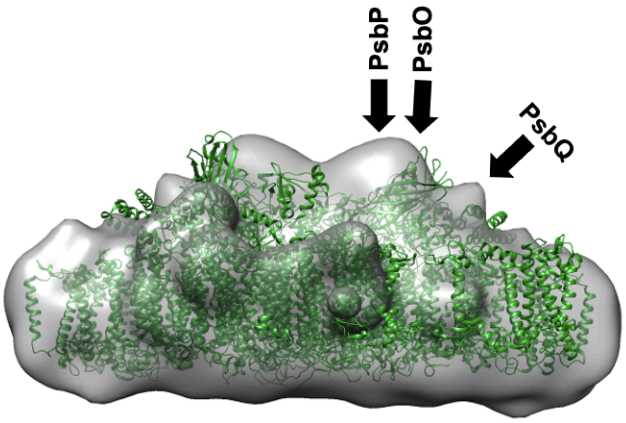

A

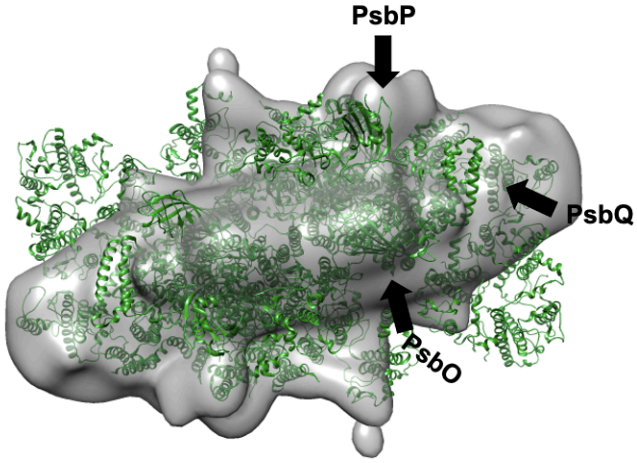

B

Figure 4.12. Superimposed comparison of active PSII 3D reconstruction with spinach PSII structure (PDB ID: 3JCU). (A) shows a side view and (B) shows a top view of the comparison. PSII is a homodimer in both structures. The extrinsic subunits are labeled in one monomer to show their location. The comparison shows the densities for all extrinsic subunits are present in the active PSII 3D reconstruction.

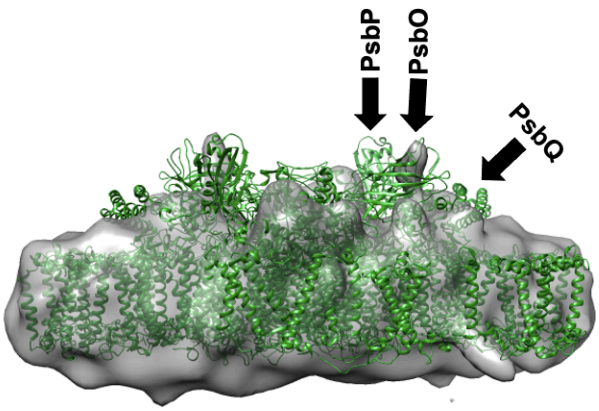

A

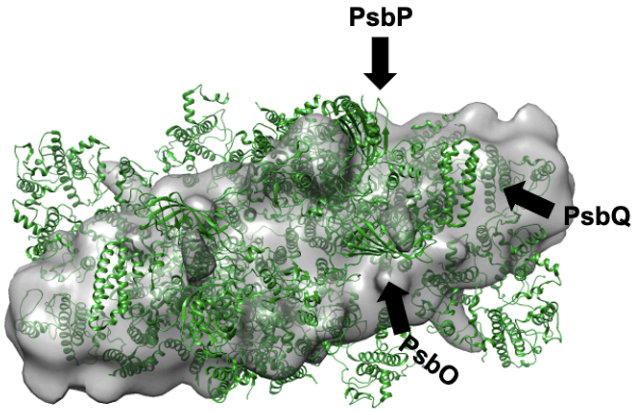

B

Figure 4.13. Superimposed comparison of the salt wash PSII 3D reconstruction with spinach PSII structure (PDB ID: 3JCU). (A) shows a side view and (B) shows a top view of the comparison. PSII is a homodimer in both structures. The extrinsic subunits are labeled in one monomer to show their location. The comparison shows the densities for PsbP and PsbQ are missing in the salt wash PSII 3D reconstruction.

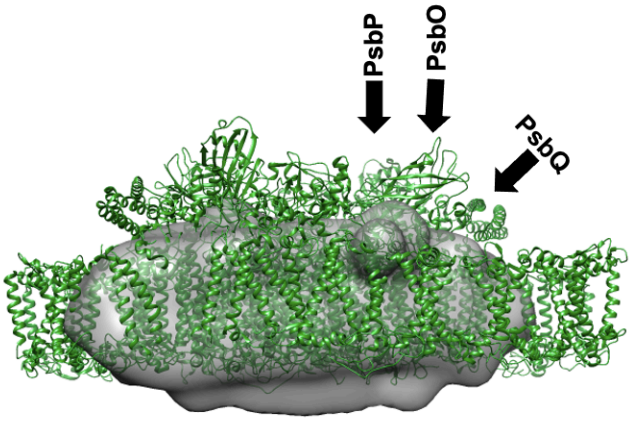

A

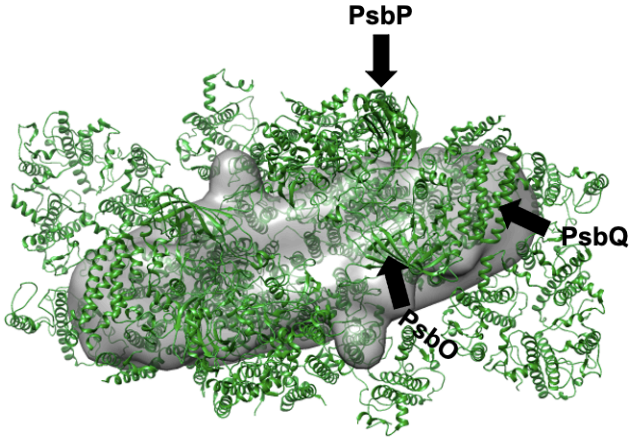

B

Figure 4.14. Superimposed comparison of urea wash PSII 3D reconstruction with spinach PSII structure (PDB ID: 3JCU). (A) shows a side view and (B) shows a top view of the comparison. PSII is a homodimer in both structures. The extrinsic subunits are labeled in one monomer to show their location. The comparison shows the densities for all extrinsic subunits are missing in the urea wash PSII 3D reconstruction.

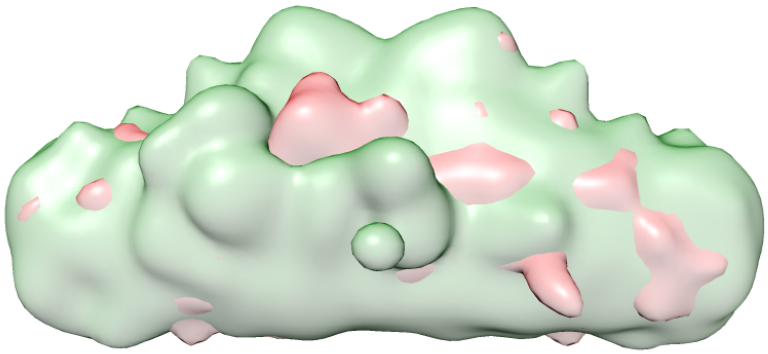

A

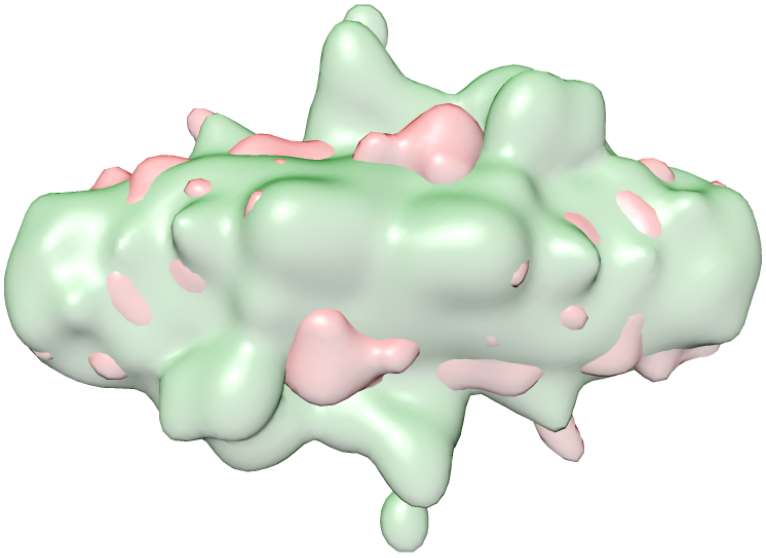

B

Figure 4.15. Superimposed comparison of active (Green) and salt wash (Red) PSII 3D reconstructions. (A) shows a side view and (B) shows a top view of the comparison. PSII is a homodimer in both structures. The comparison shows the densities for PsbP and PsbQ are present only in the active PSII 3D reconstruction.

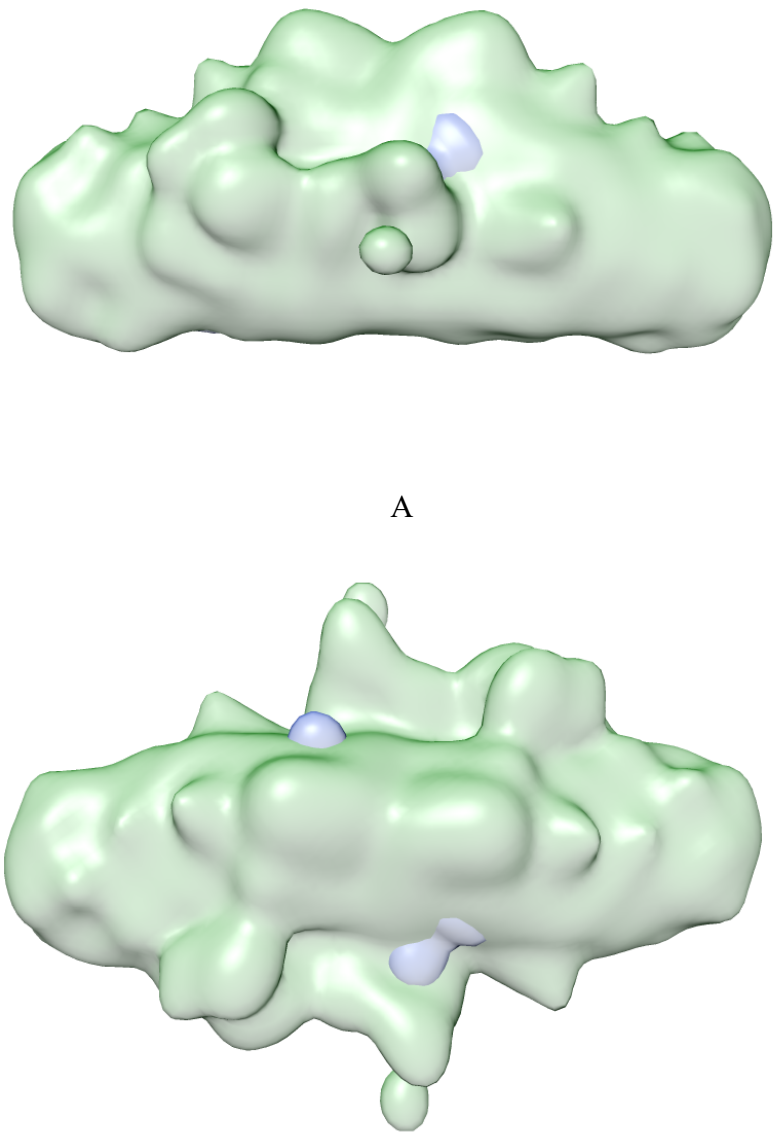

A

B

Figure 4.16. Superimposed comparison of active (Green) and urea wash (Blue) PSII 3D reconstructions. (A) shows a side view and (B) shows a top view of the comparison. PSII is a homodimer in both structures. The comparison shows there are densities for PsbO, PsbP, and PsbQ are missing from the urea wash PSII 3D reconstruction.

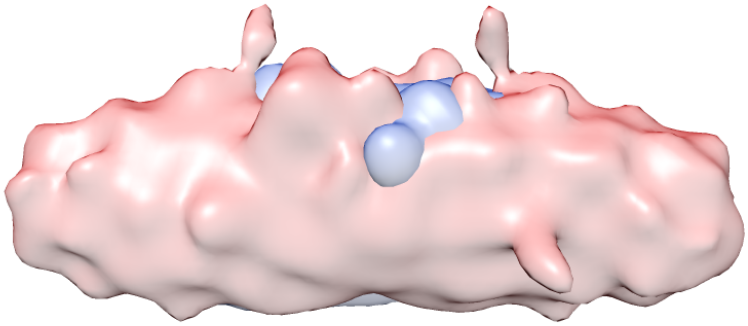

A

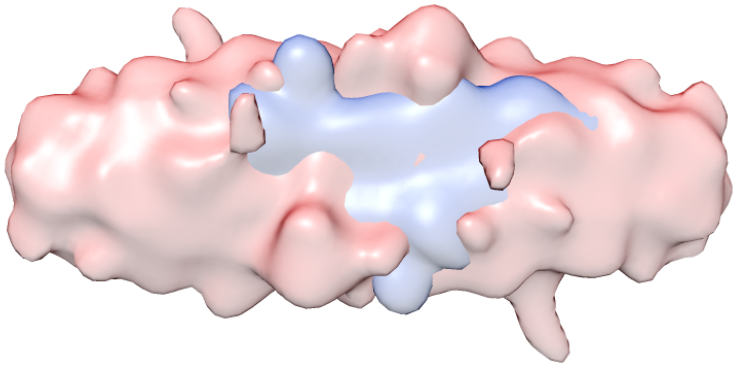

B

Figure 4.17. Superimposed comparison of salt wash (Red) and urea wash (Blue) PSII 3D reconstructions. (A) shows a side view and (B) shows a top view of the comparison. PSII is a homodimer in both structures. The comparison shows salt wash PSII 3D reconstruction contains density for PsbO which is not present in the urea wash PSII 3D reconstruction.

4.4 DISCUSSION

The same image processing approach was followed for the salt and urea wash PSII samples. However, the salt and urea wash PSII samples did not contain nearly as many particles as the control sample. Fewer images were collected and there were fewer particles per images for the salt wash and urea wash samples. It was still necessary to do preliminary image processing to compare the resulting 3D reconstructions. Thus, fewer class averages were excluded during image processing. A class average was discarded only when it had a substantially lower SNR based on visual inspection and particle size that did not match the target size. A careful balance had to be considered between discarding inferior particles and at the same time keeping as many particles as possible. With inferior particles present, the quality and resolution of the 3D reconstruction will be reduced. However, using only a few particles generally has a negative effect for 3D reconstruction as valuable signal can be lost. This was especially true for the salt wash and urea wash samples as they contained fewer particles.

The initial Refinement Package from the control PSII sample contained 53,742 particles. Due to the large number of particles in this sample, we were able to test a wide range of class average numbers (5-750). The class average numbers for the control PSII sample that resulted in the best 3D reconstruction were 10-25 class averages. The 3D reconstructions were less noisy and of higher resolution than other class averages. Class averaging of the salt wash and urea wash PSII samples required substantial care due to the smaller number of particles for these two PSII samples. The salt wash and urea wash sample data consisted of 1,475 particles and 9,192 particles, respectively. Due to the relatively low particle counts, class averages higher than 100 were not tested. For both salt and urea wash samples, 5-100 class averages were tested. For all 3

samples, 25 class averages were determined to be the optimal number of class averages based on the 3D reconstruction and resolution.

It was possible to observe the anticipated differences among the three samples already at the class averaging step. The class averages of the control sample had a crown shape indicating the presence of the extrinsic subunits. However, in the salt wash class averages, the crown shape density is a lot weaker and reduced in size. This is expected as the treatment with salt wash removes two of the extrinsic subunits (PsbP and PsbQ). The class averages from the urea wash sample do not have a crown shape or any density corresponding to any of the extrinsic subunits, indicating that all extrinsic subunits have been successfully removed.

Once the 3D reconstructions were obtained for all 3 samples, they were superimposed on a spinach structure (PDB ID: 3JCU) for a first comparison of our work with others. The 3JCU structure has a resolution of 3.2Å and it was obtained from spinach. However, it was obtained with different purification method and had reduced activity. This homodimer structure is a helpful comparison for our 3D reconstructions. The structures were superimposed manually by rotating our reconstructions on the x, y, z plane to align it with the 3JCU structure. In this process, several PSII features were very helpful. The transmembrane region as well as key subunits such as the LHCII complexes and the extrinsic subunits were critical in aligning the structures properly and ensuring correct alignment and superimposition.

While rotating our structures on the x, y, z plane, several fits were considered. There were some rotations that initially appeared to be a fit our structures into 3JCU. Yet the densities for various subunits did not align in a biologically and structurally meaningful manner. A good example of this is the LHCII complex. This complex is a trimer and present for each PSII monomer. Some rotations aligned our 3D reconstruction densities to show partial LHCII

complexes. Only one rotation clearly aligned our reconstructions in all dimensions and without any density for the two LHCII complexes for the PSII complex dimer. The LHCII complex could have been detached from the rest of the PSII complex at any step between sample purification to grid preparation. However, it is clear the LHCII is missing in all of our PSII 3D reconstructions.

Additional helpful features in our alignment were the extrinsic subunits. These subunits are located on top of the manganese cluster region where they can assist with oxygen evolution. Their densities give PSII a crown shape. This feature was critical in aligning our 3D reconstructions with the 3JCU structure as the crown-shaped density from these extrinsic subunits was easy to align with one obvious fit. This was especially true for the active PSII (all extrinsic subunits present) and the salt wash PSII (PsbO present) 3D reconstructions. However, this feature was not helpful in the urea wash 3D reconstruction because all extrinsic subunits were removed (no extrinsic densities present).

These considerations support only one correct fit for the alignment. The alignments allowed for the evaluation of the presence or absence of the different extrinsic subunits. For example, in the active PSII 3D reconstruction densities for PsbO, PsbP, and PsbQ are clearly present and in locations comparable to the corresponding subunits in the 3JCU structure. In the salt wash PSII 3D reconstruction, the crown-like shape has been greatly reduced as PsbP and PsbQ are removed by the salt wash treatment, with the two PsbO densities in locations to those corresponding to the 3JCU structure. The urea wash PSII 3D reconstruction does not show any density in these locations since all of the extrinsic subunits were successfully removed by the urea wash treatment.

It is worth noting that there are several densities missing in all three PSII 3D reconstructions. This includes the LHCII trimer complexes, the chlorophyll binding protein 26

kD (CP26), and the chlorophyll binding protein 29 kD (CP29). Additional, much smaller subunits may be missing from the overall structure. However, a high-resolution 3D reconstruction is needed for this kind of analysis.

The current 3D reconstructions show the overall architecture of PSII and missing subunits. These reconstructions are an important step towards obtaining high resolution reconstructions. However, interpretation of the data beyond the presence and overall location of the extrinsic subunits needs to be based on a larger number of particles and a reconstruction at higher resolution. One has to be very cautious about drawing additional conclusions as there are several limitations to consider. The 3D reconstructions for these samples are results of only a few thousand particles. Furthermore, there were preferred orientations in these particles (mostly side views). Generally, a significantly larger number (hundreds of thousands) particles are used for single particle analysis and these particles ideally provide many different views of the particle of interest. For example, in the salt wash sample, there is a weak density around the LHCII area. It may be noise, but it could also be due to protein density. An increased number of particles and improved resolution will allow for proper interpretation as noise would disappear with improved SNR and protein density would become defined.

The current reconstructions provide the overall architecture of PSII under these 3 different conditions and allow for first important conclusions on the presence and absence of major subunits. However, more detailed questions can only be answered with confidence when high resolution 3D reconstructions have been determined. Chapter 5 discusses detailed strategies that may be helpful in achieving this goal. Once high resolution is achieved, the molecular structures from these 3 PSII samples can be compared with one another to examine and understand what kind of conformational changes take place during the PSII repair mechanism.

4.5 ACKNOWLEDGMENTS

I would like to thank Dr. Bridgette Barry's Laboratory for the PSII project collaboration. Dr. Yusuf Uddin was an invaluable mentor and collaborator.

I would also like to thank Carolann Espy and Tajah Damm for their help with the salt wash and urea PSII image processing. They have helped me explore wide range parameters and ultimately identify the best image processing conditions for all 3 PSII samples. I want to thank my Ph.D. Advisor Dr. Schmidt-Krey for her valuable inputs and guidance on our data collection and image processing.

I want to thank Dr. Stroupe's Laboratory at Florida State University for their collaboration with data collection, especially Dr. Jay Rai generously sharing his expertise Dr. Nilakshee Bhattacharya is much appreciated for overseeing the automated cryo-EM data collection via NIH U24 consortium on the Titan Krios at Florida State University and many valuable discussions.

CHAPTER 5: CONCLUSIONS AND FUTURE DIRECTIONS

5.1 CONCLUSIONS

A wide range of crystallization parameters were tested for MCMJR1SPP. These parameters include testing of different purification fractions, LPRs, salt concentrations, glycerol concentrations, pH values, temperatures, and lengths of dialysis. By optimizing these 2D crystallization conditions, the size and quality of 2D MCMJR1SPP crystals was significantly improved. Crystallization with LPR 6-8, pH 6-6.5, temperature 24° - 27°C, 20% glycerol, 200-300mM NaCl gave the best results. Crystals grown in these conditions showed the highest quality (3-5) and several areas contained crystals larger than 150nm. The best results were consistently observed in MCMJR1SPP samples from purification fractions 11 and 12 from different purification batches. The use of specific fractions, rather than pooling fractions, after purification, dramatically improved reproducibility from purification to purification. The next important step to make the high-resolution structure determination possible, is to increase the crystal size to ideally 1 μm or even larger.

PSII was purified from market spinach using gentle purification to preserve its activity. Three different PSII samples (active PSII (control), salt wash PSII, and Urea wash PSII samples) were prepared for high-resolution cryo-EM data collection and image processing, including testing of particle picking strategies and single particle image processing parameters, resulted in 3D reconstructions for each sample. The 3D reconstruction for the salt wash sample clearly showed the absence of densities of the PsbP and PsbQ subunits while the urea wash sample 3D reconstruction showed the absence of densities for the three extrinsic subunits PsbO, PsbP, and PsbQ.

The compromise in sample heterogeneity in order to preserve PSII activity, required consideration of the different complex species of PSII. These species could easily be distinguished in the class averages as different class averages varied in the length of the long axis due to the absence of peripheral subunits such as LHCII and CP26. Thus, two different 3D reconstructions of the control sample were generated. The 3D reconstruction from the shorter class averages shows PSII with missing LHCII complexes and CP26 subunits, while the 3D reconstruction from the longer class averages shows PSII containing CP26 subunits. Improved quality in SNR and resolution of the 3D reconstruction was observed when particles and class averages of low quality were excluded.

5.2 MCMJR1SPP FUTURE DIRECTIONS

5.2.1 CRYSTALLIZATION TRIALS

The reconstituting phospholipid often plays a critical role in 2D crystallization. DMPC was used for SPP crystallization trials due to its key role in growing 2D crystals of a large percentage of membrane proteins[16]. However, it is worth investigating other phospholipids that have been successful for 2D crystallizations. One promising phospholipid is dioleoyl phosphatidylcholine (DOPC). DOPC has been used successfully to crystallize several membrane proteins[165]. The use of phospholipids with different charges or chain lengths is another option as well as a mixture of different lipids[166]. These approaches have been successful for 2D crystallization. Based on the presence of smaller ordered arrays within large membrane of sometimes 1μm or more in diameter, it may be feasible to induce large ordered arrays that span the entire membrane by removal of excess phospholipid. Two strategies may be pursued to

achieve this goal. Excess phospholipids can be removed during the purification, or during the crystallization process via the use of phospholipases[167].

Different buffers were thoroughly tested for MCMJR1SPP 2D crystallization. The use of different phospholipids may require additional optimization of the buffer, or even entirely different buffers.

In addition to 2D crystallization, a different cryo-EM approach of using nanodic reconstitution[30] combined with an MCMJR1SPP -specific antibody in order to increase the size of SPP via the antibody to make single particle cryo-EM feasible.

5.2.2 MCMJR1SPP 2D CRYO-EM AND FOLLOW UP EXPERIMENTS

Once large and well-ordered 2D crystals are available and after the MCMJR1SPP structure determination by 2D electron crystallography, a large number of additional structural studies are feasible. There are several MCMJR1SPP mutations that can be expressed and purified in Dr. Raquel Lieberman's laboratory. These mutations can shed light on the MCMJR1SPP reaction mechanism. The structure determination of these MCMJR1SPP mutants may be facilitated by the use of identical or similar 2D crystallization parameters as those for the wildtype protein. There are also known inhibitors such as $(Z\text{-}LL)_2$-ketone and transition state analogs for MCMJR1SPP[117]. These molecules can be used to arrest the protein in a specific state from which the structure may be determined in order to understand the MCMJR1SPP reaction mechanism.

5.3 PSII FUTURE DIRECTIONS

5.3.1 PSII CRYO-EM SAMPLE PREPARATION

Single particle cryo-EM grid preparation remains one of the critical bottlenecks for many samples. Ideally, cryo-EM grid preparation uses a minimal amount of sample, especially for very precious samples, and at the same time results in a good sample distribution and thin ice that can be used for high resolution data collection. In order to optimize cryo-EM grid preparation, several laboratories are working to reduce the required sample volume, to increase the distribution of sample on the grid, and to optimize the thickness of the ice[45, 168-170]. The sample concentration of PSII is not of concern as large quantities of PSII can be obtained by purification. A higher concentration of PSII on the cryo-EM grid, however, would allow for more efficient data collection and particle picking. For some samples, the distribution and particle number per micrograph could be improved via several rounds of sample application and blotting[170]. The presence of sucrose in the PSII sample prevented concentration under the conditions tested. In addition, preferred orientations of PSII particles need to be prevented or reduced. The Spotiton[45] has proven successful for a number of challenging samples and could be the solution for improving the cryo-EM grid preparation of the active PSII.

Graphene coated grids may be another alternative[168, 171, 172]. Graphene is one atom thick and can improve the contrast. This could have a big benefit for particle picking as well as image processing.

5.3.2 DATA COLLECTION

Our current 3D reconstructions for the PSII samples are estimated to be between 15-18Å resolution. In order to achieve high-resolution 3D reconstructions, additional data will be

collected. Ideally, these will be collected of samples at an increased concentration. Alternatively, a larger number of images will be collected.

5.3.3 AUTOMATIC PARTICLE PICKING

During the initial stage of PSII image processing, automatic particle picking was attempted using the RELION software. However, automated particle picking was not successful because the PSII sample was very heterogeneous. As a result, the 3D reconstruction was meaningless. Thus, manual particle picking was employed. However, automatic particle picking may improve with the most recent version of RELION or by using different software. In addition, testing of improved templates for particle picking may increase the particle number and final resolution. An improved template will make it possible to pick many particles in a very brief period of time, improve the quality of data by reducing human error at the particle picking stage, and thus also allow for faster testing of additional parameters.

This thesis has focused on determining the structure of 3 different PSII samples. The work done has provided 3D reconstructions that show the overall architectures. The long-term goal is to obtain high resolution structures for all 3 PSII samples. In order to achieve these, future works will focus on optimizing grid preparation in order to improve the concentration of the sample as well as the contrast. These improvements will improve the particle picking and the number of particles obtained. Furthermore, the current 3D reconstructions can be used to generate improved templates that can be used in automated particle picking which will save time and increase accuracy. These improvements would make it possible to obtain the high-resolution structures for all 3 samples. Once that is achieved, the high-resolution structures can be used to answer detailed questions about PSII repair mechanism.

REFERENCES

1. Lacapere, J.J., et al., *Determining membrane protein structures: still a challenge!* Trends Biochem Sci, 2007. **32**(6): p. 259-70.

2. Schmidt-Krey, I., et al., *Two-dimensional crystallization of human vitamin K-dependent gamma-glutamyl carboxylase.* J Struct Biol, 2007. **157**(2): p. 437-42.

3. Rubinstein J.L., W.J.E., Henderson R. , *Structure of the mitochondrial ATP synthase by electron cryomicroscopy.* EMBO J. , 2003. **22**: p. 6182-6192.

4. Dong, et al., *Structural basis of assembly of the human T cell receptor-CD3 complex.* Nature, 2019. **573**(7775): p. 546-552.

5. Gonen, T., Sliz, P., Kistler, J. et al., *Aquaporin-0 membrane junctions reveal the structure of a closed water pore.* Nature, 2004. **429**: p. 193–197.

6. Guerrero-Ferreira, R.C. and E.R. Wright, *Cryo-electron tomography of bacterial viruses.* Virology, 2013. **435**(1): p. 179-86.

7. Grunewald, K. and M. Cyrklaff, *Structure of complex viruses and virus-infected cells by electron cryo tomography.* Curr Opin Microbiol, 2006. **9**(4): p. 437-42.

8. Ke, Z., et al., *The Morphology and Assembly of Respiratory Syncytial Virus Revealed by Cryo-Electron Tomography.* Viruses, 2018. **10**(8).

9. Hampton, C.M., et al., *Correlated fluorescence microscopy and cryo-electron tomography of virus-infected or transfected mammalian cells.* Nat Protoc, 2017. **12**(1): p. 150-167.

10. Schubert, K., et al., *SARS-CoV-2 Nsp1 binds the ribosomal mRNA channel to inhibit translation.* Nat Struct Mol Biol, 2020. **27**(10): p. 959-966.

11. Cheng, Y., et al., *Cryo-electron tomography of clathrin-coated vesicles: structural implications for coat assembly.* J Mol Biol, 2007. **365**(3): p. 892-9.

12. Kühlbrandt, W., *Two-dimensional crystallization of membrane proteins.* Q Review Biophysics, 1992. **25**: p. 1-49.

13. Jap, B.K., Zulauf, M., Scheybani, T., Hefti, A., Baumeister, W., and U.a.E. Aebi, A., *2D crystallization- from art to science.* Ultramicroscopy, 1992. **46**: p. 45-84.

14. Engel, A., Hoenger, A., Hefti, A., Henn, C., Ford, R.C., Kistler, J., Zulauf, M., *Assembly of 2-D membrane protein crystals: dynamics, crystal order, and fidelity of structure analysis by electron microscopy.* J Struct Biol., 1992. **109**: p. 219-234.

15. Amos, L.A., Henderson, R., Unwin, P.N., *Three-dimensional structure determination by electron microscopy of two-dimensional crystals.* Prog Biophys Mol Biol., 1982. **39**: p. 183-231.

16. Ubarretxena-Belandia, I. and D.L. Stokes, *Membrane protein structure determination by electron crystallography.* Curr Opin Struct Biol, 2012. **22**(4): p. 520-8.

17. Jones, C.G., et al., *The CryoEM Method MicroED as a Powerful Tool for Small Molecule Structure Determination.* ACS Cent Sci, 2018. **4**(11): p. 1587-1592.

18. Nannenga, B.L. and T. Gonen, *Protein structure determination by MicroED.* Curr Opin Struct Biol, 2014. **27**: p. 24-31.

19. Iadanza, M.G. and T. Gonen, *A suite of software for processing MicroED data of extremely small protein crystals.* J Appl Crystallogr, 2014. **47**(Pt 3): p. 1140-1145.

20. Nannenga, B.L. and T. Gonen, *The cryo-EM method microcrystal electron diffraction (MicroED).* Nat Methods, 2019. **16**(5): p. 369-379.

21. Rubinstein, J.L., *Structural analysis of membrane protein complexes by single particle electron microscopy.* Methods, 2007. **41**(4): p. 409-16.

22. Cheng, Y., et al., *A primer to single-particle cryo-electron microscopy.* Cell, 2015. **161**(3): p. 438-449.

23. Cheng, Y., *Single-Particle Cryo-EM at Crystallographic Resolution.* Cell, 2015. **161**(3): p. 450-457.

24. Carroni, M. and H.R. Saibil, *Cryo electron microscopy to determine the structure of macromolecular complexes.* Methods, 2016. **95**: p. 78-85.

25. Thompson, R.F., et al., *An introduction to sample preparation and imaging by cryo-electron microscopy for structural biology.* Methods, 2016. **100**: p. 3-15.

26. Nagayama, K., *Development of phase plates for electron microscopes and their biological application.* Eur Biophys J, 2008. **37**(4): p. 345-58.

27. Danev, R. and K. Nagayama, *Phase Plates for Transmission Electron Microscopy*, in *Cryo-EM Part A Sample Preparation and Data Collection*. 2010. p. 343-369.

28. Wang, H.W. and X. Fan, *Challenges and opportunities in cryo-EM with phase plate.* Curr Opin Struct Biol, 2019. **58**: p. 175-182.

29. Frank, J., *Single-particle imaging of macromolecules by cryo-electron microscopy.* Annu Rev Biophys Biomol Struct, 2002. **31**: p. 303-19.

30. Strickland, K.M., Neselu, K., Grant, A.J., Espy, C.L., McCarty, N.A., Schmidt-Krey, I., *Reconstitution of detergent-solubilized membrane proteins into proteoliposomes and nanodiscs for functional and structural studies.* Methods in Molecular Biology, 2021. **Accepted**.

31. Schmidt-Krey, I., *Electron crystallography of membrane proteins: two-dimensional crystallization and screening by electron microscopy.* Methods, 2007. **41**(4): p. 417-26.

32. Johnson, M.C. and I. Schmidt-Krey, *Two-dimensional crystallization by dialysis for structural studies of membrane proteins by the cryo-EM method electron crystallography.* Methods Cell Biol, 2013. **113**: p. 325-37.

33. Uddin, Y.M. and I. Schmidt-Krey, *Inducing two-dimensional crystallization of membrane proteins by dialysis for electron crystallography.* Methods Enzymol, 2015. **557**: p. 351-62.

34. Unger, V.M., et al., *Expression, two-dimensional crystallization, and electron cryo-crystallography of recombinant gap junction membrane channels.* J Struct Biol, 1999. **128**(1): p. 98-105.

35. Booth, D.S., A. Avila-Sakar, and Y. Cheng, *Visualizing proteins and macromolecular complexes by negative stain EM: from grid preparation to image acquisition.* J Vis Exp, 2011(58).

36. De Carlo, S. and J.R. Harris, *Negative staining and cryo-negative staining of macromolecules and viruses for TEM.* Micron, 2011. **42**(2): p. 117-31.

37. Scarff, C.A., et al., *Variations on Negative Stain Electron Microscopy Methods: Tools for Tackling Challenging Systems.* J Vis Exp, 2018(132).

38. Dubochet J., M.A.W., *Vitrification of pure water for electron microscopy.* .lournu1 of Microscopy, 1981. **124**: p. RP3–RP4.

39. Dubochet, J., Adrian, M., Chang, J.-J., Homo, J.-C., Lepault, J., McDowall, A.W., Schultz, P., *Cryo-electron microscopy of vitrified specimens.* Q Review Biophysics, 1988. **21**: p. 129-228.

40. Lyumkis, D., *Challenges and opportunities in cryo-EM single-particle analysis.* J Biol Chem, 2019. **294**(13): p. 5181-5197.

41. Grassucci, R.A., D.J. Taylor, and J. Frank, *Preparation of macromolecular complexes for cryo-electron microscopy.* Nat Protoc, 2007. **2**(12): p. 3239-46.

42. Drulyte, I., et al., *Approaches to altering particle distributions in cryo-electron microscopy sample preparation.* Acta Crystallogr D Struct Biol, 2018. **74**(Pt 6): p. 560-571.

43. Bammes, B.E., et al., *Direct electron detection yields cryo-EM reconstructions at resolutions beyond 3/4 Nyquist frequency.* J Struct Biol, 2012. **177**(3): p. 589-601.

44. Suloway, C., et al., *Automated molecular microscopy: the new Leginon system.* J Struct Biol, 2005. **151**(1): p. 41-60.

45. Jain, T., et al., *Spotiton: a prototype for an integrated inkjet dispense and vitrification system for cryo-TEM.* J Struct Biol, 2012. **179**(1): p. 68-75.

46. Huo, J., et al., *Neutralization of SARS-CoV-2 by Destruction of the Prefusion Spike.* Cell Host Microbe, 2020. **28**(3): p. 445-454 e6.

47. Hiroaki, Y., et al., *Implications of the aquaporin-4 structure on array formation and cell adhesion.* J Mol Biol, 2006. **355**(4): p. 628-39.

48. Niu, Y., et al., *Cryo-EM analysis of PIP2 regulation in mammalian GIRK channels.* Elife, 2020. **9**.

49. Scheres, S.H., *RELION: implementation of a Bayesian approach to cryo-EM structure determination.* J Struct Biol, 2012. **180**(3): p. 519-30.

50. Grant, T., A. Rohou, and N. Grigorieff, *cisTEM, user-friendly software for single-particle image processing.* Elife, 2018. **7**.

51. Tang, G., et al., *EMAN2: an extensible image processing suite for electron microscopy.* J Struct Biol, 2007. **157**(1): p. 38-46.

52. Gipson, B., et al., *2dx--user-friendly image processing for 2D crystals.* J Struct Biol, 2007. **157**(1): p. 64-72.

53. Kremer, J.R., Mastronarde, D. N., McIntosh, J. R., *Computer Visualization of Three-Dimensional Image Data Using IMOD.* J. Struct. Biol., 1996. **116**: p. 71-76.

54. Hegerl, R., *The EM Program Package- A Platform for Image Processing in Biological Electron Microscopy.* J. Struct. Biol., 1996. **116**: p. 30-34.

55. Bayburt, T.H. and S.G. Sligar, *Membrane protein assembly into Nanodiscs.* FEBS Lett, 2010. **584**(9): p. 1721-7.

56. Denisov, I.G. and S.G. Sligar, *Nanodiscs for structural and functional studies of membrane proteins.* Nat Struct Mol Biol, 2016. **23**(6): p. 481-6.

57. Rouck, J.E., et al., *Recent advances in nanodisc technology for membrane protein studies (2012-2017).* FEBS Lett, 2017. **591**(14): p. 2057-2088.

58. Rigaud, J.-L.e.a., *Bio-Beads- An Efficient Strategy for Two-Dimensional Crystallization of Membrane Proteins.* J. Struct. Biol., 1997. **118**: p. 226–235.

59. Johnson, M.C., et al., *Assessing two-dimensional crystallization trials of small membrane proteins for structural biology studies by electron crystallography.* J Vis Exp, 2010(44).

60. Gyobu, N., et al., *Improved specimen preparation for cryo-electron microscopy using a symmetric carbon sandwich technique.* Journal of Structural Biology, 2004. **146**(3): p. 325-333.

61. Schmidt-Krey, I. and J.L. Rubinstein, *Electron cryomicroscopy of membrane proteins: specimen preparation for two-dimensional crystals and single particles.* Micron, 2011. **42**(2): p. 107-16.

62. Koning, R.I., Oostergetel, G.T., Brisson, A., *Preparation of flat carbon support films.* Ultramicroscopy, 2003. **94**: p. 183-191.

63. Braun, T. and A. Engel, *Two-dimensional Electron Crystallography*, in *Encyclopedia of Life Sciences*. 2005.

64. Kühlbrandt W., D.K.H., *Two-dimensional structure of plant light-harvesting complex at 3.7 A resolution by electron crystallography.* J Mol Biol, 1989. **207**: p. 823-828.

65. Schenk, A.D., et al., *3D Reconstruction from 2D Crystal Image and Diffraction Data*, in *Cryo-EM, Part B: 3-D Reconstruction*. 2010. p. 101-129.

66. Crowther, R.A., Henderson, R., Smith, J. M,, *MRC Image Processing Programs.* J Struct Biol. , 1996(116): p. 9-16.

67. Johnson, M.C., et al., *2D Electron Crystallography of Membrane Protein Single-, Double-, and Multi-Layered Ordered Arrays.* Methods Mol Biol, 2021. **2215**: p. 227-245.

68. Gonen T, C.Y., Sliz P, Hiroaki Y, Fujiyoshi Y, Harrison SC, Walz T., *Lipid-protein interactions in double-layered two-dimensional AQP0 crystals.* Nature, 2005(438): p. 633-638.

69. Miyazawa, A., Fujiyoshi, Y., Stowell, M., Unwin, N., *Nicotinic Acetylcholine Receptor at 4.6 AÊ Resolution- Transverse Tunnels in the Channel Wall.* Journal of Molecular Biology, 1999. **288**: p. 765-786.

70. Kühlbrandt, W., Wang, D. & Fujiyoshi, Y., *Atomic model of plant light-harvesting complex by electron crystallography.* Nature, 1994. **367**: p. 614-621.

71. Henderson, R., Unwin, P., *Three-dimensional model of purple membrane obtained by electron microscopy.* Nature, 1975. **257**: p. 28-32.

72. Iancu, C.V., et al., *Electron cryotomography sample preparation using the Vitrobot.* Nat Protoc, 2006. **1**(6): p. 2813-9.

73. Darrow, M.C., et al., *Chameleon: Next Generation Sample Preparation for CryoEM based on Spotiton.* Microscopy and Microanalysis, 2019. **25**(S2): p. 994-995.

74. Li, Y., et al., *High-Throughput Cryo-EM Enabled by User-Free Preprocessing Routines.* Structure, 2020. **28**(7): p. 858-869 e3.

75. van Heel, M., *Angular reconstitution: A posteriori assignment of projection directions for 3D reconstruction.* Ultramicroscopy, 1987. **21**: p. 111-123.

76. Nogales, E. and S.H. Scheres, *Cryo-EM: A Unique Tool for the Visualization of Macromolecular Complexity.* Mol Cell, 2015. **58**(4): p. 677-89.

77. Li, X., Mooney, P., Zheng, S. et al., *Electron counting and beam-induced motion correction enable near-atomic-resolution single-particle cryo-EM.* Nat Methods 2013. **10**.

78. Milazzo, A.C., et al., *Initial evaluation of a direct detection device detector for single particle cryo-electron microscopy.* J Struct Biol, 2011. **176**(3): p. 404-8.

79. Clough, R.N., Moldovan, G., Kirkland, A.I., *Direct Detectors for Electron Microscopy.* Journal of Physics: Conference Series, 2014. **522**.

80. McMullan, G., A.R. Faruqi, and R. Henderson, *Direct Electron Detectors.* Methods Enzymol, 2016. **579**: p. 1-17.

81. Faruqi, A.R. and G. McMullan, *Direct imaging detectors for electron microscopy.* Nuclear Instruments and Methods in Physics Research Section A: Accelerators, Spectrometers, Detectors and Associated Equipment, 2018. **878**: p. 180-190.

82. Cheng, A., et al., *Strategies for Automated CryoEM Data Collection Using Direct Detectors.* Methods Enzymol, 2016. **579**: p. 87-102.

83. McMullan, G., Chen, S., Henderson, R., Faruqi, A.R., *Detective quantum efficiency of electron area detectors in electron microscopy.* Ultramicroscopy, 2009. **109**: p. 1126-1143.

84. Meyer, R.R., Kirkland, A.I., Dunin-Borkowski, R.E., Hutchison, J.L., *Experimental characterisation of CCD camerasfor HREM at 300 kV.* Ultramicroscopy, 2000. **85**: p. 9-13.

85. Booth, C.R., J. Jakana, and W. Chiu, *Assessing the capabilities of a 4kx4k CCD camera for electron cryo-microscopy at 300kV.* J Struct Biol, 2006. **156**(3): p. 556-63.

86. Wu, S., J.P. Armache, and Y. Cheng, *Single-particle cryo-EM data acquisition by using direct electron detection camera.* Microscopy (Oxf), 2016. **65**(1): p. 35-41.

87. Carpenter, E.P., et al., *Overcoming the challenges of membrane protein crystallography.* Curr Opin Struct Biol, 2008. **18**(5): p. 581-6.

88. Wallin, E.v.H., G., *Genome-wide analysis of integral membrane proteins from eubacterial, archaean, and eukaryotic organisms.* Protien Science, 1998. **7**: p. 1029-1038.

89. Krogh, A., et al., *Predicting transmembrane protein topology with a hidden Markov model: application to complete genomes.* J Mol Biol, 2001. **305**(3): p. 567-80.

90. Merk, A., et al., *Breaking Cryo-EM Resolution Barriers to Facilitate Drug Discovery.* Cell, 2016. **165**(7): p. 1698-1707.

91. Tan, S., H.T. Tan, and M.C. Chung, *Membrane proteins and membrane proteomics.* Proteomics, 2008. **8**(19): p. 3924-32.

92. Lin, S.-H. and G. Guidotti, *Chapter 35 Purification of Membrane Proteins*, in *Guide to Protein Purification, 2nd Edition*. 2009. p. 619-629.

93. Caffrey, M., *Membrane protein crystallization.* Journal of Structural Biology, 2003. **142**(1): p. 108-132.

94. Seddon, A.M., P. Curnow, and P.J. Booth, *Membrane proteins, lipids and detergents: not just a soap opera.* Biochim Biophys Acta, 2004. **1666**(1-2): p. 105-17.

95. Stetsenko, A., Guskov, A., *An Overview of the Top Ten Detergents Used for Membrane Protein Crystallization.* Crystals, 2017. **7**(7): p. 1-16.

96. Martoglio, B. and T.E. Golde, *Intramembrane-cleaving aspartic proteases and disease: presenilins, signal peptide peptidase and their homologs.* Hum Mol Genet, 2003. **12 Spec No 2**: p. R201-6.

97. Lemberg, M.K., et al., *Intramembrane proteolysis of signal peptides: an essential step in the generation of HLA-E epitopes.* J Immunol, 2001. **167**(11): p. 6441-6.

98. Urban, S., Freeman, M., *Intramembrane proteolysis controls diverse signalling pathwaysthroughout evolution.* Current Opinion in Genetics & Development, 2002. **12**: p. 512-518.

99. Naing, S.H., et al., *Catalytic Properties of Intramembrane Aspartyl Protease Substrate Hydrolysis Evaluated Using a FRET Peptide Cleavage Assay.* ACS Chem Biol, 2015. **10**(9): p. 2166-74.

100. Manolaridis, I., et al., *Mechanism of farnesylated CAAX protein processing by the intramembrane protease Rce1.* Nature, 2013. **504**(7479): p. 301-5.

101. Kuhnle, N., V. Dederer, and M.K. Lemberg, *Intramembrane proteolysis at a glance: from signalling to protein degradation.* J Cell Sci, 2019. **132**(16).

102. Erez, E., D. Fass, and E. Bibi, *How intramembrane proteases bury hydrolytic reactions in the membrane.* Nature, 2009. **459**(7245): p. 371-8.

103. Fluhrer, R., H. Steiner, and C. Haass, *Intramembrane proteolysis by signal peptide peptidases: a comparative discussion of GXGD-type aspartyl proteases.* J Biol Chem, 2009. **284**(21): p. 13975-9.

104. Naing, S.H., et al., *Both positional and chemical variables control in vitro proteolytic cleavage of a presenilin ortholog.* J Biol Chem, 2018. **293**(13): p. 4653-4663.

105. Torres-Arancivia, C., et al., *Identification of an archaeal presenilin-like intramembrane protease.* PLoS One, 2010. **5**(9).

106. Ponting, C.P., Hutton, M., Nyborg, A., Baker, M., Jansen, K., and Golde, T. E., *Identification of a novel family of presenilin homologues.* Human molecular genetics, 2002. **11**: p. 1037-1044.

107. De Strooper, B., *Aph-1, Pen-2, and Nicastrin with Presenilin Generate an Active γ-Secretase Complex.* Neuron, 2003. **38**: p. 9-12.

108. Franberg, J., et al., *gamma-Secretase dependent production of intracellular domains is reduced in adult compared to embryonic rat brain membranes.* PLoS One, 2010. **5**(3): p. e9772.

109. Wolfe, M., Xia, W., Ostaszewski, B. et al., *Two transmembrane aspartates in presenilin-1 required for presenilin endoproteolysis and γ-secretase activity.* Nature, 1999. **398**: p. 513–517.

110. Bolduc, D.M., et al., *The amyloid-beta forming tripeptide cleavage mechanism of gamma-secretase.* Elife, 2016. **5**.

111. Lichtenthaler, S.F., C. Haass, and H. Steiner, *Regulated intramembrane proteolysis--lessons from amyloid precursor protein processing.* J Neurochem, 2011. **117**(5): p. 779-96.

112. De Strooper, B., T. Iwatsubo, and M.S. Wolfe, *Presenilins and gamma-secretase: structure, function, and role in Alzheimer Disease.* Cold Spring Harb Perspect Med, 2012. **2**(1): p. a006304.

113. Auclair, S.M., M.K. Bhanu, and D.A. Kendall, *Signal peptidase I: cleaving the way to mature proteins.* Protein Sci, 2012. **21**(1): p. 13-25.

114. McLauchlan, J., Lemberg, M. K., Hope, G., and Martoglio, B., *Intramembrane proteolysis promotes traf®cking of hepatitis C virus core protein to lipid droplets.* The EMBO journal, 2002. **21**: p. 3980-3988.

115. Nyborg, A.C., et al., *Intramembrane proteolytic cleavage by human signal peptide peptidase like 3 and malaria signal peptide peptidase.* FASEB J, 2006. **20**(10): p. 1671-9.

116. Sato, T., Nyborg, A. C., Iwata, N., Diehl, T. S., Saido, T. C., Golde, T. E., and Wolfe, M. S., *Signal Peptide Peptidase- Biochemical Properties and Modulation by Nonsteroidal Antiinflammatory Drugs.* Biochemistry, 2006. **45**: p. 8649-8656.

117. Weihofen, A., et al., *Targeting presenilin-type aspartic protease signal peptide peptidase with gamma-secretase inhibitors.* J Biol Chem, 2003. **278**(19): p. 16528-33.

118. Gertsik, N., D.M. Chau, and Y.M. Li, *gamma-Secretase Inhibitors and Modulators Induce Distinct Conformational Changes in the Active Sites of gamma-Secretase and Signal Peptide Peptidase.* ACS Chem Biol, 2015. **10**(8): p. 1925-31.

119. Dang, S., et al., *Cleavage of amyloid precursor protein by an archaeal presenilin homologue PSH.* Proc Natl Acad Sci U S A, 2015. **112**(11): p. 3344-9.

120. Weihofen, A., Binns, K., Lemberg, M. K., Ashman, K., and Martoglio, B., *Identification of Signal Peptide Peptidase, a Presenilin-Type Aspartic Protease.* Science, 2002. **296**: p. 2215-2218.

121. Li, X., et al., *Structure of a presenilin family intramembrane aspartate protease.* Nature, 2013. **493**(7430): p. 56-61.

122. Bai, X.C., et al., *An atomic structure of human gamma-secretase.* Nature, 2015. **525**(7568): p. 212-217.

123. Bai, X.C., et al., *Sampling the conformational space of the catalytic subunit of human gamma-secretase.* Elife, 2015. **4**.

124. Miyashita, H., et al., *Three-dimensional structure of the signal peptide peptidase.* J Biol Chem, 2011. **286**(29): p. 26188-97.

125. Kalyoncu, S., *STRUCTURAL AND FUNCTIONAL CHARACTERIZATION OF AN INTRAMEMBRANE PEPTIDASE AND A NON-PEPTIDASE.* Ph.D Thesis. Georgia georgia Institute of Technology, 2016: p. 1-177.

126. Naing, S.H., *SOLUTION STRUCTURE AND BIOCHEMISTRY OF AN INTRAMEMBRANE ASPARTYL PROTEASE (IAP).* Ph.D Thesis. Georgia georgia Institute of Technology, 2018: p. 1-129.

127. Metcalfe, M.G., *Two-dimensional crystallization of archaeal signal peptide peptidases for structural studies by electron crystrallography.* Master's Thesis. Georgia georgia Institute of Technology, 2014: p. 1-54.

128. Schmidt-Krey, I., et al., *Parameters for the two-dimensional crystallization of the membrane protein microsomal glutathione transferase.* J Struct Biol, 1998. **123**(2): p. 87-96.

129. Zhao, G., et al., *Two-dimensional crystallization conditions of human leukotriene C4 synthase requiring adjustment of a particularly large combination of specific parameters.* J Struct Biol, 2010. **169**(3): p. 450-4.

130. Barber, J., *Photosynthetic energy conversion: natural and artificial.* Chem Soc Rev, 2009. **38**(1): p. 185-96.

131. Mizusawa, N. and H. Wada, *The role of lipids in photosystem II.* Biochim Biophys Acta, 2012. **1817**(1): p. 194-208.

132. Shen, J.-R., *Photosystem II: Protein Components, Structure and Electron Transfer*, in *Reference Module in Life Sciences*. 2020.

133. Umena Y, K.K., Shen JR, Kamiya N. , *Crystal structure of oxygen-evolving photosystem II at a resolution of 1.9 Å.* Nature, 2011. **473**: p. 55-60.

134. Ago, H., et al., *Novel Features of Eukaryotic Photosystem II Revealed by Its Crystal Structure Analysis from a Red Alga.* J Biol Chem, 2016. **291**(11): p. 5676-87.

135. Wei, X., et al., *Structure of spinach photosystem II-LHCII supercomplex at 3.2 A resolution.* Nature, 2016. **534**(7605): p. 69-74.

136. Tanaka, A., Y. Fukushima, and N. Kamiya, *Two Different Structures of the Oxygen-Evolving Complex in the Same Polypeptide Frameworks of Photosystem II.* J Am Chem Soc, 2017. **139**(5): p. 1718-1721.

137. Su X.D., M.J., Wei X.P., Cao P., Zhu D.J., Chang W.R. Liu, Z., Zhang, X, Li, M., *Structure and assembly mechanism of plant C2S2M2-type PSII-LHCII supercomplex.* Science, 2017. **357**: p. 816–820.

138. Shen, L., et al., *Structure of a C2S2M2N2-type PSII-LHCII supercomplex from the green alga Chlamydomonas reinhardtii.* Proc Natl Acad Sci U S A, 2019. **116**(42): p. 21246-21255.

139. Huang, G., et al., *Structural insights into a dimeric Psb27-photosystem II complex from a cyanobacterium Thermosynechococcus vulcanus.* Proc Natl Acad Sci U S A, 2021. **118**(5).

140. Nield, J., Orlova, E., Morris, E. et al., *3D map of the plant photosystem II supercomplex obtained by cryoelectron microscopy and single particle analysis.* Nat Struct Mol Biol, 2000. **7**: p. 44–47.

141. Albanese, P., et al., *Pea PSII-LHCII supercomplexes form pairs by making connections across the stromal gap.* Sci Rep, 2017. **7**(1): p. 10067.

142. van Bezouwen, L.S., et al., *Subunit and chlorophyll organization of the plant photosystem II supercomplex.* Nat Plants, 2017. **3**: p. 17080.

143. Kawakami, K. and J.R. Shen, *Purification of fully active and crystallizable photosystem II from thermophilic cyanobacteria.* Methods Enzymol, 2018. **613**: p. 1-16.

144. Shen, J.R., Ikeuchi, M., Inoue Y., *Stoichiometric association of extrinsic cytochrome c550 and 12 kDa protein with a highly purified oxygen-evolving photosystem II core complex from Synechococcus vulcanus.* FEBS Lett 1992. **301**: p. 145-149.

145. Berthold, D.A., Babcock, F.T, Yocum, C.F., *A highly resolved, oxygenevolving photosystem II preparation from spinach thylakoid membranes: EPR and electron-transport properties.* FEBS Letters, 1981. **134**: p. 231-234.

146. Mishra, R.K., Ghanotakis, D.F., *Selective extraction of CP 26 and CP 29 proteins without affecting the bindi of the extrinsic proteins (33, 23 and 17 kDa) and the DCMU sensiti ty of a Photosystem H core complex.* Photosynth Res, 1994. **42**: p. 37–42.

147. Uddin, Y.M., *Biochemical Characterization and Cryo-EM Studies of a Highly Active Spinach Photosystem II Complex.* Ph.D Thesis. Georgia georgia Institute of Technology, 2018: p. 1-143.

148. Lander, G.C., et al., *Appion: an integrated, database-driven pipeline to facilitate EM image processing.* J Struct Biol, 2009. **166**(1): p. 95-102.

149. Pettersen, E.F., et al., *UCSF Chimera--a visualization system for exploratory research and analysis.* J Comput Chem, 2004. **25**(13): p. 1605-12.

150. Tegunov, D., et al., *Multi-particle cryo-EM refinement with M visualizes ribosome-antibiotic complex at 3.5 A in cells.* Nat Methods, 2021. **18**(2): p. 186-193.

151. Liu, C., et al., *A Non-covalent Ligand Reveals Biased Agonism of the TRPA1 Ion Channel.* Neuron, 2021. **109**(2): p. 273-284 e4.

152. Bartesaghi, A., et al., *Atomic Resolution Cryo-EM Structure of beta-Galactosidase.* Structure, 2018. **26**(6): p. 848-856 e3.

153. Baradaran, R., et al., *Cryo-EM structures of fungal and metazoan mitochondrial calcium uniporters.* Nature, 2018. **559**(7715): p. 580-584.

154. Rohou, A. and N. Grigorieff, *CTFFIND4: Fast and accurate defocus estimation from electron micrographs.* J Struct Biol, 2015. **192**(2): p. 216-21.

155. Lyumkis, D., et al., *Likelihood-based classification of cryo-EM images using FREALIGN.* J Struct Biol, 2013. **183**(3): p. 377-388.

156. Scheres S.H., V.M., Nunez R., Sorzano C.O., Marabini R., Herman G.T., Carazo J.M., *Maximum-likelihood multi-reference refinement for electron microscopy images.* Journal of Molecular Biology, 2005. **31**: p. 139-149.

157. Grigorieff, N., *Frealign: An Exploratory Tool for Single-Particle Cryo-EM.* Methods Enzymol, 2016. **579**: p. 191-226.

158. Saibil, H.R., *Conformational changes studied by cryo-electron microscopy.* Nat Struct Mol Biol, 2000. **7**: p. 711–714.

159. Murata, N., et al., *Photoinhibition of photosystem II under environmental stress.* Biochim Biophys Acta, 2007. **1767**(6): p. 414-21.

160. Offenbacher, A.R., B.C. Polander, and B.A. Barry, *An intrinsically disordered photosystem II subunit, PsbO, provides a structural template and a sensor of the hydrogen-bonding network in photosynthetic water oxidation.* J Biol Chem, 2013. **288**(40): p. 29056-68.

161. Mulo, P., Laakso, S., Mäenpää, P., Aro, E.M., *Stepwise Photoinhibition of Photosystem II.* Plant Physiol., 1998. **117**: p. 483-490.

162. Boekema, E.J., Nield, J., Hankamer, B. and Barber, J., *Localization of the 23-kDa subunit of the oxygen-evolving complex of photosystem II by electron microscopy.* European Journal of Biochemistry, 1998. **252**: p. 268-276.

163. Boekema, E.J., van Breemen, J. F.L., van Roon, H., and Dekker, J. P., *Conformational Changes in Photosystem II Supercomplexes upon Removal of Extrinsic Subunits.* Biochemistry, 2000. **39**: p. 12907-12915.

164. Nield, J., et al., *Three-dimensional electron cryo-microscopy study of the extrinsic domains of the oxygen-evolving complex of spinach: assignment of the PsbO protein.* J Biol Chem, 2002. **277**(17): p. 15006-12.

165. De Zorzi, R., et al., *Growth of large and highly ordered 2D crystals of a K(+) channel, structural role of lipidic environment.* Biophys J, 2013. **105**(2): p. 398-408.

166. Rémigy, H.W., et al., *Membrane protein reconstitution and crystallization by controlled dilution.* FEBS Letters, 2003. **555**(1): p. 160-169.

167. Mohraz, M., Yee, M., Smith, P.R., *Novel crystalline sheets of Na,K-ATPase induced by phospholipase A2.* Journal of Ultrastructure Research, 1985. **93**: p. 17-26.

168. Han, Y., et al., *High-yield monolayer graphene grids for near-atomic resolution cryoelectron microscopy.* Proc Natl Acad Sci U S A, 2020. **117**(2): p. 1009-1014.

169. Razinkov, I., et al., *A new method for vitrifying samples for cryoEM.* J Struct Biol, 2016. **195**(2): p. 190-198.

170. Snijder, J., et al., *Vitrification after multiple rounds of sample application and blotting improves particle density on cryo-electron microscopy grids.* J Struct Biol, 2017. **198**(1): p. 38-42.

171. Pantelic, R.S., et al., *Graphene oxide: a substrate for optimizing preparations of frozen-hydrated samples.* J Struct Biol, 2010. **170**(1): p. 152-6.

172. Russo, C., Passmore, L., *Controlling protein adsorption on graphene for cryo-EM using lowenergy hydrogen plasmas.* Nat Methods, 2014. **11**: p. 649–652.